The Geochemistry of the Gough Island Basalts and their Mantle Source Region

David J. Long
B.Sc. (Hons)

Thesis submitted in fulfilment of the requirements for the degree of Master of Science

Department of Geological Sciences
University of Cape Town

October 2008

Supervisors:
Professor Anton le Roex[1]
Dr Cornelia Class[2]

[1] Department of Geological Sciences, University of Cape Town, Private Bag, Rondebosch, 7701, South Africa.
[2] Department of Geochemistry, Lamont-Doherty Earth Observatory of Columbia University, 61 Route 9W, Palisades, New York, 10964, U.S.A.

Abstract

Basalts from Gough Island and the McNish Seamount were selected for a detailed geochemical study, using major and trace element data as well as $^{143}Nd/^{144}Nd$, $^{87}Sr/^{86}Sr$ and newly acquired $^{176}Hf/^{177}Hf$ isotope data. The geochemical data are subsequently used to determine the petrogenesis of the Gough Island suite of lavas and the evolution of the underlying mantle source region.

Gough Island (40°19'S; 09°56'W) and the McNish Seamount (40°10'S; 08°31'E) are both located in the south Atlantic Ocean on ~34Ma crust of the African plate. The Gough Island suite of lavas consist of picrite basalts, olivine basalts, trachybasalts, trachytes and aegirine-augite trachytes; three different varieties of olivine basalt exist - the coarsely pyroxene-olivine phyric basalts, moderately pyroxene-olivine phyric basalts and aphyric to finely porphyritic basalts (le Maitre, 1962, le Roex, 1985). The oldest lavas from Gough Island are dated at 2.5Ma (Lower Basalts), whereas the youngest lavas are dated at 0.1Ma (Upper Basalts) (Maund *et al.*, 1988).

Thirty-eight olivine basalts and trachybasalts (10 Lower Basalts, 27 Middle Basalts and 1 Upper Basalt) were chosen to form the sample set used in this study and range from aphyric through finely to coarsely porphyritic. Two distinct petrographic groups exist in the Lower and Middle Basalts, where the first group consists of anhedral to euhedral olivine phenocrysts and anhedral to subhedral clinopyroxene as the major and minor phenocryst phases, respectively. The second group consists of anhedral to subhedral clinopyroxene and subhedral olivine as the major and minor phenocryst phases, respectively. All of the samples exhibit an intergranular texture with a groundmass assemblage consisting of olivine, plagioclase, titanomagnetite, ilmenite and apatite.

The lavas consist of basalts, trachybasalts and basaltic trachyandesites and therefore form a alkali basalt – trachyte series on a TAS diagram. Both the Lower and Middle Basalts range from basaltic to basaltic trachyandesite whereas the single Upper Basalt sample is a basaltic trachyandesite. SiO_2 ranges from 45.15 to 52.61wt%, K_2O from 1.19-4.39wt%, Al_2O_3 from 8.76-18.50wt%, CaO from 5.74-12.00wt%, MgO from 3.05-17.30wt% and Mg# from 37.9-75.3. The Lower, Middle and Upper Basalts of the Gough Island lavas as well as the McNish Seamount lavas are all superimposed on major element variation diagrams.

High precision trace element data for the Gough Island and the McNish Seamount suite of lavas exhibit high incompatible (e.g. Ba, Ta, Nb, Rb) and moderately incompatible (e.g. Hf, Y, Ce, Sr) trace element concentrations with high Ba/Nb (11.6-18.0), low Zr/Nb (4.51-7.39) and variable La/Nb (0.84-1.18) ratios. The Lower, Middle and Upper Basalts exhibit similar trace element concentrations. Variation diagrams of Ba, Ta, Rb vs. Zr indicates the continuous fractionation of mineral phases with increasing magma differentiation. The primitive mantle normalised trace element

diagrams are sub-parallel and exhibit positive Ba and Pb as well as negative Th, U and Zr anomalies. The chondrite normalised REE diagrams for most samples are sub-parallel, and are LREE enriched relative to HREE. Some exhibit crossing patterns between Tb and Dy.

$^{176}Hf/^{177}Hf$ isotope ratios were measured for 27 basalts from Gough Island and 3 samples from the McNish Seamount and range from 0.282699±12 to 0.282778±10 and 0.282715±16 to 0.282757±12, respectively. The Gough Island lavas form a tight, steep array in Hf-Nd isotope space, whereas the McNish Seamount forms a tight near-vertical array in Hf-Nd isotope space that intersects the Gough Island array. These two suites of lava plot towards the enriched (relative to PM) end of the global OIB array, within the more depleted (relative to PM) end of the continental array (Vervoort *et al.*, 1999), and exhibit similar $^{176}Hf/^{177}Hf$, $^{143}Nd/^{144}Nd$ and $^{87}Sr/^{86}Sr$ isotope ratios as Tristan da Cunha and Inaccessible Island.

Ten Gough Island primary magma compositions were calculated for use in constrained forward modelling. The primary magma compositions were calculated by the addition of 14-28% clinopyroxene and equilibrium olivine, in equal proportions, back into the primitive lava compositions in 1% increments until an Mg# of 69 was reached. Constrained forward modelling methods were used in determining the chemical and mineralogical nature of the mantle source region as well as the required melting parameters required in producing the Gough Island suite of lavas. The models indicate that the full compositional range, as well as the crossing REE patterns at Dy, can be produced through ~5-8% equilibrium melting of a mantle source region composed of garnet lherzolite or ~30-50% melting of a garnet pyroxenite source.

Numerous studies of OIB from around the world show that the enriched trace element and isotope compositions require involvement of a lithospheric component (Andres *et al.*, 2002, Chauvel *et al.*, 1992, Class & le Roex, 2008, Gibson *et al.*, 2005, Lustrino, 2005, White & Hofmann, 1982, Willbold & Stracke, 2006). To test this hypothesis, binary mixing curves were calculated between a typical OIB mantle source region composition and datasets of lower crustal xenoliths, mantle xenoliths representing Southern African SCLM as well as modern marine sediments in $^{176}Hf/^{177}Hf$-$^{143}Nd/^{144}Nd$-$^{87}Sr/^{86}Sr$-Ba/Nb-Zr/Nb-$(Ce/Ce^*)_{Nd}$ space and superimposed on the Gough Island array. It is shown, based on Ce-anomalies, that the Gough Island lavas do not exhibit a lower crust or SCLM signature as these components do not exhibit a large negative Ce-anomaly. It is argued that the Gough Island lavas are derived from a source more typical of South Atlantic OIB, but with a significant recycled marine sediment component.

Declaration

I hereby declare that all the work presented in this dissertation is my own, except where otherwise stated.

Signed by candidate

David James Long

Acknowledgements

Firstly I would like to thank my two supervisors, Professor Anton le Roex and Dr Cornelia Class for the guidance, patience and opportunity you have shown and given me over these past few years.

Also many thanks to Dr Steve Goldstein, Tina van de Flierdt and Cai (Merry) Yue for assistance and guidance during my visits to L-DEO. I would also like to thank Taber Hersum, Jill van Tongeren, Anna Cipriani, Malka Machlus, Antonio Buono and Debra Tillinger for making me feel at home during my visits and to David Wilson (UCT) for preparing thin sections at a moments notice for me during the course of this study.

Lastly, I would like to especially thank Chazanne Allison, my brother Michael Long and my parents for their constant support and assistance throughout these past years.

Table of Contents

ABSTRACT II

DECLARATION IV

ACKNOWLEDGEMENTS V

TABLE OF CONTENTS VI

1 INTRODUCTION 1-1

1.1 Ocean Island Basalts and Gough Island 1-1
1.2 The Hafnium Isotope System 1-1
1.3 Petrogenesis of the Gough Island Suite of Lavas 1-2
1.4 Evolution of the Gough Island Mantle Source Region 1-3
1.5 Objectives 1-3

2 GEOLOGICAL SETTING 2-1

2.1 Gough Island 2-1
2.2 Previous Work 2-3

3 ANALYTICAL TECHNIQUES 3-1

4 PETROGRAPHY 4-1

4.1 Lower Basalts 4-1
4.2 Middle Basalts 4-2
4.3 Upper Basalts 4-3

5 BULK ROCK GEOCHEMISTRY 5-1

5.1 Introduction 5-1
5.2 Major Element Geochemistry 5-1
5.3 Trace Element Geochemistry 5-4
5.4 The McNish Seamount 5-9

6 ISOTOPE GEOCHEMISTRY 6-1

6.1 Introduction 6-1
6.2 The Lu-Hf Isotope System and its Relationship to the Sm-Nd Isotope System 6-1
6.3 Isotope Geochemistry of the Gough Island and McNish Seamount Lavas 6-3
6.4 Gough Island in a Regional and Global Context 6-5
6.5 Hf Isotope and Trace Element Variation 6-9

7 PETROGENESIS OF THE GOUGH ISLAND SUITE OF LAVAS 7-1

7.1 Introduction 7-1
7.2 Partial Melting Models 7-1
7.3 Determination of Primary Magma Compositions 7-2
7.4 Constrained Forward Modelling 7-6
7.5 A Peridotite Mantle Source Region 7-7
7.5.1 Spinel Lherzolite *7-9*
7.5.2 Garnet Lherzolite *7-12*
7.6 Pyroxenite Mantle Source Region 7-15
7.6.1 Garnet Pyroxenite *7-17*
7.7 Summary of Mantle Source Region Modelling 7-19

8 EVOLUTION OF THE GOUGH ISLAND MANTLE SOURCE REGION 8-1

8.1 Introduction 8-1
8.1.1 The Gough Island Suite of Lavas *8-1*
8.1.2 Ce-Anomalies *8-1*

8.1.3 Previous Work *8-2*
8.2 END-MEMBER COMPONENTS USED IN BINARY MIXING CALCULATIONS 8-3
8.2.1 Starting Composition *8-4*
8.3 GEOCHEMISTRY OF END-MEMBER COMPONENTS 8-6
8.3.1 $(Ce/Ce^*)_{Nd}$ Ratios *8-6*
8.3.2 Ba/Nb Ratios *8-7*
8.3.3 $^{176}Hf/^{177}Hf$, $^{143}Nd/^{144}Nd$ and $^{87}Sr/^{86}Sr$ Isotope Ratios *8-8*
8.4 BINARY MIXING CALCULATIONS 8-9
8.4.1 The Role of Lower Crust *8-9*
8.4.2 The Role of SCLM *8-10*
8.4.3 The Role of Sediment *8-11*
8.5 SUMMARY 8-14

9 SUMMARY AND CONCLUSIONS **9-1**

9.1 OVERVIEW 9-1
9.2 PETROGRAPHY 9-1
9.3 BULK ROCK GEOCHEMISTRY 9-1
9.4 ISOTOPE GEOCHEMISTRY 9-3
9.5 PETROGENESIS OF THE GOUGH ISLAND SUITE OF LAVAS 9-3
9.6 EVOLUTION OF THE GOUGH ISLAND MANTLE SOURCE REGION 9-4

10 REFERENCES **10-1**

Appendix A Sample Petrography A-1
A.1 Gough Island A-1
A.2 McNish Seamount A-7
Appendix B Sample Preparation B-1

1 Introduction

1.1 Ocean Island Basalts and Gough Island

One of the fundamental problems in studying the mantle and mantle dynamics is the limited availability of fresh, unaltered mantle rocks and therefore geochemists must rely on a range of different rocks which can act as a window into the mantle (Hofmann, 1997). One type of rock that serves this objective particularly well is ocean-island basalts (OIB). Volcanic islands and seamounts that form on intra-plate oceanic crust by means of hotspots or local melting anomalies and are not related to subduction zone processes, are composed (although not exclusively) of basalt known as OIB (Hofmann, 1997). OIB have been and are extensively studied as these lavas pass through the oceanic crust (Green & Ringwood, 1967, Hofmann, 1997, Yoder, 1976) and not the continental crust, which implies that they have experienced less interaction with crustal material. However, OIB are still subjected to processes which can alter their original primary magma composition and therefore corrections need to be made for any chemical overprints which can occur as magma migrates from the mantle source region to the surface of the Earth.

OIB exhibit a large variation in isotope ratios, whereas mid-oceanic ridge basalts (MORB) exhibit a more depleted (relative to a primitive mantle (PM)) isotope composition, and OIB fan away from typical MORB compositions to more enriched (relative to PM) isotope compositions (Hofmann, 1997, Zindler & Hart, 1986). This trend suggests that the various OIB plot on a mixing line between less radiogenic (depleted relative to PM) and more radiogenic (enriched relative to PM) mantle components (Hart, 1988, Hart *et al.*, 1992, Hofmann, 1997, Zindler & Hart, 1986). OIB which exhibit low $^{143}Nd/^{144}Nd$, $^{176}Hf/^{177}Hf$ and high $^{87}Sr/^{86}Sr$ isotope ratios, and therefore plot within the enriched quadrants in Hf-Nd-Sr isotope space, are referred to as EM-type OIB (Salters & White, 1998, Weaver, 1991, Zindler & Hart, 1986).

The Gough Island OIB are a prime example of lavas produced from an enriched mantle (EM) source region (White & Hofmann, 1982). le Roex (1985) studied the fractional crystallisation processes involved in the production of these lavas, but not the partial melting processes. Therefore, this study aims at interpreting the partial melting processes involved in producing these lavas, using geochemical principles, which are subsequently used to make inferences on the chemical and mineralogical nature as well as the production of an EM-type mantle source region.

1.2 The Hafnium Isotope System

An important tool in understanding mantle geochemistry is the use of radiogenic isotope systems, such as the Sm-Nd, Rb-Sr, U-Pb and Lu-Hf isotope systems (e.g. Gast *et al.*, 1964 Patchett *et al.*, 1984, White & Hofmann, 1982), as geochemical tracers (Hofmann, 1997). Parent-daughter isotope

ratios are able to record information of ancient enrichment or depletion events in the mantle as unstable parent isotopes decay into more stable daughter isotopes thus changing the radiogenic/stable isotope ratios as a function of time (Patchett *et al.*, 1984). The behaviour of individual isotope systems differs during different Earth processes, and therefore by comparing one isotope system to another it is possible to ascertain the nature and timing of specific processes which may have occurred (Hofmann, 1997, Patchett *et al.*, 1984). Isotopes ratios, like incompatible trace element ratios, are unaffected by melting and crystallisation processes and therefore are a direct representation of the primary magma composition and the mantle source region (Hofmann, 1997).

Since some OIB exhibit isotope compositions more enriched relative to PM, it has been argued that OIB form as a result of mixing processes between a typical depleted mid-ocean ridge mantle (DMM) composition (convecting asthenospere) and a more isotopically enriched component (Hart, 1988, Hart *et al.*, 1992, Hofmann, 1997, Zindler & Hart, 1986). It has been proposed that sediment and oceanic crustal recycling could be the possible missing enriched component, as marine sediments are constantly recycled back into the mantle through subduction zones and are isotopically enriched (Andres *et al.*, 2002, Chauvel *et al.*, 1992, Eisele *et al.*, 2002, Salters & White, 1998, White & Hofmann, 1982). Another suggestion for the enriched component is sub-continental lithospheric mantle (SCLM) which is argued, by some, to be present in the shallow mantle as a result of continental break-up, or mechanically abraded from the upper plate in a subduction zone, recycled and injected into the shallow mantle (Class & le Roex, 2006, Milner & le Roex, 1996, Willbold & Stracke, 2006). Other methods that have been proposed for producing an EM-type mantle involve metasomatic processes (Pilet *et al.*, 2005) and even recycling of oceanic plateaus (Gasperini *et al.*, 2000).

The Hf-isotope system is a particularly powerful diagnostic tool in understanding sediment recycling processes. This is because of the ability of Hf and Nd isotopes to decouple as a result of preferential partitioning of Hf into the mineral zircon (known as the zircon effect) (Patchett *et al.*, 1984). This results in recycled zircon-rich (terrigenous) or poor (pelagic) sediments developing different $^{176}Hf/^{177}Hf$ isotope ratios over time and results in decoupling of the Hf and Nd isotope systems. Subsequent mixing of recycled sediments with a mantle source region results in the mantle source region inheriting a unique isotope signature.

1.3 Petrogenesis of the Gough Island Suite of Lavas

Peridotite, composed of olivine, clinopyroxene, orthopyroxene and garnet or spinel, is the most common rock type in the upper mantle (Jaques & Green, 1980, Kushiro, 1968, Ringwood, 1975, Sun & McDonough, 1995) and therefore basaltic melts, such as OIB, derived from the upper mantle have long thought to be the product of partial melting of peridotite (Kushiro, 1968, Takahashi, 1986). However, recently it has been suggested that eclogite and pyroxenite may be present in the source

regions of some OIB, such as Hawaii (Sobolev *et al.*, 2007, Sobolev *et al.*, 2005). The presence of eclogite in the shallow mantle is argued to occur by the incorporation of recycled oceanic crust into rising plumes (Sobolev *et al.*, 2007).

Constrained forward modelling methods are used to determine the chemical and mineralogical nature as well as the melting parameters required to produce the Gough Island lavas. Feigenson *et al.* (1996) introduced the concept of constrained forward modelling by attempting to constrain melting processes involved in producing the Mauna Kea basalts. This modelling involves calculating a range of REE patterns produced by the partial melting of a calculated theoretical mantle source region composition using various melting parameters. The calculated range of REE patterns are subsequently compared to the calculated Gough Island primary magma compositions in order to determine which set of melting parameters and source region composition are able to most satisfactorily account for the trace element geochemistry of the Gough Island lavas.

1.4 Evolution of the Gough Island Mantle Source Region

Earlier studies of the Gough Island suite of lavas have all argued for the interaction of the mantle source region with another component. le Roex (1985) argued, based on trace element data, that the Gough Island mantle source region must have been enriched relative to a more depleted MORB source region. Willbold & Stracke (2006) argued that the trace element geochemistry of the Gough Island lavas can be explained by a recycled oceanic lithosphere component with variable upper and lower continental crust. Class & le Roex (2008) argued, based on Ce anomalies, that the Gough Island mantle source region interacted with a recycled sediment component which had previously experienced near-surface interaction with ocean-water.

Binary mixing curves are used to assess whether the Gough Island lavas could be produced through the interaction of a mantle source region with a recycled sediment component, SCLM or lower crust. Mixing curves are calculated between a typical OIB mantle source region composition and SCLM, lower crust and modern marine sediment using $^{176}Hf/^{177}Hf$, $^{143}Nd/^{144}Nd$ and $^{87}Sr/^{86}Sr$ isotope ratios, Ba/Nb and Zr/Nb ratios as well as Ce-anomalies.

1.5 Objectives

OIB pass through the oceanic crust which implies that they have experienced less contamination by country rock than lavas which pass through continental crust and therefore are important in mantle studies (Green & Ringwood, 1967, Hofmann, 1997, Yoder, 1976). The Gough Island lavas are, in some aspects, anomalous in comparison to other global OIB (e.g. Hf, Nd and Sr isotope and Ba/Nb trace element ratios), which suggests derivation from a complex mantle source region. Therefore, this study aims at exploring the geochemical nature and petrogenesis of the basaltic lavas from Gough Island, as well as the evolution of the underlying mantle source region.

This is accomplished using previously measured major and trace element data as well as $^{143}Nd/^{144}Nd$ and $^{87}Sr/^{86}Sr$ isotope data in conjunction with newly acquired $^{176}Hf/^{177}Hf$ isotope data for the Gough Island and the McNish Seamount lavas. These data are used to explore differences between individual lava flows within the Gough Island lavas, as well as between the lavas of Gough Island, the McNish Seamount and the geographically close islands of Tristan da Cunha and Inaccessible Island. Subsequently, the petrogenesis and evolution of the Gough Island mantle source region is modelled through the use of constrained forward modelling and binary mixing calculations.

2 Geological Setting

2.1 Gough Island

Gough Island is located in the south Atlantic Ocean (40°19'S; 09°56'W) approximately 400km southeast of Tristan da Cunha and 2700km southwest of Cape Town, located on ~34Ma crust of the African Plate (le Maitre, 1960, le Roex, 1985). It is a small island with a length of thirteen kilometres and a width of six kilometres, rising from a depth of -3500m and reaching a maximum altitude of 970m at Edinburgh Peak (le Roex, 1985, Maund *et al.*, 1988). The island has a rugged topography with small pebble-boulder beaches and large cliff faces, with numerous young, v-shaped valleys with dense fern-type vegetation below 300m (le Maitre, 1960).

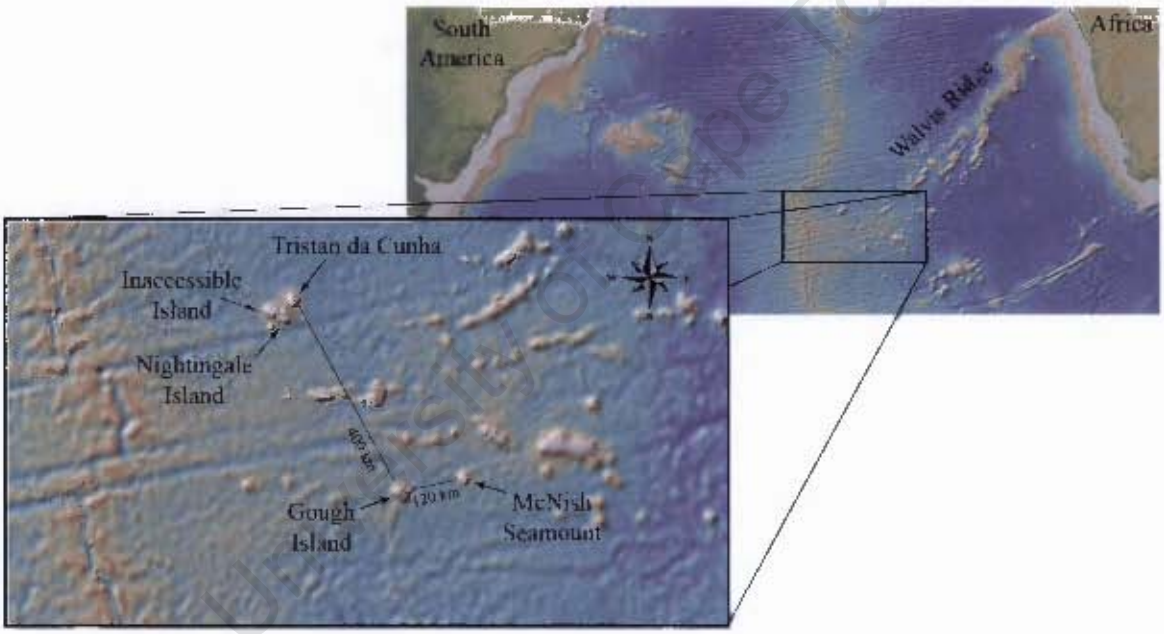

Fig 2-1: Topographic map showing in detail the location of the Tristan da Cunha group of islands (i.e. Tristan da Cunha, Inaccessible Island and Nightingale Island) as well as the location of Gough Island and the McNish Seamount. Map created using GeoMapApp (http://www.geomapapp.org).

The island was first discovered in the sixteenth century by a Portuguese navigator by the name of Gonçalo Alvarez and named Diego Alvarez (Carroll, 2003). After a period of time and due to a lack of accurate co-ordinates, the island was lost and rediscovered in 1731 by Captain Gough and subsequently renamed Gough Island (Carroll, 2003, le Maitre, 1960). The name Diego Alvarez was dropped and today the island is known as Gough Island.

In November 1955, an eight-man expedition (Gough Island Scientific Expedition) arrived at Gough Island to complete a detailed map of the island as well as to perform a detailed study of the island's geology, vegetation and animal life. The first investigation into the island's geology was

performed by R.W. le Maitre who also produced the first geological map (le Maitre, 1960) and the first comprehensive petrographic study (le Maitre, 1962). Later visits to the island, in 1978 and 1986, led to a more detailed description of the geochemistry of the lavas (le Roex, 1985) and a revised geological map (Maund *et al.*, 1988).

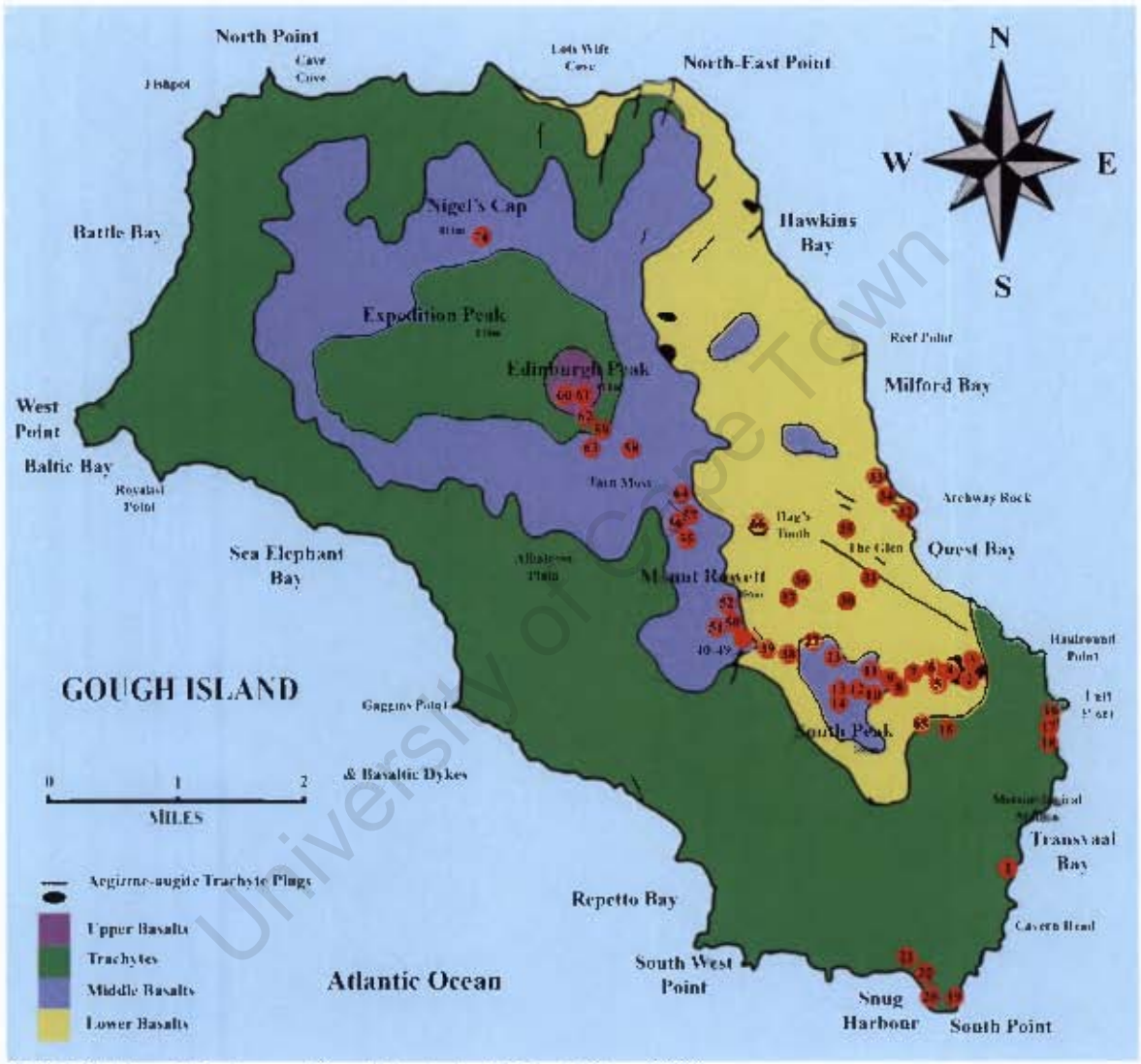

Fig 2-2: Sketch geological map of Gough Island adapted from le Roex (1985)

The first studies by le Maitre (1960, 1962) on Gough Island suggested that the island was Tertiary in age since it showed the same degree of erosion as St Helena and that the island consisted of cyclical units of basalt and trachyte lavas. le Maitre (1960) described five main stratigraphic units - Lower, Middle and Upper Basalts as well as Lower and Upper Trachytes.

By using K-Ar dating, Miller (1964) determined the volcanic activity to be 2-6Ma, but this was later revised to 2.5-0.1Ma by Maund *et al.*, (1988) based on high-precision K-Ar dating and field work. Maund *et al.*, (1988) found that there were four different periods of volcanic activity; eruption of the older basalt group (2.5-0.5Ma), intrusion of aegerine-augite trachyte plugs (0.8-0.47Ma),

eruption of trachyte lavas (0.3-0.12Ma) and the final eruption of the youngest Edinburgh Basalts (0.2-0.13Ma). As a result, the stratigraphy of Gough Island was revised (Maund *et al.,* 1988) and is summarised in Table 2-1.

Table 2-1: Revised Gough Island stratigraphy. Ages are only general approximations.

Maund *et al.*, (1988)	Age (Ma)
Edinburgh Peak Basalts	0.1
Trachytes	0.2
Rowett Basalts	0.5
Aegirine-Augite Trachyte Plugs	0.8
Glen Basalts	1.0
Reef Point Basalts	2.5

2.2 Previous Work

Whole rock rare-earth element (REE) abundances on the Gough Island suite of lavas were first measured by Zielinski & Frey (1970) for a limited number of samples in order to test a fractional crystallisation model. They determined that the major and trace element trends in the Gough Island lavas can be explained by fractional crystallisation of olivine, pyroxene, feldspar and apatite. le Roex (1985) subsequently performed a more detailed determination of major, trace element and mineral compositions to evaluate possible petrogenetic relationships between lava flows and major geological units, and to make inferences on the geochemical nature of the mantle source region giving rise to the lavas. le Roex (1985) concluded that the Upper and Lower Basalts have a restricted compositional range compared to the Middle Basalts and the lavas have experienced up to 40% crystal fractionation of clinopyroxene, olivine, plagioclase with minor fractionation of Fe-Ti oxides and apatite. More recently, Willbold & Stracke (2006) also made inferences on the nature of the Gough Island mantle source region and argued that the trace element signatures of the Gough Island suite of lavas can be explained by the recycling of an oceanic lithosphere component with variable upper and lower continental crust. Helium, lead, strontium, neodymium and oxygen isotope data have been determined on a limited number of Gough Island samples in the past (Gast *et al.*, 1964, Harris *et al.*, 2000, Kurz *et al.*, 1982, le Roex, 1985, White & Hofmann, 1982). The Gough Island lavas has never been analysed for Hf isotopes.

3 Analytical Techniques

The major element data for the Gough Island sample set used in this study were published in le Roex (1985), whereas newly acquired high precision trace element data as well as Nd and Sr isotope data are from Class & le Roex (2008). Operating conditions and analytical procedures used in acquiring the $^{143}Nd/^{144}Nd$ and $^{87}Sr/^{86}Sr$ isotope ratios as well as the major and trace element concentrations are given in Class & le Roex (2008).

Hf-isotope data were acquired on an AXIOM MC-ICP-MS at L-DEO (New York, USA). Samples were prepared by a two-stage process which first involved the initial sample digestion using a 2.65ml ~3:1 conc. HF:HNO_3 solution, followed by a Lu-Hf purification stage using reversed phase cation exchange one-column chromatography on EICHROM Ln-Spec® resin (following the method adapted from Münker *et al.*, (2001) at L-DEO (Cai, in prep.; see Appendix B for a detailed discussion of sample preparation methodology)). Instrument stability and drift were monitored prior to and during sample analysis by bracketing every sample with a 500ppb Specpure standard. Samples were diluted to approximately 500ppb total Hf in order to produce similar voltage across the cups as the 500ppb Specpure standard. The dilution factors varied from one set of samples to another as a result of varying percentage yields of Hf during sample preparation. Measurements over a two year span (7 repeat analyses) of the in-house standard, K1919, yielded an average value of 0.283106 with an external 2σ standard deviation of $9x10^{-6}$ (61ppm) which is within error of published values of 0.283116 ± 4 (Blichert-Toft *et al.*, 1999) and 0.283096 ± 7 (Münker *et al.*, 2001). Hf measurements were normalised to a $^{176}Hf/^{177}Hf$ ratio of 0.28216 for JMC-475 so as to be comparable with other published hafnium isotope data.

4 Petrography

le Maitre (1962) was the first to complete a petrographic study of the Gough Island lavas and recognised six different rock types, namely picrite basalts, olivine basalts, trachybasalts, trachytes and aegirine-augite trachytes which were categorised into five main stratigraphic units – Lower, Middle and Upper Basalts as well as the Lower and Upper Trachytes. Later, le Roex (1985) recognised, based on petrography, that three different varieties of olivine basalts exist in the Gough Island lavas, these include the coarsely pyroxene-olivine phyric basalts, moderately pyroxene-olivine phyric basalts and aphyric to finely porphyritic basalts.

Thirty-eight olivine basalts, trachybasalts and basaltic trachyandesites were used in this study (the trachytes were not considered for this study). This chapter provides a brief petrographic overview of the three different stratigraphic units of basaltic lavas focusing on the more primitive lavas (see Appendix A for detailed individual petrographic descriptions).

4.1 Lower Basalts

The ten samples from the Lower Basalt series consist of basalt, trachybasalt and basaltic trachyandesite as determined by a total-alkali silica diagram (TAS diagram; Fig 5-1). The Lower Basalts are composed of two petrographically distinct lavas, with both groups ranging from aphyric through finely to coarsely porphyritic. The first of these lava groups have 0.5-10mm anhedral to euhedral olivine (10-60% modal abundance) as a major phenocryst phase with minor phenocrysts of 0.5 to 4mm anhedral to subhedral clinopyroxene (5-10% modal abundance) and 2-4mm plagioclase (5-10% modal abundance). The second lava type consists of 2-8mm anhedral to subhedral clinopyroxene (10-30% modal abundance) as a major phenocryst phase with 2-4mm plagioclase and minor 0.5-2mm subhedral olivine (5-20% modal abundance) as the other phenocryst phases. The plagioclase (and to a lesser degree, the clinopyroxene and olivine) phenocrysts in both lava types commonly exist as glomerocrysts and cumulocrysts of up to 10 individual mineral grains. The lavas are vesicular with vesicles ranging in size from 0.5-4mm in diameter. ALR32G and ALR33G (both trachyandesites) are unique as they also contain phenocrysts of titanomagnetite which range in size from 0.5 to 2mm in diameter. All the Lower Basalts exhibit an intergranular texture where the matrix minerals include olivine, plagioclase, clinopyroxene, titanomagnetite, ilmenite and apatite. Four of the lower basalt lavas are fresh with minimal signs of alteration, whereas the remainder of the samples exhibit evidence for limited hydrothermal alteration and development of indingsite and/or bowlingsite after olivine.

Figure 4-1: Photomicrographs of selected samples from the Lower Basalts. a) subhedral to euhedral olivine phenocryst (PPL, ALR6G) b) cumulocryst of anhedral to subhedral olivine grains which show slight alteration to iddingsite (red) along grain boundaries and fractures (PPL, ALR33G) c) subhedral olivine phenocrysts with extensive grain boundary alteration to iddingsite (PPL, ALR35G) d) plagioclase and titanomagnetite phenocryst (XPL, ALR33G). PPL – plane polarized light; XPL – polarized light.

4.2 Middle Basalts

Twenty-seven samples are from the Middle Basalt series and form the largest group of lavas analysed in this study. The Middle Basalts consist of basalt, trachybasalt and trachyandesite as determined by a TAS diagram (Fig 5-1). These samples range from aphyric through finely to coarsely porphyritic and can be petrographically divided into two main groups. The first lava group has 0.5-5mm anhedral to euhedral olivine (5-60% modal abundance) as a major phenocryst phase with 0.5-8mm anhedral to subhedral clinopyroxene (5-30% modal abundance) and 0.5-6mm plagioclase (2-30% modal abundance) as minor phenocryst phases. The second lava type (two samples) has 0.5-4mm anhedral to subhedral olivine (1-5% modal abundance) as a minor phenocryst phase with the major phenocryst phases consisting of 0.5-8mm anhedral to subhedral clinopyroxene (5-20% modal abundance) and 6mm plagioclase (10% modal abundance). Both groups of lavas exhibit glomerocrysts and cumulocrysts of primarily plagioclase but also occasionally with clinopyroxene and olivine, where the glomerocrysts and cumulocrysts consist of up to ten individual mineral grains. All of the samples are vesicular with the vesicles ranging in size from 0.5-6mm in diameter. All the samples exhibit an intergranular texture where the matrix minerals include olivine, plagioclase, clinopyroxene, titanomagnetite, ilmenite and apatite. Six of the Middle Basalt lavas are

petrographically fresh with minimal evidence of alteration, whereas the remainder of the samples exhibit limited hydrothermal alteration minerals of iddingsite and/or bowlingsite after olivine.

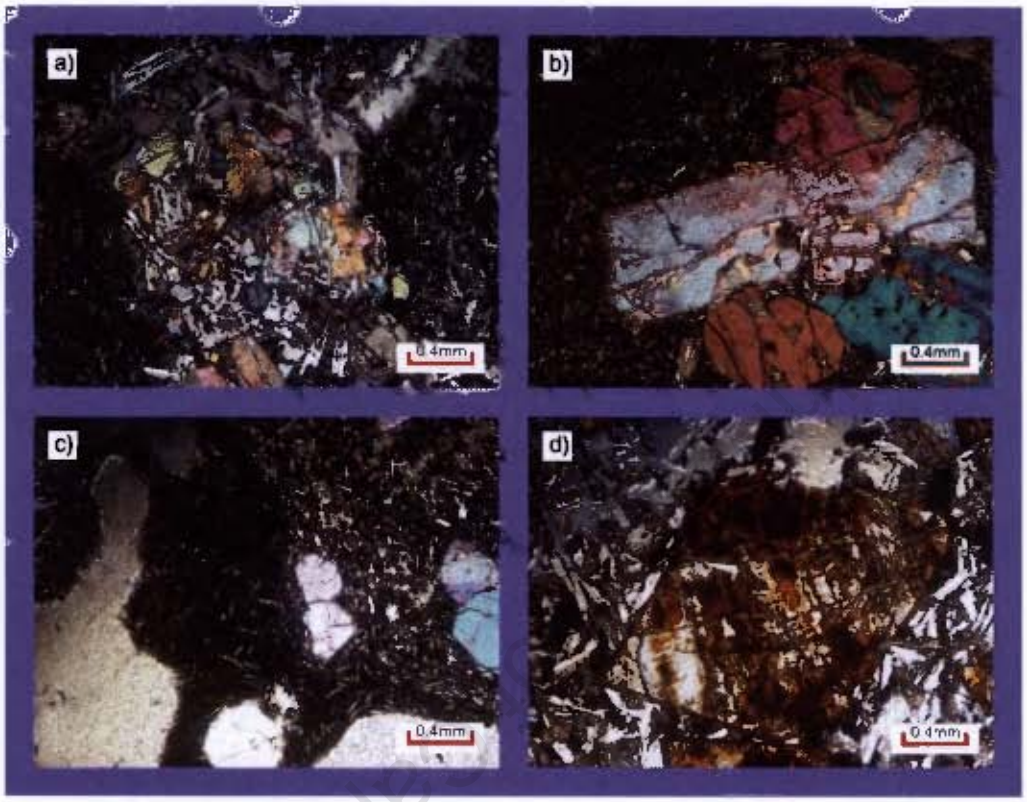

Figure 4-2: Photomicrographs of selected samples from the Middle Basalts. a) Glomerocryst of anhedral olivine, clinopyroxene and plagioclase grains (XPL, ALR10G) b) Cumulocryst of randomly orientated clinopyroxene grains (XPL, ALR14G) c) Vesicle with chill margin. (XPL, ALR24G) d) euhedral olivine phenocryst with extensive alteration to iddingsite (PPL, ALR43G).

4.3 Upper Basalts

Only one sample of the Upper Basalts was used in this study (ALR63G) and plots within the basaltic trachyandesite field on a TAS diagram (Fig 5-1). This sample is moderately porphyritic and contains phenocrysts of 0.5-4mm anhedral to euhedral olivine (25% modal abundance) and 1mm plagioclase (5% modal abundance). Vesicles are also present in this sample and are 0.5mm in diameter. The sample has an intergranular texture, where the matrix minerals are composed of olivine, plagioclase, clinopyroxene, titanomagnetite, ilmenite and apatite. This sample is fresh and with little evidence of weathering or hydrothermal alteration.

5 Bulk Rock Geochemistry

5.1 Introduction

The first detailed geochemical study of the Gough Island lavas was performed by Zielinski & Frey (1970) who measured whole rock REE abundances on a different sample set from the one used in this study. Later, le Roex (1985) performed a more detailed determination of major and trace element abundances on a newly acquired sample set (the same sample set used in this study). Recently, Class & le Roex (2008) collected high precision Inductively Coupled Plasma Mass Spectrometry (ICP-MS) trace element data, at the University of Cape Town (UCT), for the same sample set, which were made available for use in this study. As a result, the major element data are taken from le Roex (1985) whereas the trace element data are from Class & le Roex (2008).

The McNish Seamount (40°10'S; 08°31'E) is located ~120km to the north-east of Gough Island and dredge samples were collected in 1987 by SA Agulhas (Cruise Number 51). The major and trace element data for the three samples were acquired by X-Ray Fluorescence Spectrometry (XRF-S) and ICP-MS methods (same method as used by le Roex (1985) and Class & le Roex (2008); Class & le Roex, unpublished data) at the University of Cape Town and made available for use in this study.

This chapter is aimed at introducing, comparing and discussing the bulk rock major and trace element geochemistry for each of the Lower, Middle and Upper Basalts of the Gough Island lavas and to compare these lavas with the McNish Seamount lavas.

5.2 Major Element Geochemistry

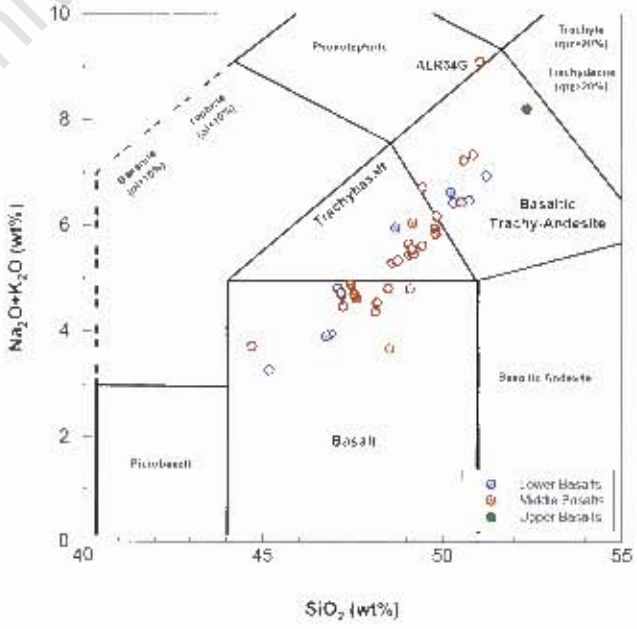

Fig 5-1: (Na_2O+K_2O) vs. SiO_2 (TAS) diagram showing compositional variation within the Gough Island lavas.

Major element analyses of the Gough Island lavas are given in Table 5-1 and are illustrated in a total-alkali silica (TAS) diagram (Fig 5-1) and selected variation diagrams (Fig 5-2). A plot of SiO_2 versus Na_2O+K_2O (TAS diagram) indicates that the Gough Island lavas is composed of alkali basalts, trachybasalts and basaltic trachyandesites and thus form an alkali basalt-trachyte series (Fig 5-1 trachytes not shown on the TAS diagram as they do not form part of the sample set used in this study). Both the Lower and Middle Basalts range from basalt to basaltic trachyandesites in composition whereas the single Upper Basalt sample plots within the basaltic trachyandesite field and is the most evolved sample out of this sample set. The Middle Basalt array is less tightly constrained than the Lower Basalt array. Overall there is no distinct grouping or variation of composition or trend between each of the different groups based on the TAS diagram.

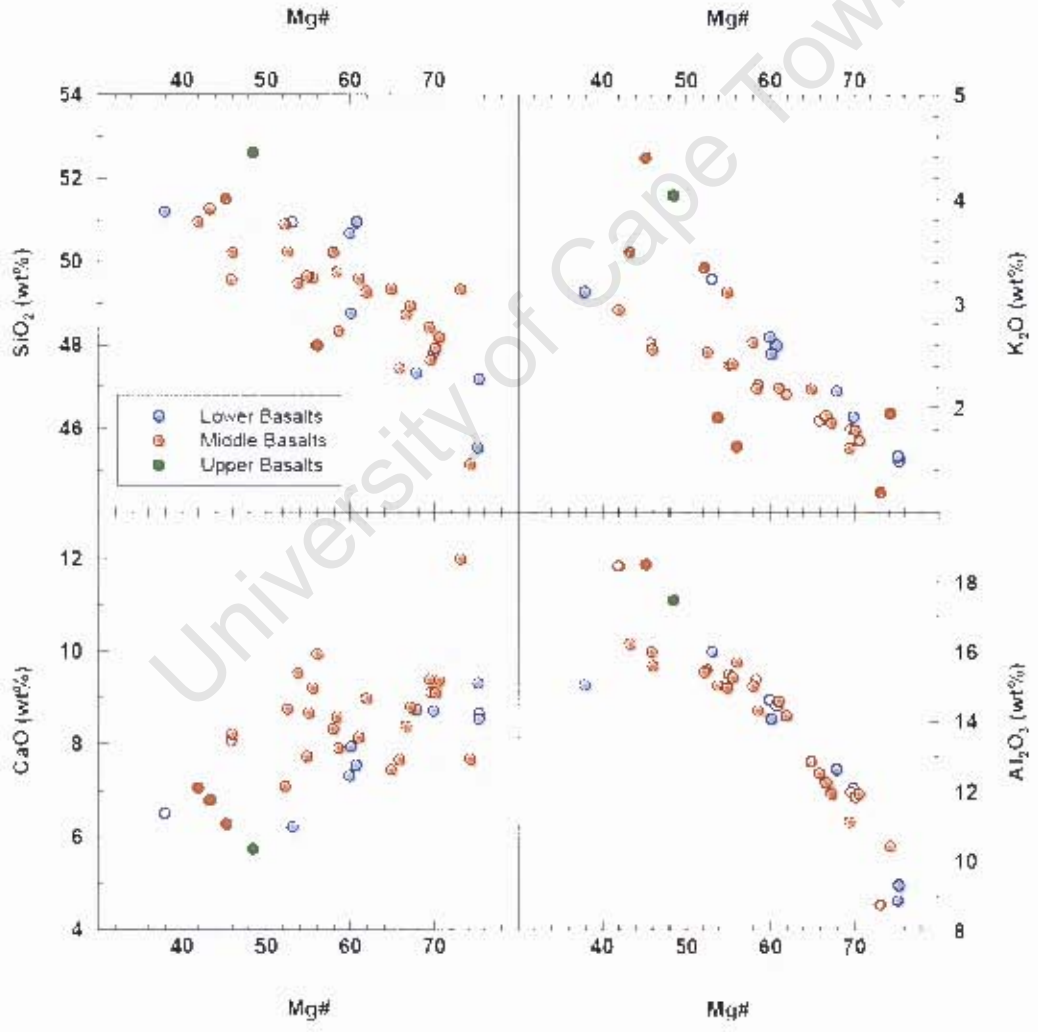

Fig 5-2: Variation of selected major element oxides with Mg# (where Mg# atomic $100Mg/(Mg+Fe^{2+})$).

SiO_2 (45.2-52.6 wt%), K_2O (1.19-4.39 wt%) and Al_2O_3 (8.76-18.5 wt%) all exhibit a negative correlation with Mg# (Mg# ranges from 37.9 to 75.3; FeO ranges from 6.46 to 10.2 wt% and MgO ranges from 3.05 to 17.3 wt%), whereas CaO (5.74-12.0 wt%) exhibits a scattered positive correlation

with Mg# (see Fig 5-2). The steady increase in Al_2O_3 with increasing differentiation (i.e. decreasing Mg#) for both the Lower and Middle Basalts indicates that plagioclase was not an important fractionating phase; this is confirmed by a gradual increase in Na_2O with increasing differentiation. Clinopyroxene appears to have been an important fractionating phase during magma differentiation as the CaO content of the lavas decreases gradually with increasing differentiation.

Table 5-1: XRF-S major element analyses for the Lower, Middle and Upper Basalts of the Gough Island suite of lavas. Data from le Roex (1985).

	ALR85G	ALR7G	ALR27G	ALR80G	ALR32G	ALR33G	ALR35G	ALR36G	ALR37G	ALR38G	ALR6G	ALR8G	ALR9G
Strat.	LB	LB	LB	LB	LB	LB	LB	LB	LB	LB	MB	MB	MB
SiO_2	47.17	47.19	47.34	50.95	50.63	50.95	48.78	51.21	45.55	47.81	49.46	49.56	49.56
TiO_2	2.11	2.09	2.06	2.50	3.11	3.04	3.40	2.73	2.17	2.60	3.24	3.85	3.24
Al_2O_3	9.32	9.31	12.64	16.00	14.62	14.44	14.08	16.04	8.88	12.10	15.03	16.00	15.35
Fe_2O_3	1.90	1.91	1.84	1.53	1.66	1.67	1.75	1.71	1.96	1.86	1.78	1.73	1.64
FeO	9.52	9.67	9.19	7.51	8.28	8.37	8.77	8.63	9.32	9.28	8.92	8.63	8.16
MnO	0.16	0.16	0.16	0.12	0.13	0.13	0.13	0.13	0.18	0.15	0.15	0.15	0.14
MgO	16.92	17.19	11.32	4.96	7.23	7.55	7.71	3.07	17.38	12.55	5.05	4.26	5.84
CaO	8.67	8.54	8.74	6.22	7.33	7.55	7.94	6.50	9.31	8.72	9.55	8.06	8.67
Na_2O	2.43	2.45	2.65	3.27	4.01	3.91	3.44	3.83	1.75	2.62	2.92	3.48	3.22
K_2O	1.53	1.49	2.16	3.03	2.68	2.60	2.52	3.11	1.54	1.92	1.91	2.52	2.41
P_2O_5	0.38	0.37	0.52	0.78	0.80	0.75	0.80	0.97	0.36	0.53	0.55	0.71	0.62
LO	0.32	0.39	0.56	2.49	0.36	0.32	0.56	2.33	1.01	0.64	0.86	1.17	0.92
Total	100.50	100.90	100.50	100.40	100.90	101.30	100.20	99.97	100.80	101.50	100.80	100.80	100.40
Mg#	75.20	75.30	67.86	53.10	59.04	60.73	60.12	37.87	75.16	69.87	53.77	47.82	55.02

	ALR10G	ALR12G	ALR13G	ALR14G	ALR23G	ALR24G	ALR34G	ALR40G	ALR41G	ALR43G	ALR44G	ALR45G	ALR46G
Strat.	MB	MB	MB	MB	MB	MB	MB	MB	MB	MB	MB	MB	MB
SiO_2	49.27	47.90	50.24	49.50	50.23	45.[illegible]	51.51	48.24	49.34	47.42	48.73	48.34	48.95
TiO_2	3.00	3.26	3.26	3.24	3.54	2.45	2.16	2.58	2.27	2.87	2.81	3.21	2.77
Al_2O_3	14.16	15.70	15.49	15.26	15.59	10.42	18.50	11.12	8.76	12.32	12.25	14.11	11.93
Fe_2O_3	1.71	1.72	1.53	1.68	1.71	7.04	1.79	1.85	1.76	1.97	1.89	1.81	1.90
FeO	8.54	8.59	8.14	8.39	8.64	10.18	6.46	9.24	8.82	9.87	9.43	9.06	9.49
MnO	0.14	0.15	0.14	0.14	0.14	0.18	0.13	0.15	0.16	0.16	0.16	0.15	0.17
MgO	8.09	6.39	5.25	6.10	4.29	17.11	3.10	12.22	13.97	11.11	10.99	7.47	11.33
CaO	8.99	9.04	8.76	9.21	8.22	7.58	6.28	9.40	12.00	7.67	8.38	7.91	8.80
Na_2O	3.33	3.02	3.46	3.29	3.37	1.80	4.79	2.77	2.53	3.01	2.89	3.04	2.75
K_2O	2.13	1.63	2.53	2.42	2.56	1.05	4.39	1.62	1.19	1.88	1.91	2.22	1.86
P_2O_5	0.56	0.53	0.65	0.63	0.65	0.47	1.04	0.46	0.34	0.51	0.49	0.60	0.46
LOI	0.32	1.47	0.92	0.85	0.94	0.96	0.82	0.49	0.48	0.72	0.41	0.94	0.59
Total	100.40	100.80	100.90	101.10	100.80	101.30	100.90	100.60	101.70	99.96	100.50	99.46	101.60
Mg#	61.88	56.04	52.60	55.48	45.97	74.23	45.14	69.39	73.09	65.87	66.63	58.57	67.17

	ALR47G	ALR48G	ALR49G	ALR50G	ALR51G	ALR52G	ALR53G	ALR54G	ALR55G	ALR56G	ALR64G	ALR63G	
Strat.	MB	MB	MB	MB	MB	MB	MB	MB	MB	MB	MB	UB	
SiO_2	49.35	49.55	50.90	49.74	47.64	49.64	51.27	50.97	47.93	48.19	50.24	52.61	
TiO_2	3.02	3.18	2.87	2.97	2.74	3.09	3.25	2.92	2.74	2.77	2.99	2.38	
Al_2O_3	12.85	14.58	15.41	15.21	11.98	14.96	16.27	18.46	11.83	11.93	15.02	17.47	
Fe_2O_3	1.93	1.75	1.67	1.71	1.82	1.73	1.67	1.45	1.88	1.85	1.65	1.37	
FeO	9.63	8.77	8.36	8.57	9.10	8.67	8.37	7.24	9.40	9.27	8.26	6.83	
MnO	0.16	0.15	0.13	0.15	0.16	0.15	0.14	0.12	0.16	0.16	0.14	0.12	
MgO	10.38	8.00	5.32	7.01	12.11	6.14	3.72	3.05	12.87	12.98	6.54	3.75	
CaO	7.46	8.14	7.11	8.59	9.11	7.73	6.80	7.06	9.11	9.39	8.42	5.74	
Na_2O	3.21	3.31	3.94	3.44	2.91	3.64	3.91	3.56	3.01	2.86	3.59	4.20	
K_2O	2.18	2.19	3.34	2.18	1.80	3.11	3.49	2.94	1.79	1.69	2.53	4.04	
P_2O_5	0.57	0.59	0.90	0.59	0.44	0.74	0.80	0.69	0.43	0.43	0.61	0.84	
LOI	0.34	0.40	0.44	0.65	0.30	0.58	0.95	1.57	0.29	0.35	0.47	0.78	
Total	101.20	100.80	100.60	101.20	100.20	100.40	100.80	100.90	101.30	102.00	100.80	100.50	
Mg#	64.87	61.00	52.17	58.38	59.52	54.84	43.25	41.93	70.12	70.60	57.95	48.47	

Strat. refers to samples stratigraphic unit where LB = Lower Basalt; MB = Middle Basalt; UB = Upper Basalt. All major element oxides given as wt%. Mg# atomic 100Mg/(Mg/Fe2+) with Fe2O3/FeO=0.20.

The single Upper Basalt sample (ALR63G) exhibits high SiO_2 (52.6 wt%), Al_2O_3 (17.5 wt%) and K_2O (4.04 wt%) and low CaO (5.74 wt%) abundances, and therefore plots at the more differentiated end of the Lower Basalt array in major element variation diagrams. TiO_2 (2.09-3.85 wt%) exhibits a tight negative correlation with Mg# greater than 54 and a scattered positive correlation with lower Mg#, indicating the increasing importance of fractionating Fe-Ti oxides with increasing differentiation. P_2O_5 (0.34-1.04 wt%) and Na_2O (1.75-4.79 wt%) exhibits a negative correlation with Mg# where the Lower Basalts have higher P_2O_5 and Na_2O content for a given Mg# than the Middle Basalts. The gradual increase in P_2O_5 with increasing differentiation indicates the minimal importance of apatite as a fractionating phase in these lavas.

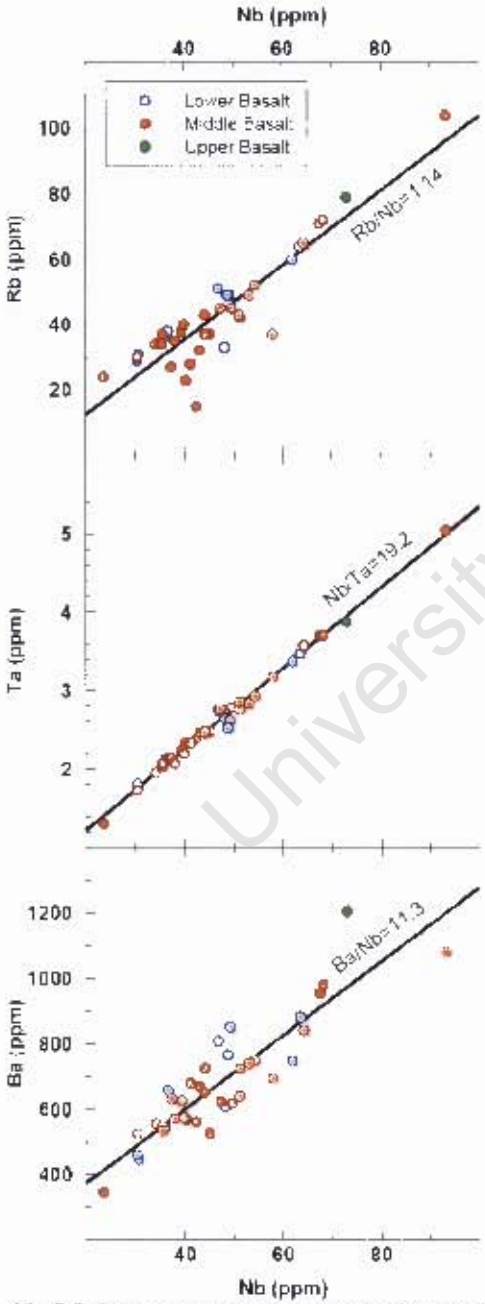

Fig 5-3: Variation of the incompatible elements Rb, Ta and Ba with Nb for the Lower, Middle and Upper Basalts of the Gough Island lavas. Solid black line is a line of best fit calculated using only the Gough Island lavas (the gradient of the best fit line is shown alongside).

5.3 Trace Element Geochemistry

Trace element data for the Gough Island suite of lavas are reported in Table 5-2 and variation diagrams of selected trace elements are shown in Fig 5-3, Fig 5-4 and Fig 5-5.

The abundances of the incompatible trace elements Ba (346-1205ppm), Ta (1.31-5.05ppm), Nb (23.5-93.1ppm) and Rb (14.8-104ppm) are all high with Ba, Rb and especially Ta exhibiting a strong positive correlation with Nb (Fig 5-3; Rb exhibits more scatter at Nb abundances below ~60ppm and Rb abundances less than ~50ppm). The Lower and Middle Basalts have a similar range in incompatible trace element abundances and therefore the arrays for each of these groups are superimposed. The single Upper Basalt sample (ALR63G) has high incompatible trace element abundances and plots at the differentiated end of the Lower and Middle Basalt arrays. As a result of the high abundance of Ba in the Gough Island lavas, the Ba/Nb (11.6-18.0) ratio for these lavas is high, and the Zr/Nb and La/Nb ratio ranges from 4.5 to 7.3 and 0.84 to 1.18, respectively.

The incompatible trace elements Hf (3.68-8.65ppm), Y (16.3-34.2ppm), Ce (51.4-155ppm) and

Sr (425-1013ppm) exhibit a large range (especially Ce) and are high in absolute abundance. Sr and Y both exhibit broad positive correlations with Zr which breaks down at Zr abundances greater than ~300ppm, whereas Ce and Hf exhibit strong positive correlations with Zr for the entire range of Zr concentration (Fig 5-4). The Lower and Middle Basalts have similar abundances of these trace elements and therefore the Lower and Middle Basalt arrays are superimposed, except in Y vs. Zr where the Lower Basalts plot at lower Y values for a given Zr concentration. The single Upper Basalt sample (ALR63G) has high moderately incompatible trace element abundances and plots at the differentiated end of the Lower and Middle Basalt arrays. The Zr/Hf ratios for Gough Island range from 44.5-54.0 and the Nb/Ta ratio ranges from 16.8 to 19.3. The Y/Nb and Ce/Pb ratios range from 0.28-0.82 and 18.5-34.0, respectively. The $(La/Sm)_N$ and $(La/Yb)_N$ ratios range from 2.55-5.08 and 11.8-30.5, respectively (values normalised to chondritic values of Sun & McDonough (1989)).

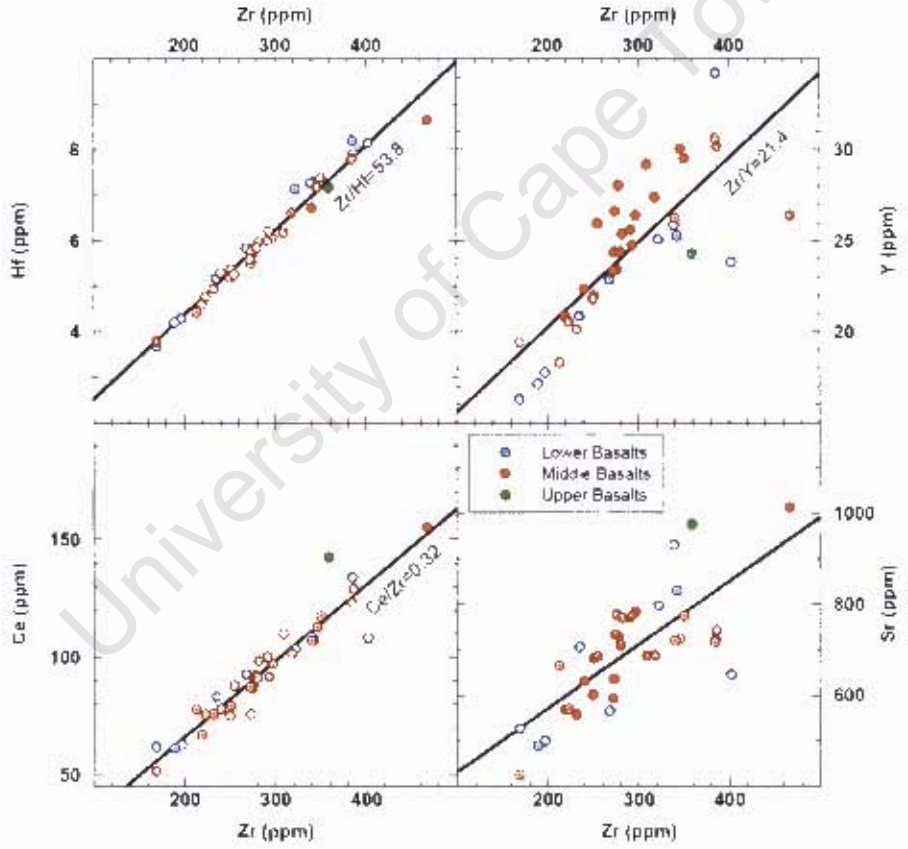

Fig 5-4: Variation of the incompatible trace elements Hf, Y, Ce and Sr with Zr for the Lower, Middle and Upper Basalts of the Gough Island suite of lavas. Solid black line is a line of best fit calculated using all the Gough Island lavas (the gradient of the best fit line is shown alongside).

The compatible ferro-magnesian trace elements Co (20-90ppm), Ni (8.50-649ppm) and Cr (11.4-1020ppm) exhibit a large range in absolute abundances and decrease systematically with increasing differentiation (i.e. decreasing Mg#; Fig 5-5). The Co, Ni and Cr abundances of the Lower and Middle Basalts are similar and therefore these arrays are superimposed in variation diagrams of Co, Ni and Cr vs. Mg#. The single Upper Basalt sample (ALR63G) has similar abundances of Co, Ni

and Cr as the Lower and Middle Basalts, and therefore plots within the Lower and Middle Basalt arrays. The overall decrease in abundance of these compatible trace elements indicates the importance of the continuous fractionation of ferro-magnesian minerals (such as olivine and clinopyroxene) with increasing magma differentiation.

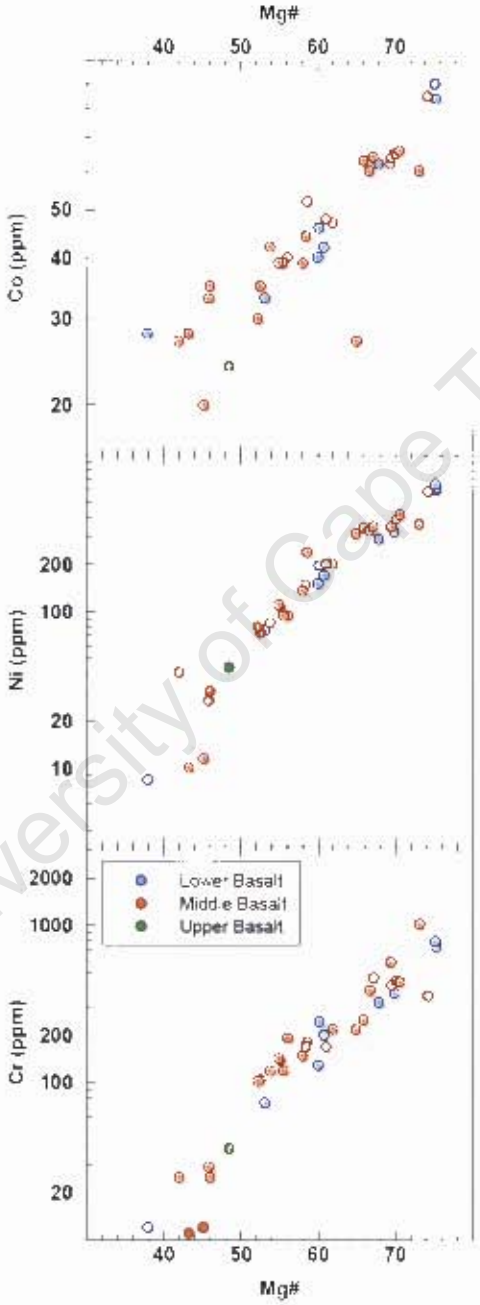

Fig 5-5: Variation of the ferro-magnesian compatible elements with Mg# for the Lower, Middle and Upper Basalts of the Gough Island lavas. Co, Ni and Cr represented on a log-normal scale.

The majority of the lavas from Gough Island exhibit sub-parallel primitive mantle normalised trace element patterns (Fig 5-6), with positive Ba and Pb anomalies as well as relative depletion in Th, U and Zr. Some samples exhibit small negative Ti anomalies.

The chondrite normalised REE patterns exhibit uniform enrichment of LREE relative to the MREE and HREE, where the LREE and HREE are 100-400x and ~10-20x chondrite, respectively. The majority of the REE patterns are sub-parallel, but a few individual samples exhibit slight variations in gradient towards the MREE and HREE which results in crossing patterns (for example ALR25G and ALR51G; Fig 5-7).

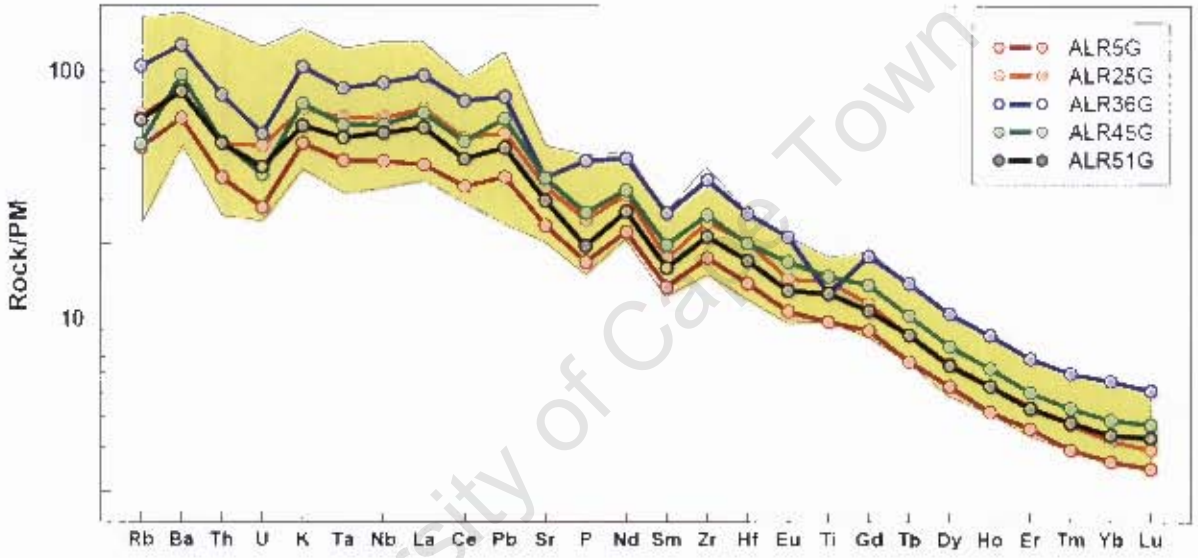

Fig 5-6: Primitive mantle normalised trace element diagram of five selected samples from the Gough Island lavas. Samples were selected so as to represent the full range of compositional variation exhibited by the sample set. Yellow field represents the full compositional range of lavas from Gough Island. Normalisation values from Sun & McDonough (1989).

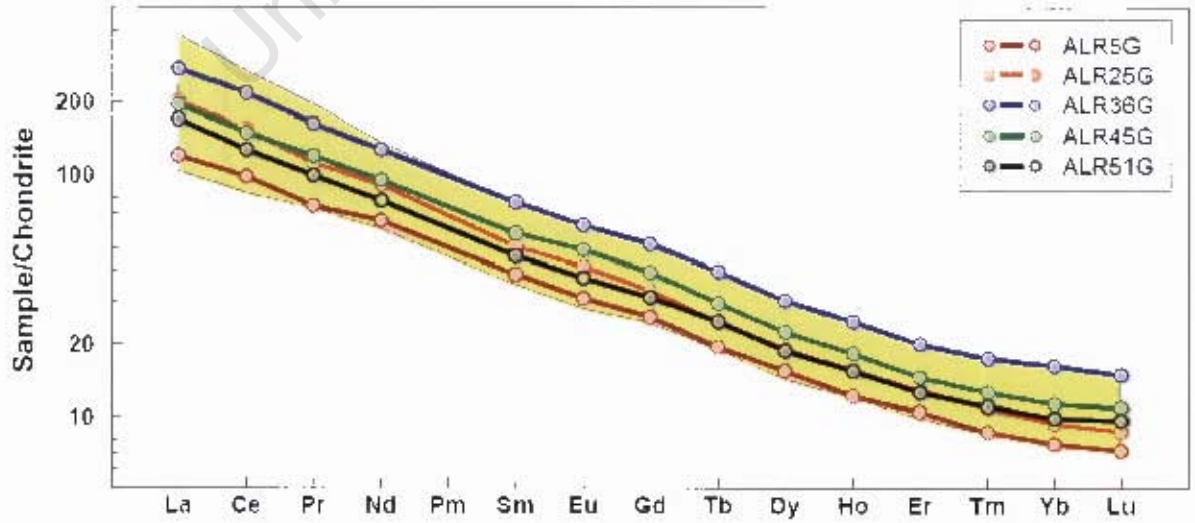

Fig 5-7: Chondrite normalised REE patterns of five selected samples from the Gough Island lavas. Samples were selected so as to represent the full range of compositional variation exhibited by the sample set. Yellow field represents the full compositional range of lavas in the sample set. Normalisation values taken from Sun & McDonough (1989).

Table 5-2: ICPMS and XRF trace element data for the Lower, Middle and Upper Basalts of the Gough Island suite of lavas.

	ALR5G	ALR7G	ALR27G	ALR30G	ALR32G	ALR33G	ALR35G	ALR36G	ALR37G	ALR38G	ALR6G	ALR8G	ALR9G
Strat.	**LB**	**LB**	**LB**	**LB**	**LB**	**LB**	**LB**	**LB**	**LB**	**LB**	**MB**	**MB**	**MB**
Sc	24.0	24.0	23.8	11.4	15.5	16.3	24.0	13.4	23.0	22.0	23.1	17.8	20.3
V*	165	157	192	122	149	166	177	171	173	158	214	214	205
Cr*	779	731	322	74.0	129	200	243	11.6	792	371	118	29.0	139
Co*	84.0	84.0	62.0	33.0	40.0	42.0	46.0	28.0	90.0	65.0	42.0	33.0	39.0
Ni*	599	613	293	76.0	151	171	198	8.50	649	324	85.0	27.0	107
Cu*	29.0	40.0	33.0	10.4	13.7	23.2	29.0	9.30	37.0	20.0	36.0	17.7	49.0
Zn*	106	101	101	109	107	110	105	121	101	94.0	115	111	105
Rb	31.0	29.0	33.2	60.1	49.2	48.6	51.0	64.4	36.0	38.0	23.4	37.4	45.0
Sr	500	489	566	645	830	797	930	723	527	706	728	725	784
Y	17.8	17.1	22.9	23.8	25.3	25.1	25.9	34.2	16.3	20.9	28.0	30.1	26.4
Zr*	197	189	268	402	342	322	339	385	169	235	278	346	297
Nb*	30.7	30.4	48.2	61.9	49.2	48.7	46.8	63.5	36.0	36.6	40.3	57.9	49.6
Ba	448	461	609	749	852	767	809	883	545	659	569	695	618
La	30.3	29.9	47.2	52.0	51.5	49.8	54.8	65.4	32.6	43.4	45.2	54.2	46.6
Ce	62.8	61.2	92.6	108	107	103	109	134	61.8	83.2	92.2	113	96.9
Pr	7.79	7.64	11.3	12.8	13.1	12.7	13.6	15.5	7.36	10.3	11.2	13.4	11.7
Nd	30.7	30.0	42.8	48.1	50.8	49.4	53.0	59.7	28.2	39.6	44.3	51.6	45.4
Sm	6.25	5.99	8.08	9.27	9.97	9.82	10.1	11.8	5.42	7.47	9.26	10.3	9.33
Eu	1.90	1.87	2.46	2.75	3.05	3.02	3.10	3.60	1.63	2.35	2.80	3.12	2.86
Gd	5.59	5.51	7.54	8.73	9.22	9.06	8.98	10.6	5.01	6.76	8.41	9.20	8.08
Tb	0.79	0.78	1.04	1.21	1.26	1.23	1.22	1.49	0.71	0.92	1.18	1.30	1.14
Dy	4.01	3.90	5.02	5.66	5.87	5.74	6.08	7.70	3.63	4.72	6.03	6.62	5.80
Ho	0.72	0.71	0.93	1.03	1.02	1.00	1.07	1.41	0.68	0.85	1.12	1.24	1.07
Er	1.72	1.68	2.18	2.43	2.26	2.24	2.46	3.31	1.61	1.97	2.64	2.91	2.52
Tm	0.23	0.23	0.29	0.33	0.30	0.29	0.33	0.45	0.22	0.26	0.36	0.40	0.35
Yb	1.39	1.39	1.76	2.00	1.74	1.70	1.93	2.76	1.33	1.59	2.14	2.44	2.11
Lu	0.20	0.20	0.25	0.29	0.24	0.23	0.27	0.38	0.19	0.23	0.31	0.35	0.30
Hf	4.29	4.20	5.84	8.15	7.29	7.15	7.27	8.20	3.68	5.17	5.84	7.17	6.06
Ta	1.77	1.81	2.64	3.37	2.62	2.52	2.75	3.47	2.13	2.14	2.34	3.17	2.79
Pb	2.63	3.27	3.71	5.26	4.48	4.90	5.12	5.56	2.54	3.42	3.60	4.54	3.93
Th	3.14	3.10	5.31	7.04	6.15	6.34	5.27	6.76	3.70	4.02	4.04	5.44	4.84
U	0.59	0.64	0.96	1.18	1.09	1.00	1.10	1.16	0.73	0.75	0.68	1.05	1.01

	ALR10G	ALR12G	ALR13G	ALR14G	ALR23G	ALR24G	ALR34G	ALR40G	ALR41G	ALR43G	ALR44G	ALR45G	ALR46G
Strat.	**MB**	**MB**	**MB**	**MB**	**MB**	**MB**	**MB**	**MB**	**MB**	**MB**	**MB**	**MB**	**MB**
Sc	24.0	23.2	18.5	20.0	16.4	24.0	11.1	26.0	32.0	18.6	23.0	20.0	24.0
V*	190	202	197	206	216	171	124	194	205	172	188	182	187
Cr*	219	192	104	119	25	354	12.4	580	1020	250	387	182	461
Co*	47.0	40.0	35.0	39.0	35.0	85.0	20.0	62.0	60.0	63.0	60.0	52.0	64.0
Ni*	202	94.0	73.0	94.0	31.0	585	11.6	350	364	346	328	239	351
Cu*	50.0	36.0	32.0	28.0	23.0	43.0	21.0	31.0	23.0	32.0	35.0	37.0	38.0
Zn*	102	107	101	103	116	109	84.0	110	92.0	120	115	117	116
Rb	37.0	14.8	41.8	36.7	43.2	45.0	104.0	30.0	24.0	27.0	35.0	32.0	34.0
Sr	777	734	771	770	688	665	1013	569	425	681	635	775	601
Y	23.4	26.6	25.6	25.4	27.4	18.3	26.4	20.9	19.4	22.0	24.4	24.7	21.8
Zr*	276	274	291	282	318	213	467	219	169	251	273	293	250
Nb*	45.2	42.4	51.3	44.2	51.2	47.3	93.1	30.4	23.5	37.3	38.0	43.1	34.1
Ba	528	562	726	726	641	625	1081	526	346	632	572	670	557
La	42.9	43.8	46.7	46.9	47.3	40.7	83.5	33.8	24.9	39.2	38.8	46.3	38.7
Ce	88.1	86.6	100	98.4	102	77.6	155	66.9	51.4	79.3	75.8	91.6	75.2
Pr	11.1	10.5	11.9	11.8	12.2	9.05	17.6	8.55	6.89	9.83	9.66	11.5	9.61
Nd	43.6	41.3	46.3	46.2	47.6	33.8	62.6	34.3	28.1	39.0	38.2	44.6	38.1
Sm	8.67	8.67	9.37	9.14	9.60	6.25	10.6	7.15	6.28	7.91	7.77	8.79	7.81
Eu	2.74	2.71	3.01	2.83	2.84	1.91	3.09	2.28	2.05	2.52	2.49	2.85	2.44
Gd	7.75	7.99	8.23	7.88	8.44	5.62	9.77	6.68	6.00	7.25	7.17	8.14	7.14
Tb	1.09	1.13	1.16	1.10	1.19	0.80	1.32	0.93	0.91	1.00	1.00	1.11	0.99
Dy	5.59	5.79	5.86	5.63	6.06	4.13	5.97	4.77	4.52	5.15	5.09	5.71	5.01
Ho	1.03	1.06	1.07	1.03	1.13	0.76	1.10	0.86	0.85	0.93	0.96	1.03	0.92
Er	2.40	2.55	2.53	2.42	2.66	1.85	2.66	1.98	1.91	2.17	2.18	2.42	2.11
Tm	0.33	0.34	0.34	0.33	0.36	0.25	0.37	0.26	0.27	0.29	0.29	0.32	0.28
Yb	2.00	2.10	2.07	2.00	2.26	1.54	2.29	1.58	1.51	1.73	1.73	1.92	1.67
Lu	0.29	0.30	0.30	0.29	0.32	0.22	0.33	0.23	0.24	0.25	0.26	0.28	0.24
Hf	5.61	5.76	6.00	5.98	6.62	4.43	8.65	4.61	3.80	5.37	5.51	6.21	5.18
Ta	2.48	2.39	2.76	2.45	2.85	2.76	5.05	1.73	1.31	2.15	2.08	2.47	1.96
Pb	3.37	3.24	3.40	3.93	3.78	3.62	8.42	2.87	1.70	3.68	3.23	4.54	3.57
Th	4.30	4.17	4.86	4.25	4.84	4.90	12.5	3.07	2.23	3.77	3.99	4.39	3.44
U	0.82	0.75	1.04	0.75	1.10	0.93	2.61	0.64	0.52	0.57	0.87	0.798	0.76

Strat. refers to the samples stratigraphic unit where LB = Lower Basalt Series; MB = Middle Basalt Series; UB = Upper Basalt Series. * indicate trace element concentrations acquired using XRFS methods (all other trace element concentrations acquired using ICP-MS methods). All trace elements expressed in ppm.

Table 5-2: continued...

Strat.	ALR47G MB	ALR48G MB	ALR49G MB	ALR50G MB	ALR51G MB	ALR52G MB	ALR53G MB	ALR54G MB	ALR55G MB	ALR56G MB	ALR64G MB	ALR63G UB
Sc	18.7	18.0	18.1	19.6	24.0	20.4	17.1	12.7	23.5	23.4	17.1	9.10
V*	162	180	141	184	177	174	195	166	171	184	160	97.0
Cr*	216	169	102	169	414	142	11.4	25.0	445	436	148	38.0
Co*	27.0	48.0	30.0	44.0	64.0	39.0	28.0	27.0	65.0	66.0	39.0	24.0
Ni*	316	203	80.0	149	351	111	10.1	41.0	390	418	136	44.0
Cu*	19.4	41.0	24.0	39.0	46.0	34.0	17.5	26.0	49.0	47.0	49.0	16.2
Zn*	113	113	98.0	104	101	105	115	103	102	101	94.0	111
Rb	38.5	28.5	71.2	42.6	40.0	65.4	71.8	51.5	37.0	33.6	49.2	78.9
Sr	593	710	743	686	630	774	717	719	558	570	687	976
Y	23.4	24.4	30.2	25.9	22.4	29.5	30.6	26.2	20.1	20.6	29.2	24.3
Zr*	272	280	386	255	240	350	384	340	232	223	309	359
Nb*	39.4	41.2	67.5	44.1	39.9	64.2	68.2	54.3	35.5	35.4	53.1	72.9
Ba	627	681	956	652	575	842	981	750	550	536	742	1205
La	42.6	43.8	65.0	45.0	40.4	64.3	63.5	53.0	36.1	37.7	61.5	74.4
Ce	87.2	91.1	129	87.8	77.9	117	123	107	75.8	75.6	110	143
Pr	10.1	10.6	15.5	10.3	9.50	14.9	14.9	12.1	8.58	8.64	12.7	15.9
Nd	40.5	42.1	59.0	39.8	36.6	55.8	57.0	46.8	33.6	33.6	48.9	59.0
Sm	8.27	8.57	11.1	8.10	7.09	10.4	11.0	9.17	6.87	6.84	9.29	10.6
Eu	2.65	2.82	3.28	2.62	2.18	3.07	3.16	3.04	2.12	2.14	2.94	3.64
Gd	7.45	7.74	10.7	7.49	6.43	9.87	10.2	8.08	6.28	6.28	8.37	8.55
Tb	1.03	1.07	1.48	1.05	0.93	1.36	1.43	1.14	0.88	0.88	1.17	1.15
Dy	5.27	5.50	7.01	5.58	4.77	6.60	6.89	5.90	4.61	4.58	6.02	5.67
Ho	0.97	1.00	1.30	1.05	0.88	1.22	1.27	1.08	0.85	0.85	1.12	0.99
Er	2.24	2.33	3.04	2.47	2.09	2.90	3.02	2.56	1.96	1.99	2.65	2.25
Tm	0.30	0.31	0.42	0.35	0.28	0.40	0.41	0.35	0.27	0.27	0.35	0.30
Yb	1.80	1.90	2.53	2.10	1.67	2.40	2.57	2.16	1.65	1.62	2.15	1.75
Lu	0.26	0.26	0.36	0.30	0.25	0.34	0.37	0.31	0.23	0.23	0.29	0.24
Hf	5.59	5.84	7.92	5.25	5.30	7.39	7.80	6.73	4.94	4.77	6.18	7.16
Ta	2.25	2.33	3.70	2.48	2.19	3.57	3.70	2.93	2.03	2.07	2.83	3.88
Pb	2.57	3.67	5.71	3.36	3.46	4.81	5.99	4.35	3.25	3.28	4.19	5.90
Th	3.72	3.98	8.00	4.61	4.31	7.30	7.84	5.52	3.79	3.62	5.29	8.44
U	0.78	0.66	1.63	0.94	0.86	1.51	1.45	0.81	0.74	0.73	1.14	1.76

Strat. refers to the samples stratigraphic unit where LB = Lower Basalt Series; MB = Middle Basalt Series; UB = Upper Basalt Series. * indicate trace element concentrations acquired using XRFS methods (all other trace element concentrations acquired using ICP-MS methods). All trace elements expressed in ppm.

5.4 The McNish Seamount

The three analysed McNish Seamount lavas (AG51-7-1, AG51-7-2 and AG51-7-3) all have near identical major and trace element geochemistry, which suggest that the three rock samples are from the same lava flow. Therefore, for the sake of clarity, in some diagrams an average value for all three samples is shown instead of the three individual samples.

The McNish Seamount lavas have similar SiO_2, K_2O and Na_2O abundances (SiO_2=44.73-46.19 wt%; K_2O=1.93-2.14 wt%; Na_2O=2.77-2.99 wt%) to the Gough Island lavas, and therefore McNish Seamount data plots within the Gough Island array on a TAS diagram. The McNish Seamount lavas also exhibit similar Al_2O_3 and CaO abundances (CaO=8.50-9.10 wt%; Al_2O_3= 12.5-12.6 wt%) as well as Mg# (62.89-64.53) as Gough Island.

The trace element abundances exhibited by the McNish Seamount lavas fall within the ranges of the trace element abundances of the Gough Island suite of lavas, but towards the differentiated end (Fig 5-3). Since the McNish Seamount exhibits similar trace element ratios to Gough Island, all of the incompatible and moderately incompatible trace element ratios for the McNish Seamount fall within the range of the respective ratios exhibited by the Gough Island suite of lavas. These trace element ratios include high Ba/Nb ratios (15.2-17.1), low Zr/Nb and La/Nb ratios (6.98-7.39 and 1.02-1.09,

respectively) as well as Zr/Hf, Yb/Nb, Nb/Ta and Ce/Pb ratios which are ~48, ~0.57, ~18 and ~22, respectively. The $(La/Sm)_N$ and $(La/Yb)_N$ ratios are ~3 and ~17, respectively (values normalised to chondritic values of Sun & McDonough (1989)).

Table 5-3: Major and high precision trace element data for three samples from the McNish Seamount. Data collected using XRFS and ICP-MS methods at the University of Cape Town (UCT). Data are unpublished but made available for use in this study.

	AG51-7-1	AG51-7-2	AG51-7-3
SiO_2	45.96	46.19	44.73
TiO_2	3.84	3.83	3.89
Al_2O_3	12.57	12.60	12.45
Fe_2O_3	1.49	1.50	1.48
FeO	9.97	9.99	9.87
MnO	0.15	0.15	0.15
MgO	9.89	9.70	10.29
CaO	9.10	8.94	8.58
Na_2O	2.99	2.95	2.77
K_2O	2.02	2.14	1.93
P_2O_5	0.89	0.83	0.65
LOI	0.41	0.38	1.20
Total	100.20	100.03	99.14
Mg#	63.39	62.89	64.53
Sc	23.0	23.0	24.0
V*	205	205	202
Cr*	267	263	296
Co*	56.0	55.0	54.0
Ni*	248	250	263
Cu*	23.0	26.0	24.0
Zn*	112	114	113
Rb	35.3	37.6	33.0
Sr	856	804	775
Y	25.9	23.7	24.1
Zr*	312	306	323
Nb*	44.7	41.5	43.9
Ba	694	709	667
La	45.4	45.1	46.5
Ce	99.0	95.3	99.9
Pr	12.6	11.7	12.4
Nd	47.8	46.8	48.5
Sm	9.67	9.64	9.98
Eu	2.94	2.82	2.96
Gd	8.71	8.36	8.83
Tb	1.23	1.15	1.20
Dy	5.89	5.77	6.06
Ho	1.09	1.00	1.06
Er	2.47	2.34	2.48
Tm	0.33	0.31	0.32
Yb	1.96	1.87	1.93
Lu	0.28	0.27	0.26
Hf	6.54	6.33	6.73
Ta	2.44	2.32	2.43
Pb	4.18	4.60	4.50
Th	4.37	4.18	4.33
U	0.79	0.85	0.84

All major element oxides given as wt%. Mg#=atomic $100Mg/(Mg/Fe^{2+})$ with $Fe_2O_3/FeO=0.20$.* indicate trace element concentrations acquired using XRFS methods (all other trace element concentrations acquired using ICP-MS methods). All trace element concentrations expressed in ppm.

Primitive mantle normalised trace element patterns (Fig 5-8) plot within the trace element compositional field for the Gough Island lavas, and are identical to the majority of Gough Island trace element patterns. Thus, the McNish seamount lavas exhibit positive Ba (~100x chondrite), Pb (~60x chondrite) and Zr (~22% chondrite) anomalies as well as negative Th (~50x chondrite) and U (~40x chondrite) anomalies. The chondrite normalised REE patterns exhibit uniform enrichment of LREE relative to the MREE and HREE, where the LREE and HREE are ~190x chondrite and ~10x chondrite, respectively. The McNish Seamount REE patterns (Fig 5-9) plot within the Gough Island REE compositional field and are identical to the Gough Island REE patterns.

The McNish Seamount and the Gough Island lavas have almost identical major and trace element geochemistry and as a result it is argued that Gough Island and the McNish Seamount are derived from similar source materials.

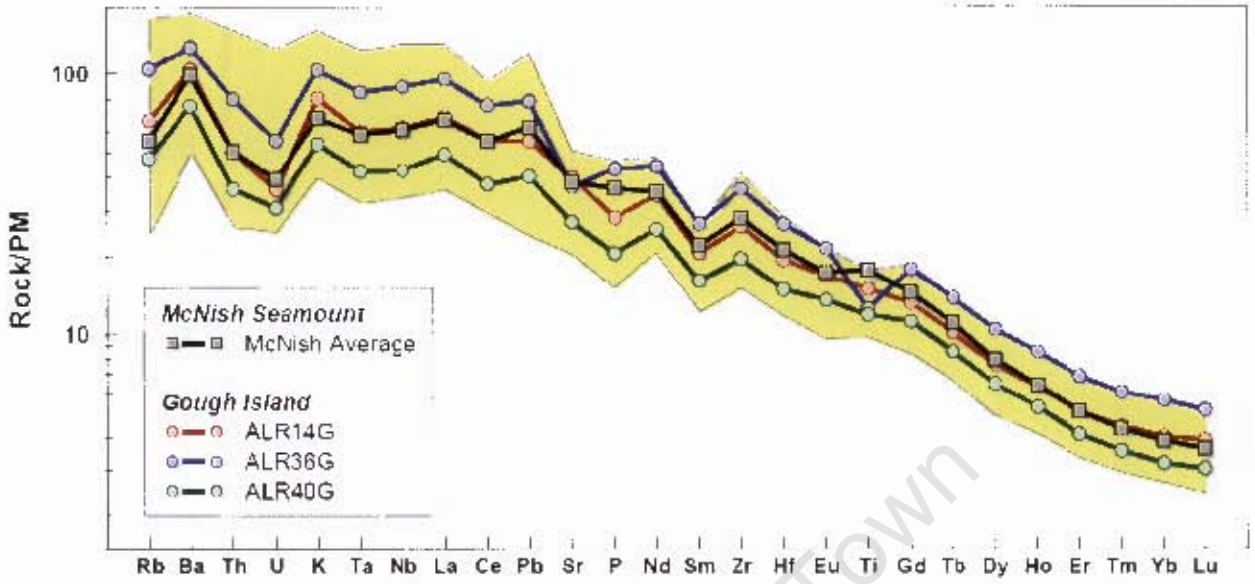

Fig 5-8: Primitive mantle normalised REE diagram for the average of the three McNish Seamount samples (AG51-7-1, AG51-7-2 and AG51-7-3). Three selected Gough Island lavas (ALR14G, ALR36G and ALR40G) are shown for comparison purposes. Gough Island REE patterns were chosen in order to illustrate both similarities and differences in abundances and REE pattern shape between the Gough Island lavas and the McNish Seamount lavas. Yellow field represents the full compositional range of the Gough Island lavas. Normalisation values taken from Sun & McDonough (1989).

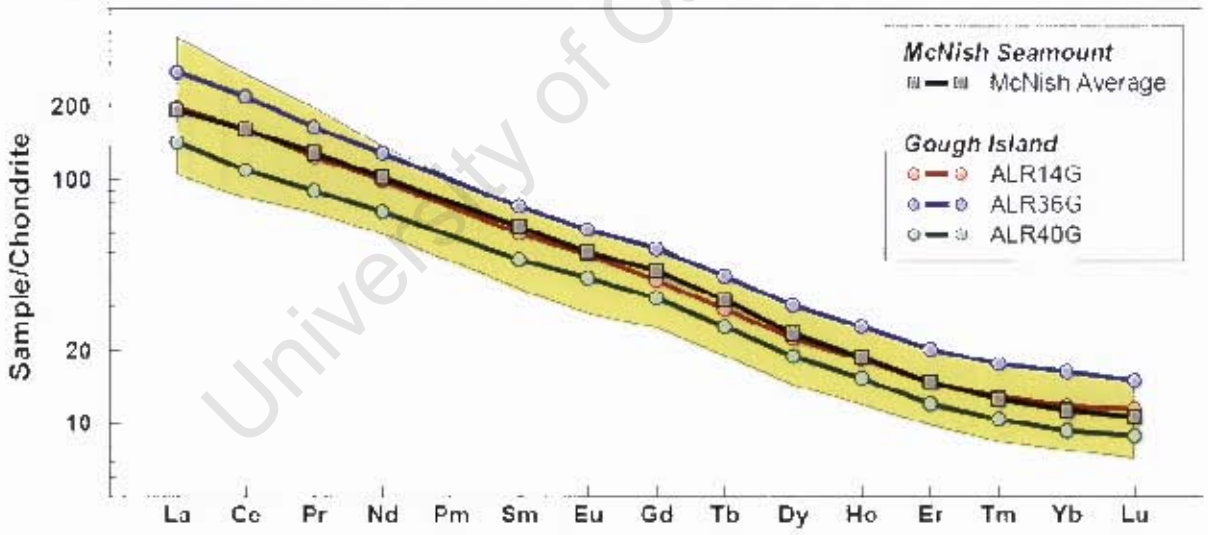

Fig 5-9: Chondrite normalised REE patterns for the average of the three McNish Seamount samples (AG51-7-1, AG51-7-2 and AG51-7-3). Three selected Gough Island lavas (ALR 14G, ALR36G and ALR40G) are shown for comparison purposes. Gough Island REE patterns were chosen in order to illustrate both similarities and differences in abundances and REE pattern shape between the Gough Island lavas and the McNish Seamount lavas. Yellow field represents the full compositional range of the Gough Island lavas. Normalisation values taken from Sun & McDonough (1989).

6 Isotope Geochemistry

6.1 Introduction

An important tool in understanding mantle geochemistry is the use of radiogenic isotope systems as geochemical tracers (Hofmann, 1997), such as the Sm-Nd, Rb-Sr, U-Pb and Lu-Hf isotope systems (e.g. Gast *et al.,* 1964 Patchett *et al.,* 1984, White & Hofmann, 1982). Parent-daughter isotope ratios are able to record information of ancient enrichment or depletion events in the mantle as radioactive parent isotopes decay into more stable daughter isotopes, thus changing the radiogenic/stable isotope ratios as a function of time (Patchett *et al.*, 1984). The behaviour of individual isotope systems differs during different Earth processes and therefore by comparing a specific isotope system to another it is possible to ascertain the nature and timing of specific processes which may have occurred (Hofmann, 1997, Patchett *et al.*, 1984). Isotopes ratios, like incompatible trace element ratios, are unaffected by melting and crystallisation processes and therefore are a direct representation of the primary magma composition and the mantle source region (Hofmann, 1997).

This chapter discusses the systematics and relevance of the Lu-Hf isotope system and reports, for the first time, newly acquired $^{176}Hf/^{177}Hf$ isotope ratios for Gough Island and the McNish Seamount which are subsequently compared to global OIB, MORB and continental $^{176}Hf/^{177}Hf$ isotope ratios.

6.2 The Lu-Hf Isotope System and its Relationship to the Sm-Nd Isotope System

Lutetium (Lu) is the heaviest REE and forms a trivalent cation with an ionic radius of 0.85Å, whereas hafnium (Hf) is a high-field strength element (HFSE) and forms a tetravalent cation with an ionic radius of 0.79Å (Whittaker & Muntus, 1970). There are numerous radiogenic isotopes of Lu, but ^{175}Lu is the most abundant (97.41%) and stable isotope, whereas Hf has five stable isotopes (^{176}Hf to ^{180}Hf) with the most abundant being ^{180}Hf (35.1%) followed by ^{178}Hf (27.297%). ^{176}Lu (2.59%) forms ^{176}Hf through beta decay with a half life of 35.9Ga (Sguigna *et al.*, 1982) .

In both the Lu-Hf and Sm-Nd isotope systems, the parent elements (Lu and Sm) are less incompatible than the daughter elements and both are rare-earth elements (Blichert-Toft, 2001, Blichert-Toft *et al.*, 1997). The similarity between the parent elements of these two systems results in near-identical behaviour in geochemical systems and together with time-integrated decay, results in a well constrained positive correlation in Hf-Nd isotope space (Blichert-Toft, 2001, Patchett & Tatsumoto, 1980, Salters & Hart, 1991, Vervoort *et al.*, 1999).

Even though the parent elements are similar in these two isotope systems, the daughter elements are not. In the Sm-Nd isotope system the daughter element (Nd) is a REE whereas in the Lu-Hf isotope system the daughter element (Hf) is a HFSE (Blichert-Toft *et al.*, 1997) and Nd and Hf occur in tri- and tetravalent states, respectively. Differences in ionic radii and valence states between Lu and Hf results in two very important decoupling mechanisms, which not only decouples Lu from Hf, but also the Lu-Hf isotope system from the Sm-Nd isotope system.

Hf is more incompatible than Lu during mantle partial melting processes (mineral/melt partition coefficients for Hf in garnet, clinopyroxene, orthopyroxene and olivine are smaller than for Lu in the same minerals; (Blichert-Toft *et al.*, 1997, Donnelly *et al.*, 2004, Hauri *et al.*, 1994)). This results in the extraction of Hf in preference to Lu from the upper mantle to newly formed crust, and the present day crust is thus enriched in Hf relative to Lu, leaving the mantle depleted in Hf relative to Lu (Blichert-Toft *et al.*, 1997). Since Hf is able to easily substitute for Zr in the mineral zircon (both ions are tetravalent and have similar ionic radii (Blichert-Toft *et al.*, 1997, Patchett *et al.*, 1984)) and as zircons are very resistant to both chemical and mechanical weathering, detrital zircons are naturally sorted in the oceans into larger-grained sediments which include sandstones and turbidites along and adjacent to the world's continental shelves (Patchett *et al.*, 1984). This natural sorting process of zircons in oceanic sediments acts as a tracer during sediment recycling through the mantle, as zircon-rich, terrigenous sediments have lower $^{176}Lu/^{177}Hf$ isotope ratios (0.002-0.013) and deep-sea, zircon-poor, pelagic sediments have higher $^{176}Lu/^{177}Hf$ isotope ratios (0.035-0.09) (Patchett *et al.*, 1984), which, with time-integrated decay develop lower and higher $^{176}Hf/^{177}Hf$ isotope ratios for terrigenous and pelagic sediments, respectively. Subduction and binary mixing of recycled sediment with ambient mantle results in a mixture enriched in Hf relative to Lu. Therefore, the lower relative concentration of Lu in the resulting mixed mantle results in lower concentrations of ^{176}Hf over time and therefore lower $^{176}Hf/^{177}Hf$ isotope ratios (^{177}Hf is stable and therefore is not affected by decay processes). This is known as the Zircon Effect.

Hf is more incompatible during partial melting events in the presence of garnet than Lu, since the mineral/melt partition coefficient for Hf in garnet is smaller than Lu ($^{Hf}D_{Garnet} = 0.115$ and $^{Lu}D_{Garnet} = 4.5$ (McKenzie & O'Nions, 1991)); Lu^{3+} is able to easily substitute Al^{3+} in garnet as a result of similar ionic radii and valency states (Salters & Hart, 1989). This results in partial melts derived from a garnet bearing source having low Lu/Hf ratios, which with time-integrated decay results in low $^{176}Hf/^{177}Hf$ isotope ratios (Dickin, 1995, Patchett & Tatsumoto, 1980). The fractionation of Lu/Hf ratios is larger than Sm/Nd (Patchett & Tatsumoto, 1980), as the difference between the Lu-Hf mineral/melt partition coefficients is larger than for Sm-Nd ($^{Sm}D_{Garnet} = 0.17$ (McKenzie & O'Nions, 1991) and $^{Nd}D_{Garnet} = 0.0052$ (Johnson, 1994)), and results in the development of a larger variation in $^{176}Hf/^{177}Hf$ than $^{143}Nd/^{144}Nd$ isotope ratios over time (Dickin, 1995, Patchett & Tatsumoto, 1980, Salters & Hart, 1989). This is known as the garnet effect and results in mantle derived partial melts or

a mantle source region produced by the interaction of partial melts with ambient mantle (where the partial melts are generated in the presence of garnet) forming steep arrays in Hf-Nd isotope space (over time) that plot below the Hf-Nd mantle array line of Vervoort *et al.*, (1999) (Patchett & Tatsumoto, 1980). However, the fractionation of Lu/Hf and Sm/Nd is not exhibited by partial melts derived from a garnet-poor source (within the spinel stability field). This results in the Hf and Nd isotope systems behaving similarly over time and forming arrays, for partial melts or a mantle source region produced by the interaction of partial melts with ambient mantle, that plot along the Hf-Nd mantle array line (Dickin, 1995, Patchett & Tatsumoto, 1980).

6.3 Isotope Geochemistry of the Gough Island and McNish Seamount Lavas

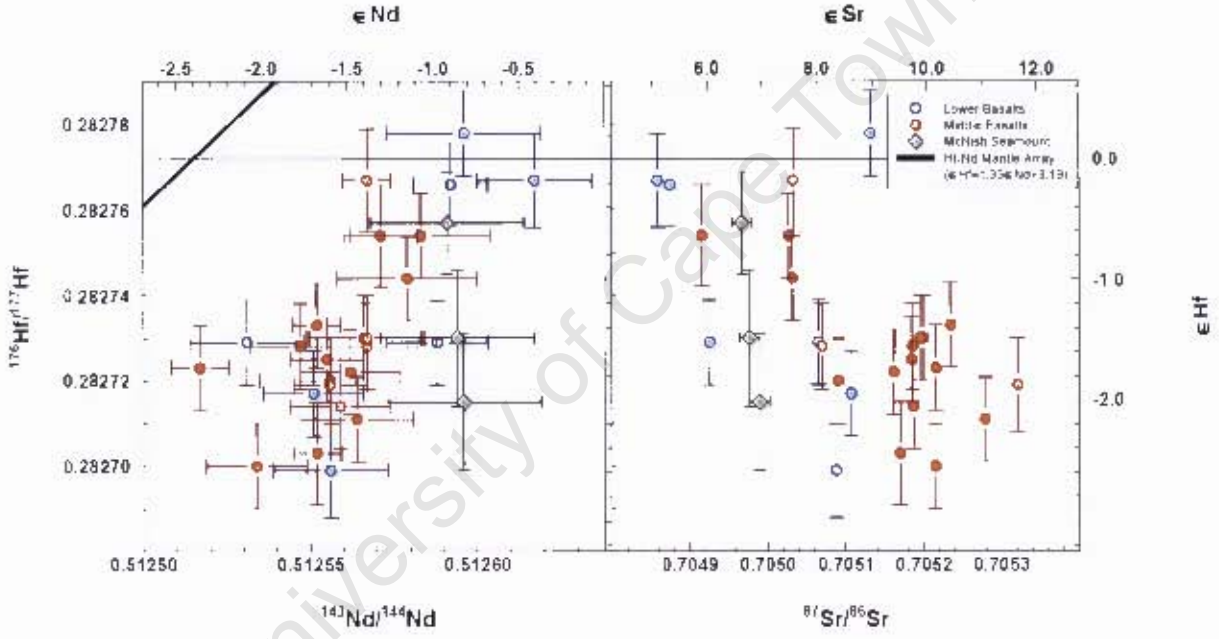

Fig 6-1: Gough Island Lower and Middle Basalts as well as the McNish Seamount lavas represented in Hf-Nd and Hf-Sr isotope space. Error bars represent a 2σ S.E. The Hf-Nd mantle array line (εHf=1.33εNd+3.19; solid black line) from Vervoort *et al.*, (1999). εHf calculated using $(^{176}Hf/^{177}Hf)_{CHUR}$ of 0.282772 (at t=0Ga), εNd calculated using $(^{143}Nd/^{144}Nd)_{CHUR}$ of 0.512638 (at t=0Ga) (Blichert-Toft & Albarède, 1997) and εSr calculated using $(^{87}Sr/^{86}Sr)_{CHUR}$ of 0.7045 (at t=0Ga). Nd and Sr isotope data for the Gough Island lavas and the McNish Seamount lavas from Class & le Roex (2008) and Class & le Roex (unpublished data), respectively.

$^{176}Hf/^{177}Hf$ isotope ratios for the Gough Island lavas are reported in Table 6-1 and range from 0.282699±12 to 0.282778±10 (εHf[3]=-2.6 to 0.2; see Fig 6-1; errors are 2σ ($x10^{-6}$) S.E.), where the Lower and Middle Basalt $^{176}Hf/^{177}Hf$ isotope ratios range from 0.282699±12 to 0.282778±10 and 0.282703±12 to 0.282767±12, respectively (the single Upper Basalt sample was not analysed for $^{176}Hf/^{177}Hf$). The $^{143}Nd/^{144}Nd$ and $^{87}Sr/^{86}Sr$ isotope ratios for the Gough Island lavas ranges from 0.512517±9 to 0.512596±23 and 0.704859±12 to 0.705321+12, respectively (Class & le Roex, 2008).

[3] $\varepsilon Hf = \left[\frac{(^{176}Hf/^{177}Hf)_{sample}}{(^{176}Hf/^{177}Hf)_{CHUR}} - 1\right] \times 10^4$ where $(^{176}Hf/^{177}Hf)_{CHUR} = 0.282772$ (at t=0Ga) (Blichert-Toft & Albarède, 1997).

The $^{176}Hf/^{177}Hf$ isotope ratios for the McNish Seamount lavas, range from 0.282715±16 to 0.282757–12, respectively, whereas the $^{143}Nd/^{144}Nd$ and $^{87}Sr/^{86}Sr$ isotope ratios range from 0.512591±45 to 0.512596–45 and 0.704977±13 to 0.704992±13, respectively (Class & le Roex, unpublished data).

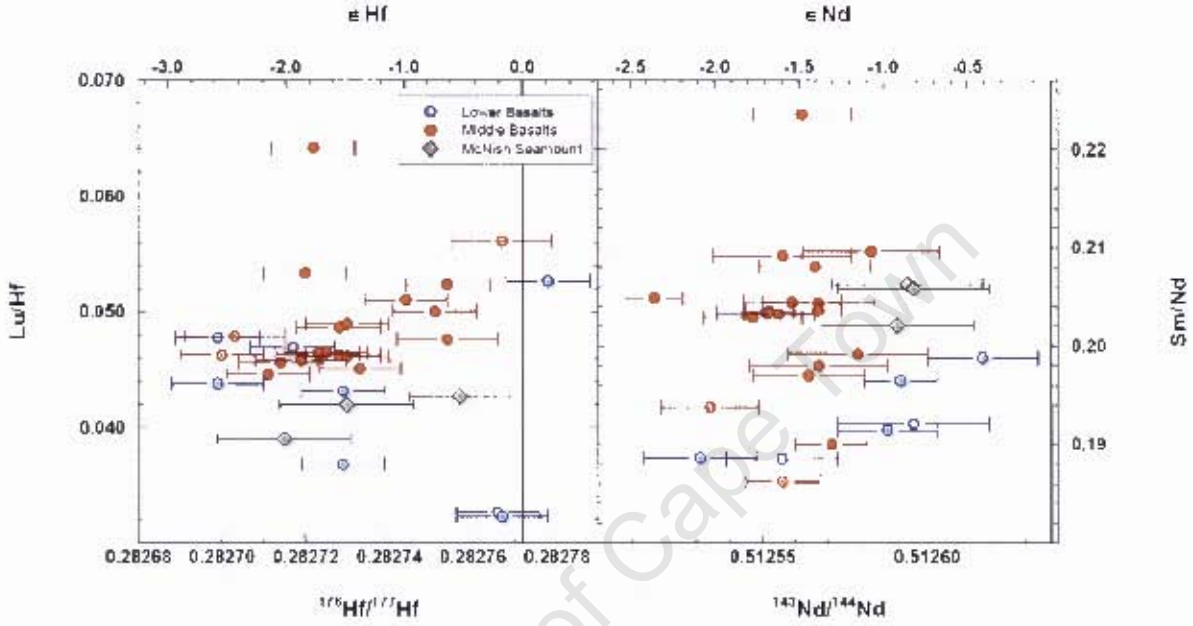

Fig 6-2: Lu/Hf vs. $^{176}Hf/^{177}Hf$ and Sm/Nd vs. $^{143}Nd/^{144}Nd$ for the Gough Island Lower and Middle Basalts as well the McNish Seamount lavas. Error bars represent a 2σ S.E. εHf calculated using $(^{176}Hf/^{177}Hf)_{CHUR}$ of 0.282772 (at t=0Ga) and εNd calculated using $(^{143}Nd/^{144}Nd)_{CHUR}$ of 0.512638 (at t=0Ga) (Blichert-Toft & Albarède, 1997). Nd isotope data for the Gough Island lavas and the McNish Seamount lavas from (Class & le Roex, 2008) and Class & le Roex (unpublished data), respectively.

The Gough Island Lower and Middle Basalts as well as the McNish lavas form scattered, sub-parallel arrays within the enriched quadrants (near primitive mantle compositions) in Hf-Nd and Hf-Sr isotope space (Fig 6-1). The Lower and Middle Basalt as well as the McNish Seamount arrays are superimposed in Hf-Nd and Hf-Sr isotope space and therefore all of these lavas are isotopically similar. However, despite the McNish lavas appearing to be from the same lava flow (Section 5.4), these lavas exhibit different $^{176}Hf/^{177}Hf$ isotope ratios, which indicate inter-sample heterogeneity. These arrays plot below the Hf-Nd mantle array line (εHf=1.33εNd−3.19; (Vervoort *et al.*, 1999)) with $\Delta\varepsilon Hf$[4] (measurement indicating the difference between a calculated εHf value from the Hf-Nd mantle array line and a measured εHf value (Johnson & Beard, 1993)) ranging from 1.5 to 3.4 for Gough Island and 2.5 to 4.1 for the McNish Seamount, which indicates decoupling of the Hf and Nd isotope systems (Janney & le Roex, 2005, Johnson & Beard, 1993) as a result of the Zircon or Garnet Effects (Section 6.2).

[4] $\Delta\varepsilon Hf = \varepsilon Hf - (1.33\varepsilon Nd + 3.19)$(Johnson & Beard, 1993).

Table 6-1: Hf, Nd and Sr isotope ratios as well as Lu and Hf trace element concentrations of the Gough Island and the McNish lavas.

Sample	Lu	Hf	$^{176}Hf/^{177}Hf$	2σ (x10^{-6}) S.E.[b]	εHf[c]	$^{143}Nd/^{144}Nd$[a]	$^{87}Sr/^{86}Sr$[a]
Gough Island							
ALR5G	0.20	4.29	0.282715	10	-2.02	0.512551	0.705107
Repeat	-	-	0.282718	10	-1.90	-	
ALR6G	0.31	5.84	0.282720	10	-1.83	0.512556	0.705091
ALR7G	0.20	4.03	0.282699	10	-2.58	-	-
ALR10G	0.29	5.61	0.282744	10	-0.99	0.512579	0.705032
ALR12G	0.30	5.76	0.282754	10	-0.62	0.512583	0.705027
ALR14G	0.29	5.98	0.282728	10	-1.56	0.512567	0.705070
ALR24G	0.22	4.43	0.282751	10	-0.75	-	
ALR27G	0.25	5.84	0.282729	10	1.53	0.512531	0.705065
ALR32G	0.24	7.39	0.282766	10	0.20	0.512592	0.704875
ALR33G	0.23	7.25	0.282771	12	-0.05	0.512617	0.704869
Repeat		-	0.282763	10	-0.32	-	-
ALR35G	0.27	7.27	0.282729	10	-1.53	0.512588	0.704926
ALR37G	0.19	3.68	0.282778	10	0.22	0.512596	0.705132
ALR38G	0.23	5.17	0.282695	12	2.72	0.512556	0.705088
Repeat	-		0.282702	10	-2.50	-	-
Duplicate			0.282700	10	-2.54	-	-
ALR40G	0.23	4.61	0.282730	10	-1.49	0.512586	0.705200
ALR41G	0.24	3.80	0.282722	10	-1.76	0.512562	0.705169
ALR43G	0.25	5.38	0.282726	10	-1.61	0.512547	0.705186
Repeat	-	-	0.282730	10	-1.47	-	
ALR44G	0.26	5.51	0.282728	10	-1.55	0.512555	0.705185
Repeat	-	-	0.282722	10	-1.78		
ALR45G	0.28	6.21	0.282711	10	-2.16	0.512564	0.705279
ALR46G	0.24	5.28	0.282723	10	-1.72	0.512517	0.705216
ALR47G	0.26	5.59	0.282730	10	-1.50	0.512567	0.705196
ALR48G	0.26	5.84	0.282733	10	-1.39	0.512552	0.705235
ALR50G	0.30	5.25	0.282767	12	-0.19	0.512567	0.705033
ALR51G	0.25	5.30	0.282700	10	-2.55	0.512534	0.705215
ALR52G	0.34	7.39	0.282721	12	1.80	0.512556	0.705321
Repeat	-	-	0.282725	10	1.67		
Duplicate	-	-	0.282711	10	2.15		-
ALR55G	0.225	4.94	0.282714	10	2.04	0.512559	0.705187
ALR56G	0.328	4.77	0.282703	12	-2.43	0.512552	0.705170
ALR64G	0.294	6.18	0.282754	12	-0.65	0.512571	0.704916
McNish Seamount							
AG51-7-1	0.28	6.54	0.282749	16	-0.80	0.512591	0.704967
Repeat	-	-	0.282764	7	-0.27		
AG51-7-2	0.27	6.33	0.282733	16	1.75	0.512594	0.70498
Repeat			0.282737	15	1.21	-	-
AG51-7-3	0.26	6.73	0.282715	16	-2.03	0.512596	0.70499

[a] $^{143}Nd/^{144}Nd$, $^{87}Sr/^{86}Sr$ data for Gough Island and the McNish Seamount from (Class & le Roex, 2008) and (Class & le Roex, unpublished data), respectively. [b] Reported errors are 2σ standard deviations from repeat analyses of the standard JMC-475. [c] εHf ratios normalised to ($^{176}Hf/^{177}Hf)_{CHUR}$=0.282772 (at t=0Ga) (Blichert-Toft & Albarède, 1997). Repeat = repeat analysis of sample. Duplicate = analysis of a newly prepared sample. $^{176}Hf/^{177}Hf$ isotope data acquired as outlined in Chapter 3 on Analytical Geochemistry.

6.4 Gough Island in a Regional and Global Context

The Tristan da Cunha lavas range in εHf and εNd from 0.28 to 2.15 (Class *et al.*, unpublished data) and -2.50 to -0.94 (Class & le Roex, unpublished data), respectively, and form an array in Hf-Nd isotope space which straddles the Hf-Nd mantle array line (Vervoort *et al.*, 1999), but plots towards higher $^{176}Hf/^{177}Hf$ isotope ratios for a given $^{143}Nd/^{144}Nd$ isotope ratio in comparison to the Gough Island array (Fig 6-3). The Inaccessible Island lavas extend to higher $^{176}Hf/^{177}Hf$ (εHf = -0.43 to 5.76 Class *et al.*, (unpublished data)) and $^{143}Nd/^{144}Nd$ (εNd = -1.91 to 1.59 Class & le Roex (unpublished data)) isotope ratios in comparison to the Gough Island lavas and plots along the Hf-Nd mantle array

line, stretching from the field of Tristan da Cunha towards more depleted Hf and Nd isotope compositions. Unlike Gough Island and the McNish Seamount, the Tristan da Cunha and Inaccessible Island lavas plot along the Hf-Nd mantle array line and therefore the Hf and Nd isotope systems are not decoupled.

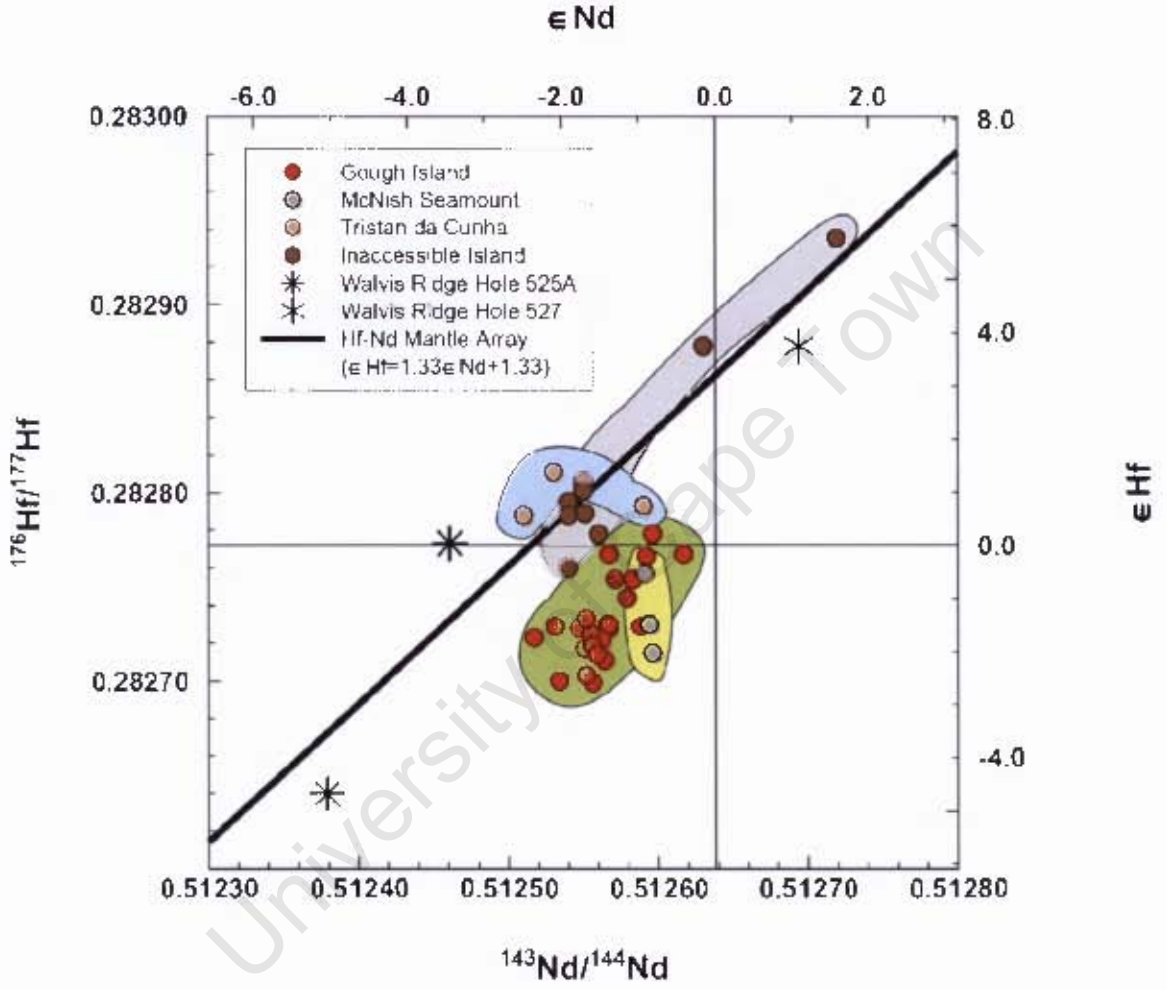

Fig 6-3: Gough Island, McNish Seamount, Tristan da Cunha and Inaccessible Island in Hf-Nd isotope space. The Hf-Nd mantle array line (εHf = 1.33εNd + 3.19; solid black line) from Vervoort *et al.*, (1999). εHf calculated using $(^{176}Hf/^{177}Hf)_{CHUR}$ of 0.282772 (at t = 0Ga) and εNd calculated using $(^{143}Nd/^{144}Nd)_{CHUR}$ of 0.512638 (Blichert-Toft & Albarède, 1997). $^{143}Nd/^{144}Nd$ values for Gough Island from Class & le Roex (2008), $^{176}Hf/^{177}Hf$ for Tristan da Cunha, Inaccessible Island from Class *et al.*, (unpublished data) $^{143}Nd/^{144}Nd$ for Tristan da Cunha, Inaccessible Island and the McNish Seamount from Class & le Roex (unpublished data), Walvis Ridge $^{143}Nd/^{144}Nd$ from Richardson *et al.*, (1984) and $^{176}Hf/^{177}Hf$ from Salters & Hart (1991). Errors are not shown for the sake of clarity, however errors for Gough Island and McNish Seamount are shown in Fig 6-1.

The Gough Island and the McNish Seamount lavas plots at the enriched end of the global OIB arrays (Fig 6-4 and Fig 6-5), within the more depleted end of the continental array (Vervoort *et al.*, 1999), in Hf-Nd-Sr isotope space and therefore are some of the most isotopically enriched oceanic lavas in the world, in terms of Hf, Nd and Sr isotopes. Other islands which exhibit enriched Hf isotope ratios (although not as enriched as Gough Island) are St Helena, Kerguelen (PETDB

(http://www.petdb.org) and precompiled files from the GEOROC (http://georoc.mpch-mainz.gwdg.de/georoc/) databases) and Bouvet Island lavas (Janney & le Roex, 2005).

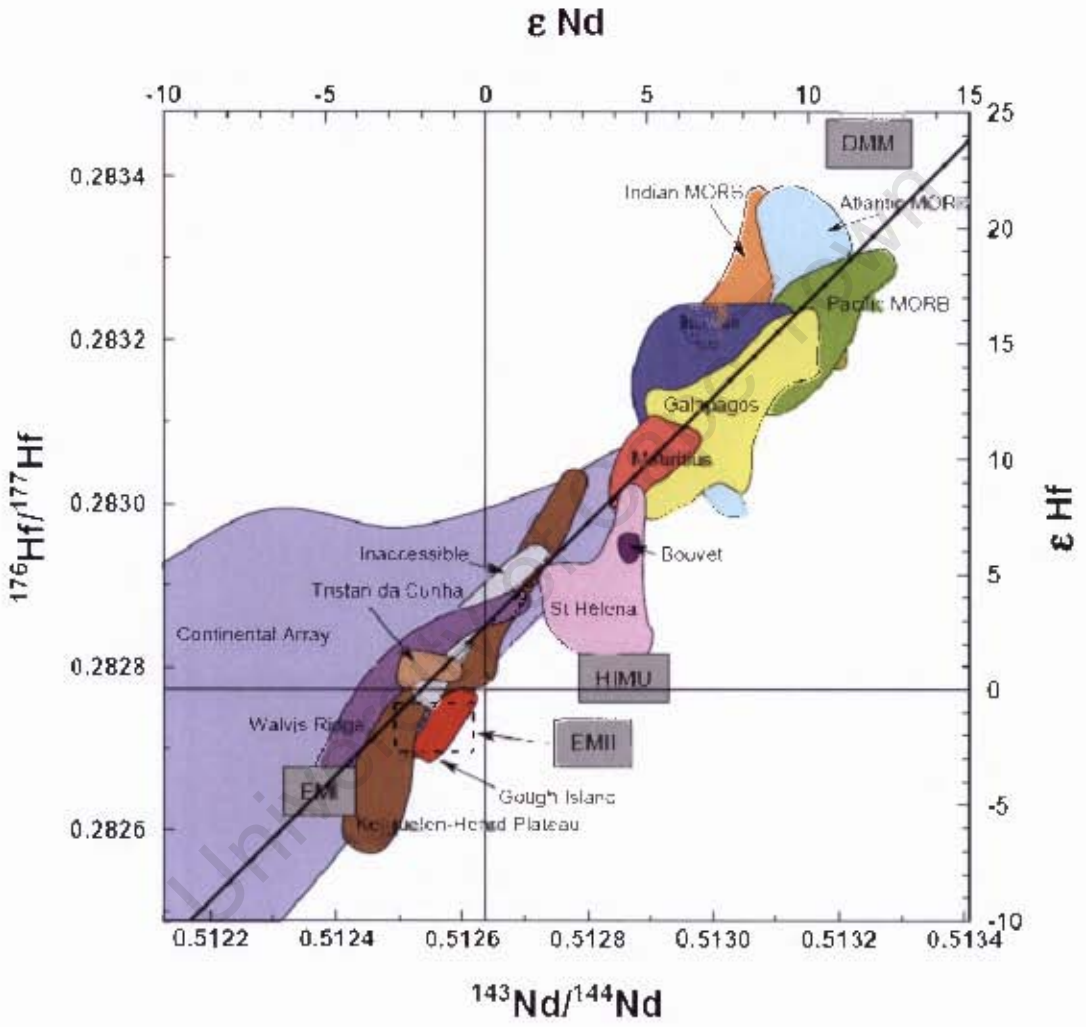

Fig 6-4: Global MORB and OIB compositions represented in Hf-Nd isotope space. The Hf-Nd mantle array line ($\varepsilon Hf=1.33\varepsilon Nd-3.19$; solid black line) from Vervoort *et al.*, (1999) and mantle end-member compositions from Salters & White (1998). εHf calculated using $(^{176}Hf/^{177}Hf)_{CHUR}$ of 0.282772 (at t=0Ga) and εNd calculated using $(^{143}Nd/^{144}Nd)_{CHUR}$ of 0.512638 (at t=0Ga) (Blichert-Toft & Albarède, 1997). $^{143}Nd/^{144}Nd$ data for Gough Island from Class & le Roex (2008); $^{176}Hf/^{177}Hf$ and $^{143}Nd/^{144}Nd$ isotope data for Tristan da Cunha and Inaccessible Island from Class *et al.*, (unpublished data). $^{143}Nd/^{144}Nd$ data for Walvis Ridge from Richardson *et al.*, (1982) and $^{176}Hf/^{177}Hf$ from Salters & Hart (1991); Bouvet Island from Janney & le Roex (2005); Continental Array from Vervoort *et al.*, (1999) and all other OIB and MORB isotope data from the PETDB (http://www.petdb.org) and precompiled files of the GEOROC (http://georoc.mpch-mainz.gwdg.de/georoc/) databases.

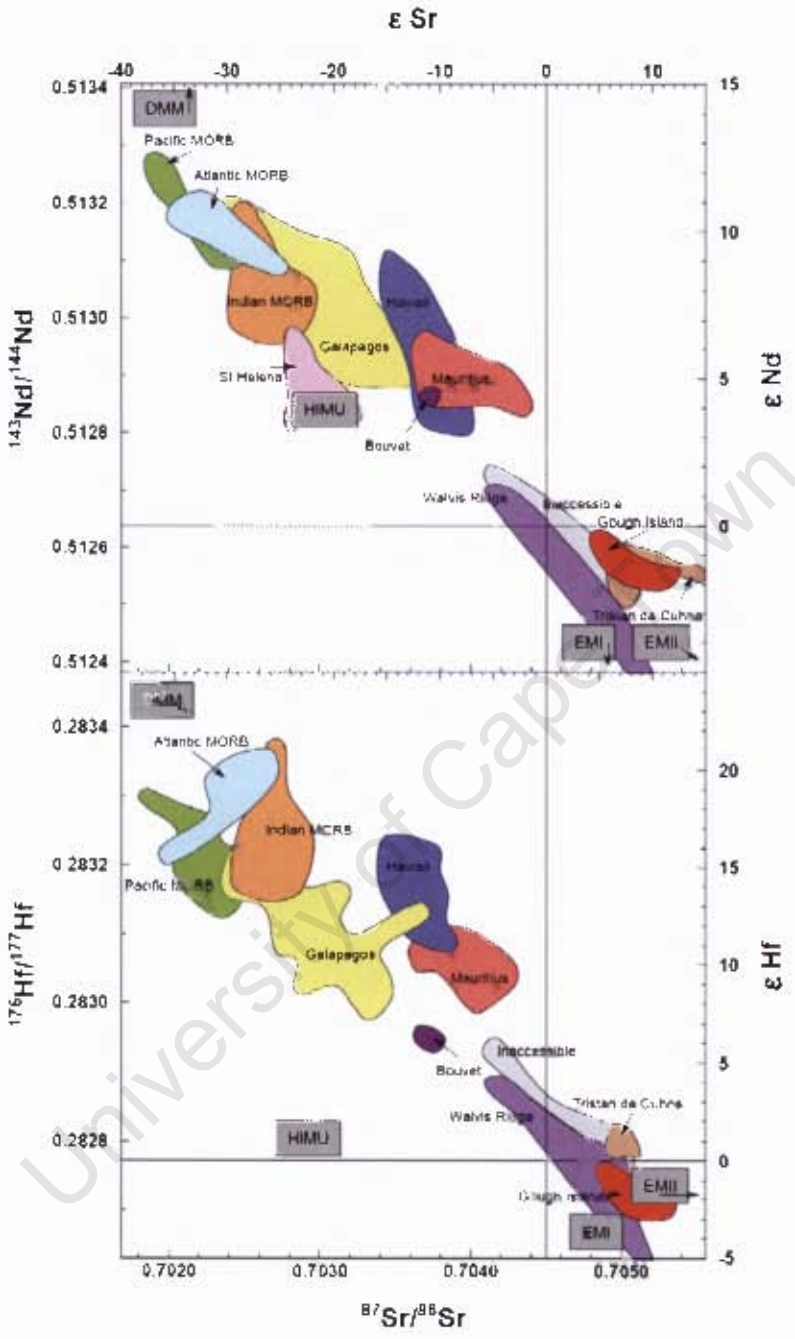

Fig 6-5: Global MORB and OIB compositions represented in Nd-Sr (top) and Hf-Sr (bottom) isotope space. Mantle end-member compositions from Salters & White (1998). εHf calculated using $(^{176}Hf/^{177}Hf)_{CHUR}$ of 0.282772 (at t 0Ga), εNd calculated using $(^{143}Nd/^{144}Nd)_{CHUR}$ of 0.512638 (at t=0Ga) (Blichert-Toft & Albarède, 1997) and εSr calculated using $(^{87}Sr/^{86}Sr)_{CHUR}$ (at t=0Ga) of 0.7045. $^{87}Sr/^{86}Sr$ and $^{143}Nd/^{144}Nd$ isotope data for Gough Island from Class & le Roex (2008), $^{176}Hf/^{177}Hf$ isotope data for Inaccessible Island and Tristan da Cunha from Class *et al.*, (unpublished data) and $^{143}Nd/^{144}Nd$ isotope data for Inaccessible Island and Tristan da Cunha from Class & le Roex (unpublished data), respectively, $^{143}Nd/^{144}Nd$ and $^{87}Sr/^{86}Sr$ data for Walvis Ridge from Richardson *et al.*, (1982) and $^{176}Hf/^{177}Hf$ from Salters & Hart (1991); Bouvet Island from Janney & le Roex (2005); Continental Array from Vervoort *et al.*, (1999) and all other OIB and MORB isotope data from the PETDB (http://www.petdb.org) and precompiled files of the GEOROC (http://georoc.mpch-mainz.gwdg.de/georoc/) databases.

6.5 Hf Isotope and Trace Element Variation

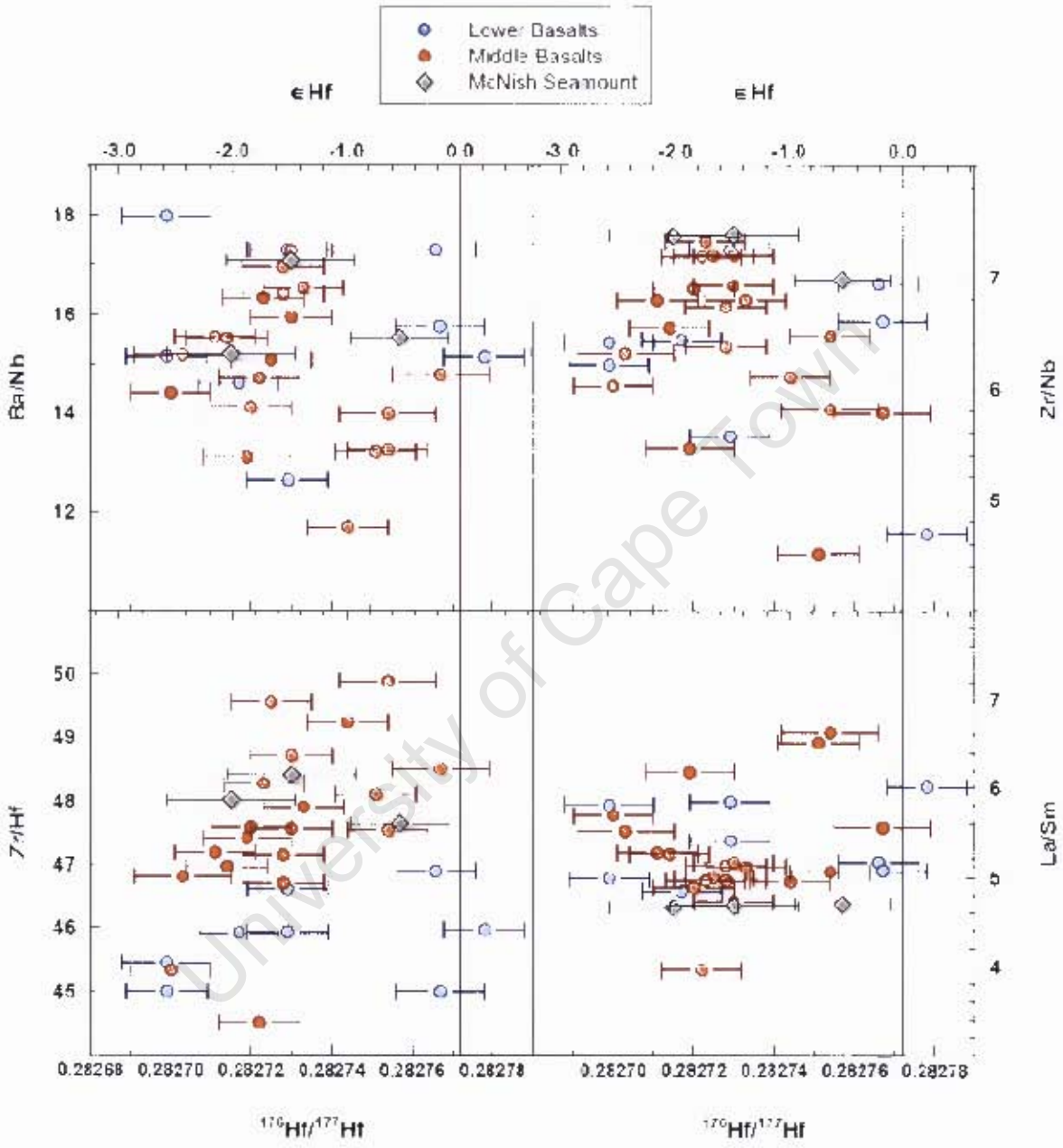

Fig 6-6: Selected trace element ratios vs. $^{176}Hf/^{177}Hf$ isotope ratios for the Lower and Middle Basalts as well as the McNish Seamount lavas. $^{176}Hf/^{177}Hf$ error bars represent 2σ S.E.

The Gough Island lavas exhibit high Ba/Nb ratios (Ba/Nb = 11.6-18.0) and low Zr/Nb and La/Sm ratios (Zr/Nb = 4.51-7.32; La/Sm = 3.96-7.87). The Lower and Middle Basalts exhibit similar Ba/Nb, Zr/Nb and La/Sm ratios (Fig 6-6) and therefore these arrays are superimposed, without any obvious correlations, in a plot of these incompatible trace element ratios vs. $^{176}Hf/^{177}Hf$. The same is true for the parent/daughter ratios vs. isotope ratios (Fig 6-2). However, the Lower Basalts have lower Zr/Hf

ratios than the Middle Basalts (Lower Basalts: Zr/Hf = 45.0-49.4; Middle Basalts: Zr/Hf = 44.5-54.0). The difference in the Zr/Hf ratios between the Lower and Middle Basalts suggests that the Gough Island mantle source region is heterogeneous, where the Lower Basalts are generated by a source that has similar Hf isotope ratios to the Middle Basalt mantle source region, but has different Zr/Hf trace element ratios. The McNish Seamount lavas exhibit similar Ba/Nb, Zr/Nb, La/Sm and Zr/Hf ratios as the Gough Island basalts (Ba/Nb = 15.2-17.1; Zr/Nb = 6.98-7.38; La/Sm = 4.66-4.69; Zr/Hf = 47.6-48.4). The McNish Seamount lavas plot within the Middle Basalt array on a plot of Zr/Hf vs. $^{176}Hf/^{177}Hf$, which suggests in this respect, that the McNish Seamount mantle source region is similar in composition to the Middle Basalt mantle source region.

7 Petrogenesis of the Gough Island Suite of Lavas

7.1 Introduction

One of the fundamental problems in studying the mantle and mantle dynamics is the inability to sample fresh mantle rocks directly from the mantle and therefore geochemists must rely on a range of different rocks which can act as a window into the mantle (Hofmann, 1997). Ocean island basalts (OIB) serve this objective particularly well as they are mantle derived lavas that do not pass through continental crust (Green & Ringwood, 1967, Yoder, 1976) and therefore have been and are still extensively studied. However, OIB are still subjected to processes which can alter their original, primary composition and therefore corrections need to be made to correct for any chemical overprints which can occur as magma migrates from the source region to the surface of the Earth. Such processes include mixing of magmas of differing compositions (Andres *et al.*, 2002, Blichert-Toft & White, 2001, Davis *et al.*, 2003, Janney & le Roex, 2005, Langmuir *et al.*, 1978, le Roux *et al.*, 2002), crystal fractionation and accumulation effects (Frey & Rhodes, 1993, Gibson *et al.*, 2005, Klügel *et al.*, 2005, le Roex, 1985, le Roex & Erlank, 1982, Zielinski & Frey, 1970) and contamination by country rocks or near surface sediments as well as hydrothermal processes at shallow crustal depths (Davis *et al.*, 2003, Hansteen & Troll, 2003). It is important that these chemical overprints are understood and corrected for in order to ascertain the nature and composition of the mantle source region.

In this chapter, ten primary magma compositions are calculated from measured major and trace element data of Gough Island lavas, which are subsequently used to gain an understanding of the nature and composition of the Gough Island mantle source region through constrained forward modelling methods.

7.2 Partial Melting Models

Different styles of partial melting are postulated to exist, with the two end-members being equilibrium (batch) melting and fractional melting. In equilibrium or batch melting, melt produced remains in contact with the residual source and therefore is able to equilibrate with the residual source until a threshold is reached at which time all the melt is removed (Shaw, 1970). In contrast, fractional melting involves the production and immediate removal of infitessimally small amounts of melt, and therefore the bulk source composition continually changes (Gast, 1968). Intermediate melting styles include aggregated fractional melting, which differs from fractional melting by allowing removed melts to aggregate prior to eruption, and continuous melting, where a large portion of the melt produced is removed and the remainder of the melt is allowed to equilibrate with new melts produced from the residual source prior to removal (Feigenson *et al.*, 1996).

Equilibrium (batch) melting is preferred in this study as this melting style produces realistic results in all the models and is simple to model. Pure fractional melting produces unrealistic results and the two intermediate styles of melting, continuous melting and aggregated fractional melting produce reasonable results in all the models but are no better than equilibrium melting. Therefore all modelling in the remainder of this chapter is based on equilibrium melting, which is defined by the following equation:

$$\frac{C_l}{C_0} = \frac{1}{D_0 + F(1-P)}$$

Equation 7.1: Trace element behaviour during equilibrium (batch) melting (Shaw, 1970).

Where:

C_l = concentration of trace element in melt

C_0 = concentration of trace element in source prior to melting

D_0 = bulk partition coefficient of trace element, calculated from phase proportions in source prior to melting by the equation: $D_0 = \sum X_0 D$

F = degree of melting ($0 \leq F \leq 1$)

P = bulk partition coefficient of trace element, calculated from the phase proportions entering melt by the equation: $P = \sum pD$

X_0 = phase proportions in source material (Start Mode)

p = proportions of phase entering melt (Melt Mode)

7.3 Determination of Primary Magma Compositions

The magma produced from the melting of a source region that has not undergone any subsequent form of differentiation or contamination processes is known as a primary magma. The majority of basalts are argued to have undergone crystal fractionation processes after melting and prior to eruption, and therefore cannot be classified as primary magmas (O'Hara, 1965). Crystal fractionation processes results in the removal of mineral phases from magma whereas crystal settling results from the addition of mineral phases to the magma. Roeder & Emslie (1970) argued that basaltic magmas with a Mg# greater than 68 can be considered to be primary, as such a magma of this composition is in equilibrium with mantle olivine (~Fo_{88-92}). Since primary magmas indirectly reflect the composition of the mantle source region it is imperative that primary magma compositions be determined in order to fully understand the chemical nature of a mantle source region.

$$Mg\# = atomic\left[\frac{100Mg}{Mg + Fe}\right]$$

A number of secondary processes can act on the original magma composition, these include alteration by surrounding country rock, contamination by near-surface sediment and interaction with hydrothermal fluid as well as crystal fractionation and accumulation processes. Contamination of the Gough Island primary magmas by hydrothermal processes and interaction with the surrounding country rock and near-surface sediments is assumed to be minimal as the Gough Island lavas do not exhibit low Ce/Pb anomalies expected to be inherited from seawater circulating through the volcanic stack and near-surface sediments (Ben Othman *et al.*, 1989, Class & le Roex, 2008, Plank & Langmuir, 1998). Therefore the calculation of the primary magma compositions for these lavas involves correcting primarily for fractional crystallisation and crystal accumulation processes. The Mg# of a magma undergoing crystal fractionation/accumulation processes changes as ferro-magnesian minerals (e.g. olivine and pyroxene) are either removed or added to the primary magma, and therefore monitoring of the Mg# is useful when calculating primary magma compositions. Both Zielinski & Frey (1970) and le Roex (1985) have argued that the Gough Island lavas have undergone up to 40% fractional crystallisation of olivine and clinopyroxene, which is confirmed petrographically as olivine and clinopyroxene are the major phenocryst phases in this suite of lavas. The accumulation of these two mineral phases is corrected for in the calculation of primary magma compositions (described below).

Table 7-1: Table of mineral/melt partition coefficients used throughout this study.

Element	Grnt	Cpx	Opx	Ol	Sp
Ni	5.1[o]	4.4[a]	1.1[o]	12.20[q]	0.01*
Rb	0.00001[b]	0.0006[b]	0.00045[i]	0.000045[b]	0.0001[j]
Ba	0.00001[b]	0.00068[b]	0.00004[e]	0.000043[b]	0.0001[j]
Th	0.0015[b]	0.003[b]	0.00005[e]	0.00005[b]	0.01*
U	0.027[k*]	0.0052[b]	0.00005[e]	0.00005[b]	0.01*
Ta	0.0084[k*]	0.014[k*]	0.0002[e]	0.000082[k*]	0.06[f]
Nb	0.0042[b]	0.007[b]	0.0001[e]	0.000041[b]	0.08[f]
La	0.001[b]	0.042[b]	0.0005[e]	0.00003*	0.01[j]
Ce	0.005*	0.08*	0.0015*	0.00006[b]	0.01[j]
Pb	0.00012[e]	0.0102[e]	0.0013[i]	0.000069[a]	0.001
Sr	0.003[b]	0.096[b]	0.009[e]	0.008[b]	0.0011[j]
Nd	0.06[b]	0.19[b]	0.0063*	0.0002[i]*	0.01[j]
Sm	0.17[i]*	0.26*	0.0096*	0.0038[i]*	0.01[j]
Zr	0.27[b]	0.128[b]	0.013[e]	0.0013[b]	0.06[f]
Hf	0.115[b]	0.23[b]	0.013[e]	0.005[b]	0.05[f]
Eu	0.38[i]*	0.33[i]*	0.013[e]	0.0007[b]	0.01[j]
Ti	0.688[e]	0.451[e]	0.061[e]	0.009[a]	0.048[j]
Ho	2.3*	0.41[b]	0.035*	0.006[b]	0.01*
Tb	1.13*	0.382[b]	0.023*	0.0023*	0.01*
Pr	0.02*	0.13*	0.0035*	0.00011*	0.01*
Tm	3.7*	0.427*	0.044*	0.012*	0.01*
Gd	0.7[i]*	0.37[b]	0.0175*	0.0013*	0.01[j]
Dy	1.6*	0.402[b]	0.029*	0.0038*	0.01[j]
Er	3.1*	0.422[b]	0.041[e]	0.0087[b]	0.01[j]
Yb	4.18[b]	0.432[b]	0.047[e]	0.016*	0.01[j]
Lu	4.5[b]	0.439[b]	0.052[e]	0.02[b]	0.01[j]

All values are mineral/melt partition coefficients. Abbreviations: Grnt – garnet, Cpx – clinopyroxene, Opx – orthopyroxene, Ol – olivine, Sp – spinel. * indicates values are either calculated or fictional, where calculated values are listed with their respective reference and fictional values have no other reference. References as follows: [a](Beattie, 1993), [b](Donnelly *et al.*, 2004), [c](Foley *et al.*, 2000), [d](Fujimaki, 1986), [e](Hauri *et al.*, 1994), [f](Horn *et al.*, 1994), [g](Kennedy *et al.*, 1993), [h](McKay *et al.*, 1994), [i](McKenzie & O'Nions, 1991), [j](McKenzie & Onions, 1995), [k](Münker *et al.*, 2004), [l](Hauri *et al.*, 1994), [m](Rubatto & Hermann, 2003), [n](Thomas *et al.*, 2002), [o](Mysen, 1978), [p](Hart & Davis, 1978), (Bougault & Hekinian, 1974).

Other mineral phases which have been shown to have contributed to crystal fractionation/accumulation processes in the Gough Island lavas are plagioclase, Fe-Ti oxides (present as ilmenite in the basalts used in this study) and apatite (le Roex, 1985, Zielinski & Frey, 1970). However, it was shown in Chapter 5 that these mineral phases are not important fractionating phases in the more primitive Gough Island lavas (Mg#>~50). This observation is confirmed petrographically, where these mineral phases are either absent or present in small modal abundances in the lavas chosen to be corrected for primary magma compositions. le Roex (1985) also shows that fractionation of the Fe-Ti oxides and apatite only occurs at higher degrees of differentiation than experienced by the lavas in the sample set used in this study.

In order to minimise the necessary corrections, only samples with Mg# >55 (MgO = 6-8wt%; Ni and Cr = 85-250ppm) were used to calculate primary magma compositions. In addition, only fresh, aphyric to moderately porphyritic lavas were used, as these lavas are assumed to have been least affected by late-stage alteration and crystal fractionation/accumulation processes. Thus, ten samples were chosen for primary magma calculations based on the above criteria, and are listed in Table 7-2.

In calculating the fractionation effects on the Gough Island lavas using a least squares approximation technique, le Roex (1985) showed the ratios of accumulated clinopyroxene and olivine were not constant and varied from olivine dominated to clinopyroxene dominated (ol:cpx ratios range from 1:0 to 1:4). Therefore, in order to correct for the effect of crystal fractionation on the major and trace element compositions, clinopyroxene and olivine were added in equal proportions to the primitive lava compositions in 1% increments until an Mg# of 69 was reached. The clinopyroxene composition was kept constant at Wo_{50} En_{20} Fs_{30} (based on microprobe data of clinopyroxene; le Roex (1985)), whereas the equilibrium olivine composition was re-calculated after each increment using the formula:

$$K_d^{Fe-Mg} = \frac{\left(\frac{Fe}{Mg}\right)^{ol}}{\left(\frac{Fe}{Mg}\right)^{liq}} = 0.30 \pm 0.03 \quad \text{(Roeder \& Emslie, 1970)}$$

Trace element concentrations were calculated after each addition of clinopyroxene and olivine using the Rayleigh law for fractional crystallisation:

$$\frac{C_L}{C^0} = F^{(D-1)}$$

C_L = concentration of trace element in fractionated liquid
C^o = concentration of trace element in parental liquid
F = fraction of liquid remaining
D = bulk partition coefficient for trace element

Table 7-2: Table of calculated Gough Island primary magma compositions.

	ALR6G		ALR10G		ALR12G		ALR32G		ALR33G		ALR35G		ALR45G		ALR48G		ALR50G		ALR64G	
	Meas. Conc.	28% Add.	Meas. Conc.	14% Add.	Meas. Conc.	24% Add.	Meas. Conc.	18% Add.	Meas. Conc.	16% Add.	Meas. Conc.	18% Add.	Meas. Conc.	22% Add.	Meas. Conc.	16% Add.	Meas. Conc.	20% Add.	Meas. Conc.	20% Add.
SiO_2	49.48	**48.89**	49.27	**48.94**	47.99	**48.07**	50.68	**49.76**	50.95	**49.87**	48.78	**48.67**	48.34	**48.71**	49.59	**49.02**	49.74	**49.08**	50.24	**49.50**
TiO_2	3.24	**2.46**	3.00	**2.61**	3.26	**2.59**	3.11	**2.58**	3.04	**2.56**	3.40	**2.86**	3.21	**2.62**	3.18	**2.70**	2.97	**2.43**	2.99	**2.44**
Al_2O_3	15.03	**11.39**	14.16	**12.31**	15.70	**12.47**	14.62	**12.14**	14.44	**12.18**	14.08	**11.83**	14.31	**11.69**	14.58	**12.38**	15.21	**12.42**	15.02	**12.27**
Fe_2O_3	1.78	**1.35**	1.71	**1.49**	1.72	**1.37**	1.66	**1.38**	1.67	**1.41**	1.75	**1.47**	1.81	**1.48**	1.75	**1.49**	1.71	**1.40**	1.65	**1.35**
FeO	8.92	**9.63**	8.54	**8.92**	8.59	**9.32**	8.28	**8.77**	8.37	**8.76**	8.77	**9.27**	9.06	**9.69**	8.77	**9.15**	8.57	**9.10**	8.26	**8.85**
MnO	0.15	**0.11**	0.14	**0.12**	0.15	**0.12**	0.13	**0.11**	0.13	**0.11**	0.13	**0.11**	0.15	**0.12**	0.15	**0.13**	0.15	**0.12**	0.14	**0.11**
MgO	6.05	**11.92**	8.09	**10.99**	6.39	**11.50**	7.23	**10.98**	7.55	**10.84**	7.71	**11.46**	7.47	**12.07**	8.00	**11.27**	7.01	**11.19**	6.64	**10.89**
CaO	9.55	**10.17**	8.99	**9.39**	9.94	**10.46**	7.33	**8.07**	7.55	**8.14**	7.94	**8.65**	7.91	**8.84**	8.14	**8.69**	8.59	**9.19**	8.32	**8.98**
Na_2O	2.92	**2.21**	3.33	**2.90**	3.02	**2.40**	4.01	**3.33**	3.91	**3.30**	3.44	**2.89**	3.04	**2.48**	3.31	**2.81**	3.44	**2.81**	3.59	**2.93**
K_2O	1.91	**1.45**	2.13	**1.85**	1.63	**1.29**	2.68	**2.22**	2.60	**2.19**	2.52	**2.12**	2.22	**1.81**	2.19	**1.86**	2.18	**1.78**	2.63	**2.15**
P_2O_5	0.55	**0.42**	0.56	**0.49**	0.53	**0.42**	0.80	**0.66**	0.76	**0.64**	0.80	**0.67**	0.60	**0.49**	0.59	**0.50**	0.59	**0.48**	0.64	**0.52**
LOI	0.86	**0.00**	0.32	**0.00**	1.42	**0.00**	0.36	**0.00**	0.32	**0.00**	0.56	**0.00**	0.94	**0.00**	0.40	**0.00**	0.66	**0.00**	0.47	**0.00**
Total	100.44	**100.00**	100.24	**100.00**	100.34	**100.00**	100.89	**100.00**	101.29	**100.00**	99.88	**100.00**	99.06	**100.00**	100.65	**100.00**	100.82	**100.00**	100.59	**100.00**
Ni	85.0	**244**	202	**342**	94.0	**232**	151	**298**	171	**313**	198	**390**	239	**548**	203	**371**	149	**317**	136	**289**
Rb	23.4	**17.7**	37.0	**32.1**	14.8	**11.6**	49.2	**41.1**	48.6	**41.38**	51.0	**42.6**	32.0	**25.7**	28.5	**24.2**	42.6	**34.8**	49.2	**40.3**
Ba	569	**430**	528	**459**	562	**442**	852	**711**	767	**654**	809	**675**	670	**537**	681	**580**	652	**533**	742	**607**
Th	4.04	**3.05**	4.30	**3.73**	4.17	**3.28**	6.15	**5.13**	6.34	**5.40**	5.27	**4.40**	4.39	**1.98**	3.98	**3.39**	4.61	**3.77**	5.29	**4.33**
U	0.680	**0.516**	0.823	**0.716**	0.747	**0.589**	1.092	**0.914**	0.999	**0.853**	1.10	**0.922**	0.798	**1.99**	0.659	**0.563**	0.936	**0.768**	1.14	**0.932**
Ta	2.34	**1.77**	2.48	**2.16**	2.39	**1.88**	2.62	**2.19**	2.52	**2.15**	2.75	**2.30**	2.47	**1.98**	2.33	**1.99**	2.48	**2.03**	2.83	**2.32**
Nb	40.3	**30.5**	45.2	**39.3**	42.4	**33.3**	49.2	**41.1**	48.7	**41.5**	46.8	**39.1**	43.1	**34.6**	41.2	**35.1**	44.1	**36.1**	53.1	**43.5**
La	45.2	**34.3**	42.9	**37.4**	43.8	**34.6**	51.5	**43.1**	49.8	**42.6**	54.8	**45.9**	46.3	**37.3**	43.8	**37.4**	45.0	**37.0**	61.5	**50.5**
Ce	92.2	**70.5**	88.1	**77.0**	86.6	**68.7**	107.3	**90.3**	103	**88.6**	109	**91.5**	91.6	**74.2**	91.1	**78.1**	87.8	**72.5**	110	**90.6**
Pb	3.60	**2.72**	3.37	**2.93**	3.24	**2.55**	4.48	**3.74**	4.90	**4.17**	5.12	**4.28**	4.54	**1.98**	3.67	**3.13**	3.36	**2.75**	4.19	**3.43**
Sr	728	**557**	777	**680**	734	**584**	830	**699**	797	**684**	930	**783**	775	**628**	710	**610**	686	**566**	687	**568**
Nd	44.3	**34.6**	43.6	**38.5**	41.3	**33.5**	50.8	**43.3**	49.4	**42.9**	53.0	**45.2**	44.6	**36.8**	42.1	**36.6**	39.8	**33.4**	48.9	**41.0**
Sm	9.26	**7.43**	8.67	**7.77**	8.67	**7.17**	9.97	**8.65**	9.82	**8.66**	10.1	**8.80**	8.79	**7.39**	8.57	**7.55**	8.10	**6.92**	9.29	**7.93**
Zr	278	**222**	276	**247**	274	**226**	342	**296**	322	**283**	339	**293**	293	**245**	280	**246**	255	**217**	309	**263**
Hf	5.84	**4.63**	5.61	**4.99**	5.76	**4.72**	7.29	**6.27**	7.15	**6.26**	7.27	**6.26**	6.21	**5.17**	5.84	**5.11**	5.25	**4.45**	6.18	**5.24**
Eu	2.80	**2.34**	2.74	**2.50**	2.71	**2.32**	3.05	**2.72**	3.02	**2.72**	3.10	**2.76**	2.85	**2.47**	2.82	**2.55**	2.62	**2.30**	2.94	**2.58**
Ti	19421	**17205**	17982	**16925**	19541	**17613**	18642	**17245**	18222	**17003**	20380	**18853**	19241	**17494**	19061	**17786**	17802	**16327**	17922	**16437**
Ho	1.12	**1.235**	1.03	**1.09**	1.06	**1.16**	1.022	**1.09**	1.00	**1.06**	1.07	**1.14**	1.03	**1.12**	1.00	**1.06**	1.05	**1.13**	1.12	**1.20**
Tb	1.18	**1.099**	1.09	**1.06**	1.13	**1.07**	1.26	**1.20**	1.23	**1.18**	1.22	**1.17**	1.11	**1.05**	1.07	**1.03**	1.05	**1.00**	1.17	**1.11**
Pr	11.2	**8.64**	11.1	**9.73**	10.51	**8.40**	13.11	**11.1**	12.7	**10.9**	13.6	**11.5**	11.5	**9.33**	10.6	**9.11**	10.3	**8.54**	12.7	**10.5**
Tm	0.361	**0.488**	0.328	**0.381**	0.344	**0.444**	0.297	**0.360**	0.294	**0.349**	0.326	**0.395**	0.322	**0.407**	0.311	**0.368**	0.346	**0.429**	0.351	**0.435**
Yb	2.14	**3.09**	2.00	**2.40**	2.10	**2.88**	1.74	**2.20**	1.70	**2.10**	1.93	**2.44**	1.92	**2.57**	1.90	**2.34**	2.10	**2.74**	2.15	**2.79**
Lu	0.312	**0.471**	0.286	**0.352**	0.302	**0.430**	0.238	**0.311**	0.231	**0.292**	0.268	**0.349**	0.277	**0.383**	0.263	**0.333**	0.295	**0.396**	0.294	**0.396**
Gd	8.41	**7.38**	7.75	**7.26**	7.99	**7.14**	9.22	**8.48**	9.06	**8.40**	8.98	**8.26**	8.14	**7.34**	7.74	**7.19**	7.49	**6.82**	8.37	**7.62**
Dy	6.03	**6.03**	5.59	**5.59**	5.79	**5.79**	5.87	**5.87**	5.74	**5.75**	6.08	**6.08**	5.71	**5.71**	5.50	**5.50**	5.58	**5.58**	6.02	**6.02**
Er	2.64	**3.26**	2.40	**2.67**	2.55	**3.06**	2.26	**2.60**	2.24	**2.53**	2.46	**2.82**	2.42	**2.86**	2.33	**2.64**	2.47	**2.88**	2.65	**3.08**
Mg#	55	**69**	63	**69**	57	**69**	61	**69**	62	**69**	61	**69**	60	**69**	62	**69**	59	**69**	59	**69**

Major oxides in wt% and trace elements in ppm. Percentage addition refers to addition of clinopyroxene and olivine in equal proportions. Calculated primary magma compositions are shown in bold.

Ten primary magma compositions were calculated by the addition of 14-28% of clinopyroxene and olivine, in equal proportions. Calculated primary magma compositions are listed in Table 7-2 and selected samples shown on a chondrite-normalised REE diagram in Fig 7-1. Differences between the calculated primary magma REE patterns do not differ significantly from the uncorrected lava REE patterns, although the La and Lu absolute abundances have decreased up to 24% and 51%, respectively. The primary magmas show an enriched REE pattern with LREE and HREE abundances ~150-200x and 15-20x chondrite, respectively. Very small variations in gradient are exhibited by the different primary magmas, which results in a few crossing REE patterns (between Tb and Dy) and must be considered when determining the composition and mineralogy of the Gough Island mantle source region (discussed in the next section).

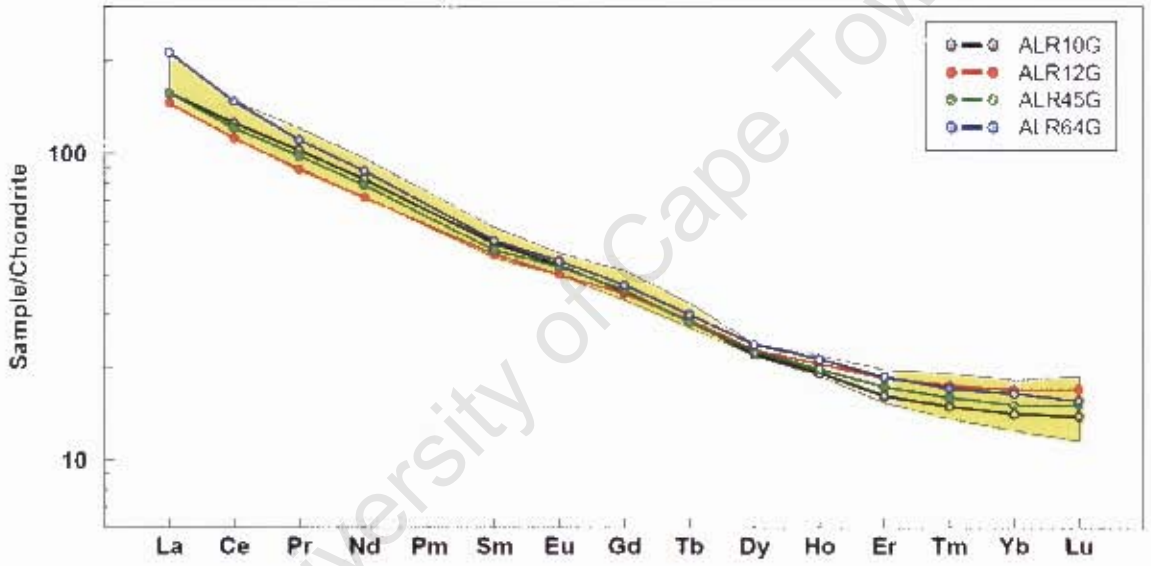

Fig 7-1: Selected chondrite-normalised REE patterns for calculated Gough Island primary magma compositions. Normalisation values from Sun & McDonough (1989). Yellow field represents the range of all calculated Gough Island primary magmas.

7.4 Constrained Forward Modelling

Feigenson *et al.* (1996) introduced the concept of constrained forward modelling by attempting to constrain melting processes involved in producing the Mauna Kea basalts. In order to achieve this, Feigenson *et al.* (1996) argued that melting conditions required to produce a suite of lavas could be constrained by first using a primary magma composition to calculate a potential mantle source region composition, assuming a suitable source mineralogy, followed by the melting of this calculated mantle source region composition using the same set of parameters but at different degrees of partial melting. This latter step produces a range of model melts for various degrees of partial melting, which can be subsequently compared to the suite of primary magma compositions in order to set reasonable constraints for each of the parameters (start and melt modes, melting style and degree of partial melting).

The use of the REE is a powerful tool when attempting to constrain the role of certain minerals during melting processes. This is due to the varying degrees of compatibility of the LREE to HREE in different mantle minerals (expressed as mineral/melt partition coefficients and the REE mineral/melt partition coefficients are well established). It is argued that an OIB mantle source region can be composed of one or a combination of three different rock types; peridotite, eclogite and garnet pyroxenite (Herzberg, 2006, Hirose & Kushiro, 1993, Kogiso *et al.*, 1998, Kogiso & Hirschmann, 2006, Kogiso *et al.*, 2003, Sobolev *et al.*, 2007, Sobolev *et al.*, 2005, Takahashi & Kushiro, 1983). Garnet may or may not be present, depending on the depth of melting (Takahashi, 1986, Walter & Presnall, 1994). Therefore, an understanding the role of garnet is required in order to understand the mineralogical nature of a mantle source region. This can be achieved by modelling REE behaviour in a source with variable garnet, as the compatibility of the REE in garnet increases from the LREE through the MREE to the HREE. Therefore if melting occurred in the presence of garnet, the HREE would be buffered and the melt would have a lower concentration of HREE than MREE and LREE (relative to chondrite).

The remainder of this chapter aims at understanding the mineralogy of the Gough Island mantle source region, through the use of constrained forward modelling methods for each of the rock types capable of producing silica-undersaturated lavas similar in composition to the Gough Island magmas.

7.5 A Peridotite Mantle Source Region

Peridotite, composed of olivine, clinopyroxene, orthopyroxene and garnet or spinel, is the most common rock type in the upper mantle (Jaques & Green, 1980, Kushiro, 1968, Ringwood, 1975, Sun & McDonough, 1995), where spinel is stable at lower pressures (<25-35kbar (Takahashi, 1986, Walter & Presnall, 1994)) and garnet is stable at higher pressures (Kushiro & Yoder, 1966, Ringwood, 1958, Ringwood, 1966, Takahashi, 1986, Walter & Presnall, 1994). Basaltic melts, such as OIB, derived from the upper mantle have long thought to be the product of partial melting of peridotite (Kushiro, 1968, Takahashi, 1986) and as a result many melting experiments have been performed on peridotites using a number of different techniques and approaches (Boyd & England, 1960, Ito & Kennedy, 1967, Jaques & Green, 1980, Johnson & Kushiro, 1992, Kinzler & Grove, 1992, Kushiro *et al.*, 1972, Ohtani & Kumazawa, 1981, Stolper, 1980, Yoder, 1952) in order to fully understand the processes involved in generating melts in the upper mantle.

Jaques and Green (1980) showed experimentally that four main melting fields (Fig 7-2) are present on the peridotite P-T phase diagram, with the first melting field being defined as olivine(Ol)+orthopyroxene(Opx)+clinopyroxene(Cpx)+Al-phase+liquid(L) (where Al-phase is spinel or garnet depending on pressure) as the first melts are formed near the solidus. Since melting results in the removal of chemical components from the source, the source gradually becomes more

refractory (ie increasing Mg/(Mg+Fe) and Cr/(Cr+Al) ratios), this is seen by the removal of Al from spinel/garnet (through Cr-Al substitution), resulting in the formation Cr-spinel (Jaques & Green, 1980). Thus, the second melting field is defined as Ol+Opx+Cpx+Cr-spinel+L. The third and fourth melting fields are marked by the exhaustion of clinopyroxene (Ol+Opx+Cr-spinel+L) and orthopyroxene (Ol+Cr-spinel+L), respectively.

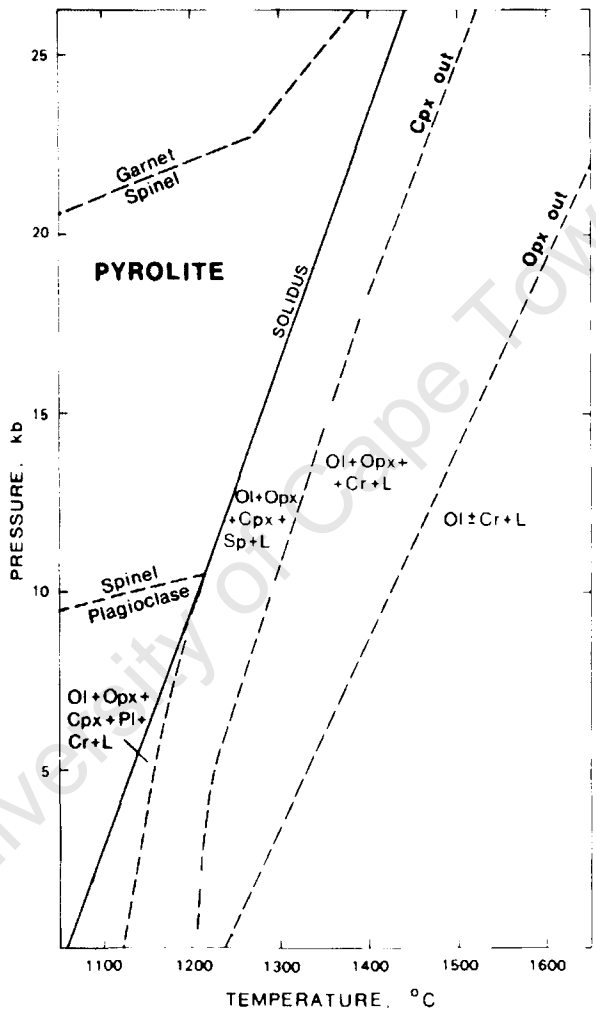

Fig 7-2: P-T diagram for melting of pyrolite adapted from Jaques & Green (1980). Ol – olivine; Opx – orthopyroxene; Cpx – clinopyroxene; Sp – spinel; Cr – chrome spinel; Pl – plagioclase; L – liquid.

Melting experiments have shown that partial melts from a peridotitic source range from silica-saturated to silica-undersaturated as a function of, among others, the degree of partial melting and pressure (Jaques & Green, 1980, Kushiro, 1968), where melts range from alkali olivine basalt (<15% melting) through olivine tholeiite (20-30% melting) to komatiite-picrite (40-60% melting) (Jaques & Green, 1980, Walter & Presnall, 1994) and generally become silica-undersaturated with increasing pressures (Jaques & Green, 1980, Kushiro, 1968). Alkali-olivine basalts are shown to form

by moderate degrees of partial melting above 10kbar (in both the spinel and garnet stability fields) within the second melting field as defined by Jaques & Green (1980) (clinopyroxene still present).

Therefore melting experiments have shown that it is possible to form magma compositions similar to the Gough Island alkali basalt primary magmas as a result of moderate degrees of partial melting of a garnet or a spinel lherzolite mantle source region.

7.5.1 Spinel Lherzolite

Constrained forward modelling of a spinel lherzolite mantle source region first involves calculating a potential mantle source region composition assuming 8% equilibrium melting of the ALR6G primary magma and secondly the calculation of a range of model melt compositions assuming 6-10% equilibrium melting of the potential mantle source region composition. Mineral/melt partition coefficients used in the model are listed in Table 7-1 whereas the start and melt modes are listed in Table 7-3. The spread and gradients of the calculated model melt chondrite normalised REE patterns are subsequently compared to one of the Gough Island primary magmas (ALR35G) which exhibits some of the highest REE abundances and one of the steepest REE patterns of this dataset. The remainder of this section first discusses the validity of the assumptions and parameters used in this model followed by the presentation and discussion of the results.

Even though the spread and gradients of the model melt REE patterns can be changed by adjusting various parameters, the overall shape of the pattern remains the same as this is determined by the primary magma used in the model. Minor changes in both the absolute abundances of REE as well as the gradients of the calculated model melt REE patterns are observed when changing the primary magma composition used in the model. However, the changes are subtle and therefore the primary magma composition used in the model (ALR6G) was chosen because it exhibits some of the lowest REE abundances of any of the Gough Island primary magmas.

Diagrams of Y vs. Zr (Fig 5-4) and Zr/Hf vs. $^{176}Hf/^{177}Hf$ (Fig 6-6) indicate that the Gough Island mantle source region is heterogeneous, however the heterogeneities are assumed to be localised within a single source region as the overall geochemistry of the Lower, Middle and Upper Basalts are identical. Therefore, if the Gough Island mantle source region is composed of spinel lherzolite, it follows that the full range of Gough Island REE patterns should be produced from this source, which includes the full compositional range of REE as well as crossing REE patterns at Dy. Thus, the calculated model melts produced from this source region are compared to one of the Gough Island primary magmas (ALR35G) which exhibits some of the highest REE abundances and one of the steepest REE patterns (Fig 7-3b) out of this dataset.

The spread of the model melt REE patterns can be changed by adjusting the degree of partial melting used in calculating the potential mantle source composition, where an increase in the degree

of partial melting decreases the spread of all the REE. 8% equilibrium melting was chosen for all the peridotitic models as this degree of partial melting is within the acceptable field of partial melting required for producing alkali basalt melts (Jaques & Green, 1980, Walter & Presnall, 1994) and also produces the best correlation between calculated model melt REE patterns and the Gough Island primary magma REE patterns.

The spread and the slope of the model melt REE patterns can also be changed by adjusting the start and melt modes (Table 7-3) as well as the mineral/melt partition coefficients (Table 7-1).

Large variations are observed in literature values for start and melt modes, where values for spinel lherzolite range from having 2-8% spinel, 46-58% olivine, 28-30% orthopyroxene and 10-18% clinopyroxene in the source, with phases entering the melt varying from 5-22% for spinel, 10-45% for olivine, 20-55% for orthopyroxene and 65-67% for clinopyroxene (Class *et al.*, 1994, Johnson *et al.*, 1990, Kelemen *et al.*, 2003). Orthopyroxene, olivine and spinel exercise little control in changing the spread of the model melt REE patterns, whereas a decrease in the spread of all the REE is observed when the start and melt modes for clinopyroxene are increased. However, the start and melt modes for clinopyroxene should not be increased as the chosen values are near the maximum values observed in literature. Also, adjustments to the start and melt modes do not result in a change in the calculated model melt REE patterns and therefore cannot produce crossing REE patterns as observed in the Gough Island primary magmas.

Large variations are also exhibited in literature values for the mineral/melt partition coefficients, where literature values for La and Lu in clinopyroxene range from 0.032 to 0.103 (McKay *et al.*, 1994, Skulski *et al.*, 1994, Sobolev *et al.*, 1996) and 0.223 to 0.958 (Hauri *et al.*, 1994, Johnson, 1994, Skulski *et al.*, 1994), respectively. By increasing the mineral/melt partition coefficients for clinopyroxene (as well as olivine, orthopyroxene and spinel) the spread of the REE for the model melts decreases. Changes in the gradients of the model melt REE patterns are observed when adjusting the mineral/melt partition coefficients; however, unrealistic values are required in order to create crossing REE patterns similar to the Gough Island primary magmas.

Therefore, the parameters used throughout this study are based on literature values, but have been adjusted so as to produce the best correlation between the model melt REE patterns and the Gough Island primary magma REE patterns (for this and all subsequent models).

Based on the assumptions discussed thus far, Fig 7-3a) shows that the calculated REE composition of a spinel lherzolite mantle source region is LREE enriched relative to HREE ($(La/Sm)_N$=2.25) and has LREE and HREE abundances of 12.4x and 2.87x chondrite, respectively. The calculated chondrite normalised REE patterns of model melts derived from this mantle source are sub-parallel, LREE enriched relative to HREE (La=163-220x and Lu=19.4-21.4x chondrite;

$(La/Sm)_N$=2.98-3.59) and exhibit broadly similar absolute abundances of REE as the Gough Island primary magmas. However, the spread of LREE and HREE exhibited by the calculated model melts are larger and smaller, respectively, than the corresponding ranges of the Gough Island primary magmas, where ~6-8% and ~8-17% equilibrium melting covers the ranges of the LREE and HREE, respectively.

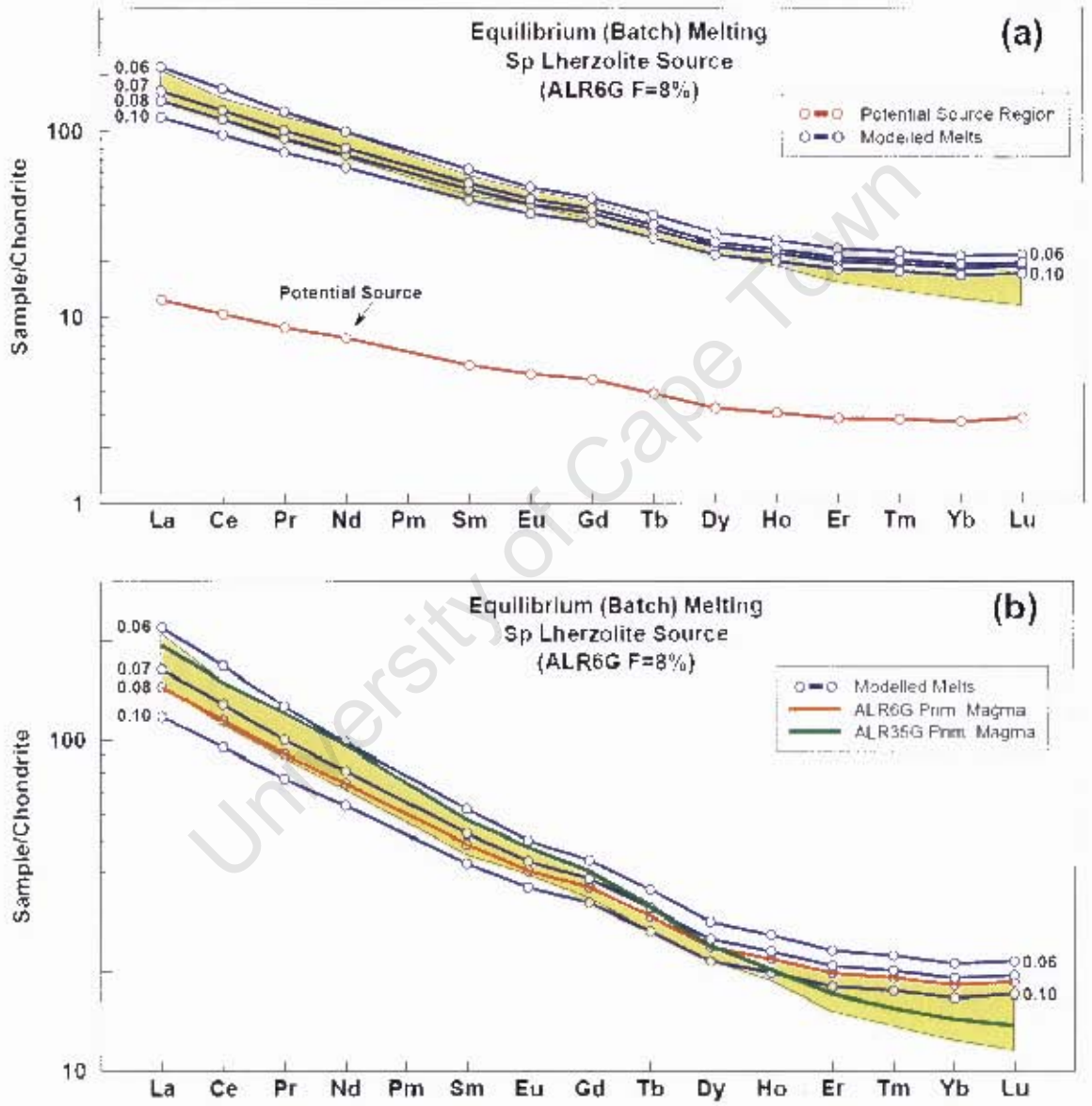

Fig 7-3: a) Chondrite normalised REE patterns for modelled melts calculated for 6-10% equilibrium melting of a spinel lherzolite potential mantle source region composition. The potential mantle source region REE pattern (calculated assuming 8% equilibrium melting of the ALR6G primary magma) is shown by the red line, whereas the blue lines represents the calculated melt REE patterns. b) Chondrite normalised REE patterns for modelled melts calculated for 6-10% equilibrium melting (blue lines) of a spinel lherzolite potential mantle source region composition (shown by the red line in figure a)) shown with two select Gough Island primary magma compositions (ALR6G and ALR35G). The two primary magma compositions were chosen so as to represent two extreme compositions that exhibit crossing REE patterns. In both fig a) and b) the yellow field represents all of the Gough Island primary magma compositions. Normalisation values taken from Sun & McDonough (1989). Mineral/melt partition coefficients are listed in Table 7-1, whereas the start and melt modes are listed in Table 7-3.

The LREE abundances exhibited by ALR35G are produced by 6-7% equilibrium melting of this source whereas 15% equilibrium melting is required to produce similar HREE abundances. Thus a spinel lherzolite mantle source region cannot account for the overall spread of REE exhibited by the Gough Island primary magmas, nor produce melt REE patterns similar to the Gough Island primary magmas nor melt REE patterns that cross at Dy.

Table 7-3: Start and melt modes used throughout this study.

	Sp Lherzolite		Grnt Lherzolite		Garnet Pyroxenite	
	Start Mode (X_o)	Melt Mode (p)	Start Mode (X_o)	Melt Mode (p)	Start Mode (X_o)	Melt Mode (p)
Grnt	-	-	0.03	0.49	0.20	0.47
Cpx	0.17	0.68	0.10	0.43	0.80	0.53
Opx	0.27	0.12	0.29	0.04	-	-
Ol	0.50	0.12	0.58	0.04	-	-
Sp	0.06	0.08	-	-	-	-

Abbreviations: Sp – spinel; Grnt – garnet. All start and melt modes based on values from Class *et al.*, (1994), Donnelly *et al.*, (2004), Johnson *et al.*, (1990), Keleman *et al.*, (1992, 2003), Stracke *et al.*, (2003).

In summation, it is argued that the Gough Island mantle source region is unlikely to be composed of spinel lherzolite, since (a) the spread of the model melt REE is different to that shown by the Gough Island primary magma REE, and (b) partial melts from such a source do not exhibit crossing REE patterns at Dy. Therefore the Gough Island mantle source region must be composed of a different rock type; one which contains a mineral which is able to buffer the HREE during partial melting processes thereby producing melt REE patterns with varying MREE-HREE gradients. One such mineral is garnet, as the HREE are more compatible in garnet than in any of the other mantle minerals. A peridotitic rock which contains garnet is garnet lherzolite.

7.5.2 Garnet Lherzolite

Constrained forward modelling of a garnet lherzolite mantle source region first involves calculating a potential mantle source region composition assuming 8% equilibrium melting of the ALR6G primary magma and secondly the calculation of a range of model melt compositions assuming 5-8% equilibrium melting of the potential mantle source region. The start and melt modes used for this model are listed in Table 7-3 and the mineral/melt partition coefficients used in the spinel lherzolite model, presented in Section 7.5.1, are applied to this model. Similar to Section 7.5.1, the spread and gradients of the calculated model melt chondrite normalised REE patterns are subsequently compared to the ALR35G primary magma. The assumptions used in this model are similar to those made in Section 7.5.1. Therefore the remainder of this section, first discusses the assumptions as applicable to this model followed by the presentation and interpretation of the results.

Similar to the partial melting of a spinel lherzolite source (Section 7.5.1), the gradient and spread of the garnet lherzolite calculated model melt REE patterns can be significantly changed by adjusting parameters such as start and melt modes (Table 7-3), the mineral/melt partition coefficients (Table 7-1), the degree of partial melting or the primary magma composition used in calculating the potential mantle source composition (all, except the choice of primary magma are discussed later, as this was discussed in Section 7.5.1).

For the same reasons as given in Section 7.5.1 the potential mantle source composition was calculated using the Gough Island primary magma ALR6G, as this primary magma exhibits some of the lowest abundances of REE and one of the shallowest REE pattern slopes out of this dataset. It follows that if the Gough Island mantle source region is composed of garnet lherzolite, that the partial melting of this source should produce calculated model melt REE patterns similar to all the Gough Island primary magmas (which includes REE patterns which cross as Dy). Thus, the calculated model melt REE patterns are compared to the Gough Island primary magma ALR35G (Fig 7-4b) as this primary magma exhibits some of the highest REE abundances and the steepest REE pattern slope out of this dataset.

Both the gradient and spread of the model melt REE patterns can be controlled by varying the degree of partial melting used to calculate the mantle source region, where an increase in the degree of partial melting results in steeper model melt REE patterns and a larger and smaller spread of the LREE and HREE, respectively. Therefore, 8% equilibrium melting was chosen for use in all the peridotitic models as this degree of partial melting is within the acceptable field of partial melting required for producing alkali basalt melts (Jaques & Green, 1980, Walter & Presnall, 1994) and also produces the best correlation between calculated model melt REE patterns and the Gough Island primary magma REE patterns.

Large variations are also seen in literature values for start and melt modes for garnet lherzolite, where start and melt modes range from having 8-20% garnet, 54-60% olivine, 17-25% orthopyroxene and 9-15% clinopyroxene in the source, with phases entering the melt varying from 5-42% for garnet, 5-13% for olivine, 5-18% for orthopyroxene and 25-65% for clinopyroxene (Class *et al.*, 1994, Johnson *et al.*, 1990, Kelemen *et al.*, 1992, Kelemen *et al.*, 2003, Stracke *et al.*, 2003). The spread of the MREE-HREE and shape of the calculated melt REE patterns are mainly controlled by the start and melt modes of clinopyroxene and garnet. An increase in either the start or melt modes for these minerals, results in the range of mainly the HREE, but also the MREE, to decrease as the REE patterns become flatter. This is due to buffering of mainly the HREE, but also the MREE, as a result of partial melting processes occurring in the presence of garnet.

The mineral/melt partition coefficients for La and Lu, in garnet, range from 0.01-0.0164 and 3.79-7.1, respectively (Hauri *et al.*, 1994, Johnson, 1994, McKenzie & O'Nions, 1991). An increase in

the partition coefficients, reduce the range of REE abundances and further buffering of the HREE are observed, which results in shallower model melt REE patterns.

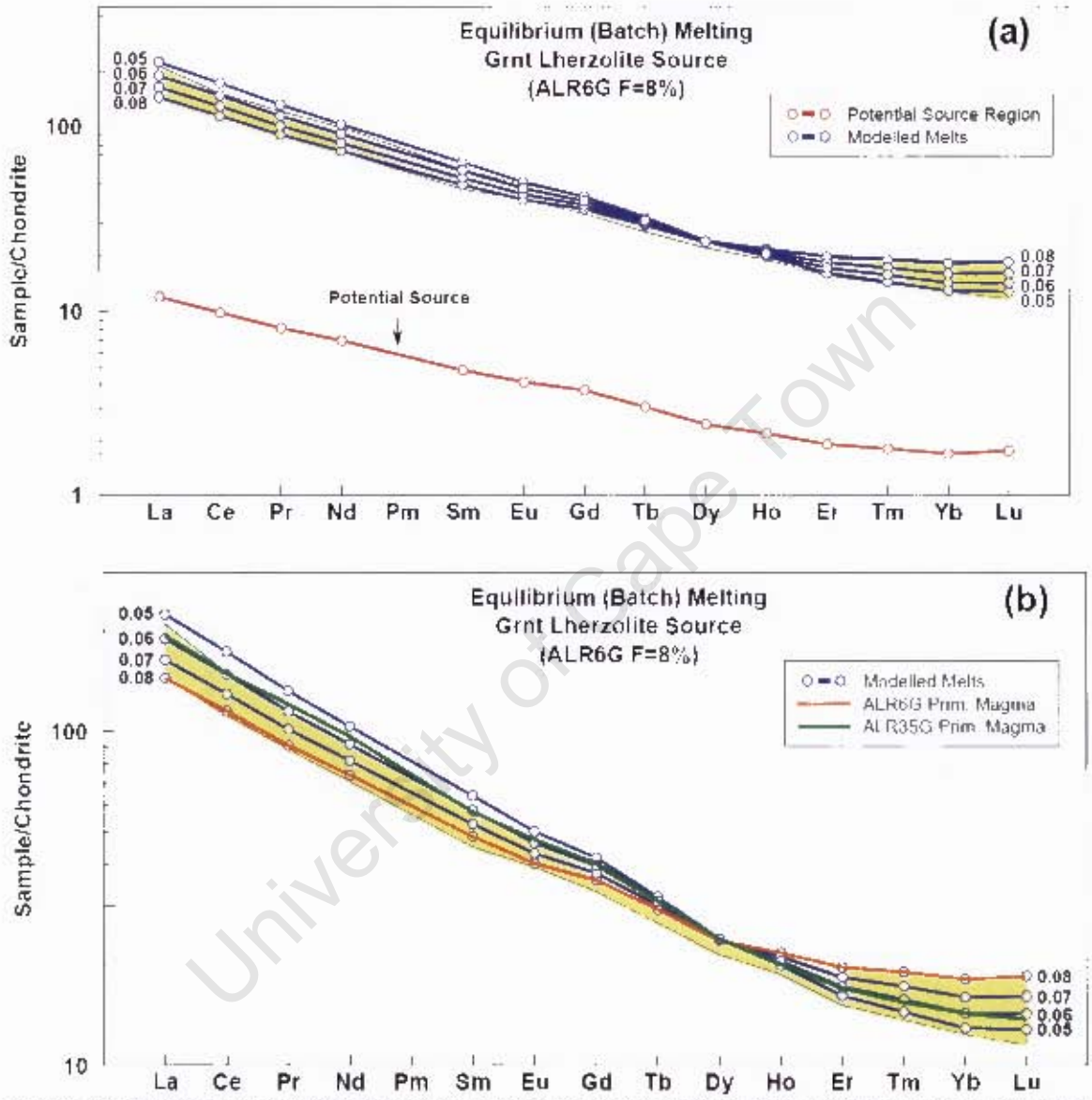

Fig 7-4: a) Chondrite normalised REE patterns for modelled melts calculated for 5-8% equilibrium melting of a garnet lherzolite potential mantle source region composition. The potential mantle source region composition REE pattern (calculated assuming 8% equilibrium melting of the ALR6G primary magma) is shown by the red line, whereas the blue lines represents the calculated melt REE patterns. b) Chondrite normalised REE patterns for modelled melts calculated for 5-8% equilibrium melting (blue lines) of a garnet lherzolite potential mantle source region composition (shown by the red line in figure a)) shown with two select Gough Island primary magma compositions (ALR6G and ALR35G). The two primary magma compositions were chosen so as to represent two extreme primary magma compositions that exhibit crossing REE patterns. In both fig a) and b) the yellow field represents all of the Gough Island primary magma compositions. Normalisation values taken from Sun & McDonough (1989). Mineral/melt partition coefficients are listed in Table 7-1, whereas the start and melt modes are listed in Table 7-3.

Based on the assumptions discussed thus far, Fig 7-4a) shows that the calculated REE composition of a garnet lherzolite source is LREE enriched relative to HREE ($(La/Sm)_N$=2.51) and has LREE and HREE abundances of 12.0x and 1.74x chondrite, respectively. The calculated chondrite normalised REE patterns of melts derived from a garnet lherzolite mantle source region (5-8% equilibrium melting of ALR6G primary magma) are LREE enriched relative to HREE (La=190-

225x and Lu=12.8-14.3x chondrite; $(La/Sm)_N$=2.98-3.49), exhibit similar absolute abundances of REE as the Gough Island primary magmas and exhibit crossing REE patterns at Dy. The spread for both the LREE and HREE for 5-8% equilibrium melting covers the entire compositional range of the Gough Island primary magmas.

The model melt REE pattern which corresponds to 6% equilibrium melting is near-identical, in both REE pattern slope and absolute abundances of all the REE, to the Gough Island primary magma ALR35G. Also, the calculated model melt REE patterns for 5-8% equilibrium melting exhibit crossing REE patterns at Dy.

In summation, the Gough Island mantle source region must contain a mineral, such as garnet, which is able to buffer the HREE during partial melting events, thereby producing partial melt REE patterns with varying MREE-HREE gradients. Therefore, it is argued that the Gough Island mantle source region could be composed of a garnet lherzolite.

7.6 Pyroxenite Mantle Source Region

Recently, it has been argued that pyroxenite and eclogite may be present in the source regions of some OIB, such as Hawaii (Sobolev *et al.*, 2007, Sobolev *et al.*, 2005). The presence of eclogite in the shallow mantle is argued to occur by the incorporation of recycled oceanic crust into rising plumes (Sobolev *et al.*, 2007). Melting experiments have shown that the solidus for eclogite is lower than that for peridotite and therefore entrained eclogite can be expected to undergo decompression melting in the rising plume prior to melting of peridotite (Kogiso & Hirschmann, 2006, Sobolev *et al.*, 2007). Melts derived from eclogite have been suggested by Sobolev *et al.* (2007) to be silica-rich (tholeiitic). However, melting experiments have shown that it is possible to form a nepheline-normative, silica-undersaturated melt if the recycled eclogite component had experienced fractional removal of fluids or melts either during subduction or during transport through the mantle prior to decompression melting (Kogiso & Hirschmann, 2006). The nepheline-normative melts produced from the decompression melting of such a melt-depleted eclogite are able to satisfactorily explain the high FeO* and CaO as well as the low Al_2O_3 and SiO_2 trends of alkali basalts if decompression melting occurs between ~3-5 GPa (Kogiso & Hirschmann, 2006). However, the MgO concentration of the produced melts is too low, which suggests that eclogite derived melts require further interaction with mantle peridotite prior to eruption in order to satisfy the magnesian content of alkali OIB and therefore the eclogite derived melts only contribute a low Al_2O_3 and high FeO* component to the alkali OIB primary magmas (Kogiso & Hirschmann, 2006).

It is also argued that a garnet pyroxenite can be produced in the rising plume, by reacting the low SiO_2 eclogite derived decompression melts with the surrounding mantle peridotite (Fig 7-5). The OIB primary magmas can be subsequently generated by the decompression melting of the garnet pyroxenite product at shallower mantle depths (Kogiso *et al.*, 2003, Sobolev *et al.*, 2007). This is

confirmed through melting experiments that show that it is possible to form either an alkali (silica-undersaturated) or a tholeiitic (silica-saturated) melt from garnet pyroxenite, depending on silica content of the source garnet pyroxenite (Hirschmann *et al.*, 2003, Keshav *et al.*, 2004, Kogiso *et al.*, 2003). Kogiso *et al.* (2003) distinguishes between silica-excess and silica-deficient garnet pyroxenites as pyroxenites either with or without a silica-rich phase, such as quartz. Melting experiments on MIX1G (a silica-deficient garnet pyroxenite) between 2.0-7.5 GPa (Hirschmann *et al.*, 2003, Kogiso *et al.*, 2003) have shown that the melts produced are strongly nepheline-normative and between 2.5-5.0 GPa have similar major element compositions to ocean island alkali basalts (low SiO_2, Al_2O_3 and high CaO at moderate MgO) (Kogiso *et al.*, 2003).

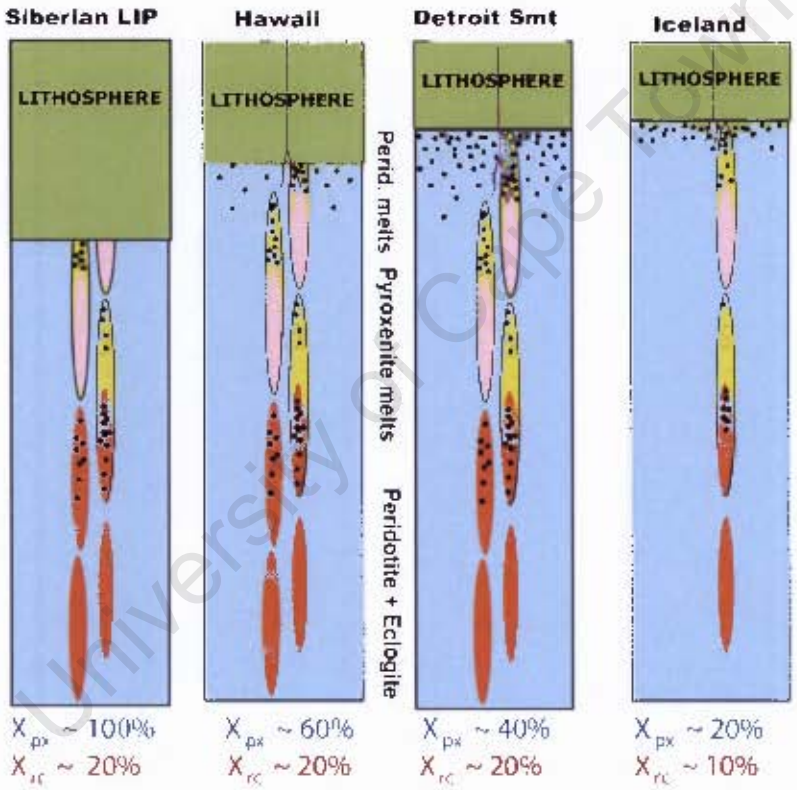

Fig 7-5: Schematic diagram from Sobolev *et al.* (2007), showing the processes involved with injecting eclogite (recycled oceanic crust; represented by orange ellipses) into the shallow mantle in a rising plume. At shallow mantle conditions, the eclogite experiences decompression melting which produces a melt (lower set of black dots) that reacts with peridotitic olivine (blue area) to form a reaction pyroxenite (yellow ellipses) and an eclogite restite (pink ellipses). Pyroxenite melts preferentially to mantle peridotite and therefore primary magmas are the product of mixing of magmas from a pyroxenite source and a peridotite source. The mixture of pyroxenite and peridotite melts is dependant on lithospheric thickness, where a thick lithosphere results in purely pyroxenite derived melts and a thin lithosphere results in a larger proportion of peridotite derived melts Sobolev *et al.* (2007). X_{px} – proportion of pyroxenite in final pyroxenite-peridotite derived melt; X_{ec} – proportion of eclogite (recycled oceanic crust) injected into the upper mantle.

Melting a source region with both peridotite and garnet pyroxenite, results in a primary magma comprised of a mixture of these two rock types. The proportions of melt derived from each source is dependent on lithospheric thickness (thick lithosphere inhibits shallow melting of peridotite)

and the potential temperature (amount of eclogite transported by the rising plume is affected by the buoyancy of the plume which, in turn, is dependent on the potential temperature) (Sobolev et al., 2007, Sobolev et al., 2005).

7.6.1 Garnet Pyroxenite

Constrained forward modelling of a garnet pyroxenite mantle source region first involves calculating a potential mantle source region composition assuming 50% equilibrium melting of the ALR6G primary magma and secondly the calculation of a range of model melt compositions assuming 30-50% equilibrium melting of the potential mantle source region. The start and melt modes used for this model are listed in Table 7-3 and the mineral/melt partition coefficients used in the spinel lherzolite model, presented in Section 7.5.1, are applied to this model. Similar to Section 7.5.1, the spread and gradients of the calculated model melt chondrite normalised REE patterns are subsequently compared to the ALR35G primary magma. The assumptions used in this model are similar to those made in Section 7.5.1. Therefore, the remainder of this section first discusses the assumptions as applicable to this model, followed by the presentation and interpretation of the results.

Similar to the partial melting of a spinel lherzolite source (Section 7.5.1), the gradient and spread of the garnet pyroxenite calculated model melt REE patterns can be changed by adjusting parameters such as start and melt modes (Table 7-3), the mineral/melt partition coefficients (Table 7-1), the degree of partial melting or the primary magma composition used (ALR6G for the same reasons given in Section 7.5.1) in calculating the potential mantle source composition.

Both the gradient and spread of the model melt REE patterns can be controlled by varying the degree of partial melting used to calculate the mantle source region, where a decrease in the degree of partial melting results in an increase in the LREE and a decrease in the HREE. This adjustment results in the LREE-MREE and the LREE-HREE gradients for the model melt REE patterns to increase and decrease, respectively. A decrease in the degree of partial melting results in the spread of the LREE to increase and the HREE to decrease. The primary magma composition was chosen to undergo 50% equilibrium melting, as this produces the best correlation between calculated model melt REE patterns and the Gough Island primary magma REE patterns and is also based on work by Sobolev *et al.*, (2005).

Literature start modes for garnet and clinopyroxene in a garnet pyroxenite are 20% and 80%, respectively, with melt modes for the same minerals being 11% and 89%, respectively (Donnelly *et al.*, 2004). By decreasing the modal abundance (start mode) of garnet present in the source (thereby increasing the modal abundance of clinopyroxene), the HREE are less buffered and exhibit a larger spread in absolute abundance. The slope of the MREE-HREE therefore becomes steeper for lower degrees of partial melting (and vice versa when increasing the modal abundance of garnet in the source). A decrease in the melt mode of garnet (thereby increasing the melt mode of clinopyroxene),

results in increased buffering of the HREE which decreases the spread of the HREE exhibited by the model melts and results in the MREE-HREE slope becoming flatter for 30-50% degrees of partial melting. The same affect on the model melt REE patterns is exhibited when increasing the mineral/melt partition coefficients for garnet and clinopyroxene.

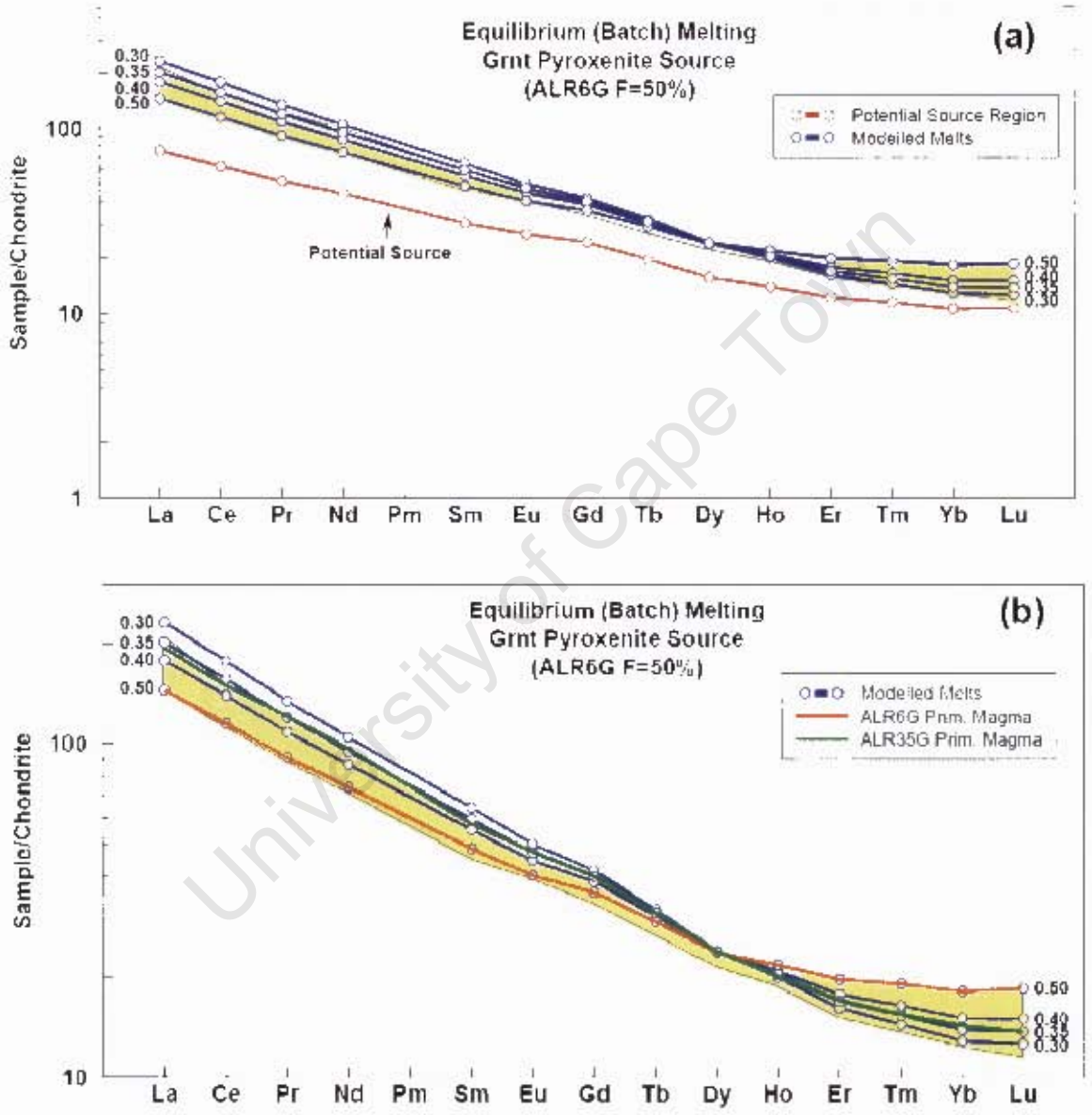

Fig 7-6: a) Chondrite normalised REE patterns for modelled melts calculated for 30-50% equilibrium melting of a garnet pyroxenite potential mantle source region composition. The potential mantle source region composition REE pattern (calculated assuming 50% equilibrium melting of the ALR6G primary magma) is shown by the red line, whereas the blue lines represents the calculated melt REE patterns. b) Chondrite normalised REE patterns for modelled melts calculated for 30-50% equilibrium melting (blue lines) of a garnet pyroxenite potential mantle source region composition (shown by the red line in figure a)) shown with two select Gough Island primary magma compositions (ALR6G and ALR35G). The two primary magma compositions were chosen so as to represent two extreme primary magma compositions that exhibit crossing REE patterns. In both fig a) and b) the yellow field represents all of the Gough Island primary magma compositions. Normalisation values taken from Sun & McDonough (1989). Mineral/melt partition coefficients are listed in Table 7-1 whereas the start and melt modes are listed in Table 7-3.

Based on the assumptions discussed thus far, Fig 7-6a) shows that the calculated REE composition of a garnet pyroxenite source is LREE enriched relative to HREE $(La/Sm)_N=2.46$ and

has LREE and HREE abundances of 75.7x and 10.7x chondrite, respectively. The calculated chondrite normalised REE patterns for melts derived from this source (30-50% equilibrium melting of ALR6G primary magma) are LREE enriched relative to HREE (La=201-231x and Lu=12.7-13.7x chondrite; $(La/Sm)_N$=2.98-3.59) and exhibit crossing patterns at Dy as well as similar REE abundances as the Gough Island primary magmas. The spread of the LREE for the model melts are slightly larger than the spread of the HREE, where ~32-50% and ~28-50% covers the ranges of the LREE and HREE, respectively, exhibited by the Gough Island primary magmas.

The model melt REE pattern which corresponds to 35% equilibrium melting is near-identical, in both REE pattern slope and absolute abundances of all the REE, to the Gough Island primary magma ALR35G. Also, the calculated model melt REE patterns for 30-50% equilibrium melting exhibit crossing REE patterns at Dy.

In summation, the Gough Island mantle source region can be composed of a garnet pyroxenite. This suggests that the Gough Island mantle source region could contain an ancient recycled lithospheric component responsible for the EM type isotope ratios of the Gough Island lavas (Sobolev *et al.*, 2007, Sobolev *et al.*, 2005). This is explored further in Chapter 8.

7.7 Summary of Mantle Source Region Modelling

Constrained forward modelling indicates that the production of the Gough Island lavas cannot be accounted for by the partial melting of a spinel lherzolite mantle source region. This is because a spinel lherzolite mantle source region is incapable of producing similar abundances of LREE and HREE, for the same degree of partial melting, as the Gough Island suite of lavas and is also incapable of accounting for the production of the ALR35G primary magma composition or the crossing REE patterns at Dy.

Constrained forward modelling indicates that the Gough Island lavas can be produced by the partial melting of a garnet rich source such as a garnet lherzolite or a garnet pyroxenite. Both of these models produce calculated model melt REE patterns which cross at Dy, plot within the Gough Island composition field and are similar in shape to the ALR35G primary magma composition. However, constrained forward modelling of REE does not allow for any distinction between a garnet pyroxenite or a garnet lherzolite mantle source region to be made. Therefore, it is concluded that the Gough Island mantle source region is rich in garnet and is either composed of a garnet lherzolite or a garnet pyroxenite.

This conclusion indicates that the Gough Island array should exhibit a steep gradient in $^{176}Hf/^{177}Hf$ vs. $^{143}Nd/^{144}Nd$ space and exhibit low $^{176}Hf/^{177}Hf$ isotope ratios as a result of the Garnet Effect (discussed in Section 6.2). In Chapter 6 that the Gough Island lavas do exhibit low $^{176}Hf/^{177}Hf$ isotope ratios in comparison to other OIB but the Gough Island array does not exhibit a steep gradient,

but rather a gradient approximately the same as the Hf-Nd mantle array line. This indicates that even though the REE concentrations of these lavas is accounted for by partial melting of a garnet rich source, the Hf-isotope composition of these lavas may be better accounted for by another process.

8 Evolution of the Gough Island Mantle Source Region

8.1 Introduction

Numerous studies of OIB from around the world have argued that the enriched trace element and isotope compositions of OIB require involvement of a lithospheric component. Many arguments have been made as to what this component consists of, but some of the more common suggestions include delaminated sub-continental lithospheric mantle (SCLM) (Class & le Roex, 2006, Gibson *et al.*, 2005, Lustrino, 2005, Milner & le Roex, 1996), recycled continental crustal material (terrigenous sediment or lower crust) and/or recycled oceanic sediments (pelagic sediments) (Andres *et al.*, 2002, Chauvel *et al.*, 1992, Eisele *et al.*, 2002, Salters & White, 1998, Weaver, 1991, White & Hofmann, 1982).

The Gough Island lavas are amongst the most geochemically unique OIB from around the world and therefore a better understanding of the interaction of an OIB mantle source region with a recycled lithospheric component can be gained by studying these lavas. This chapter aims to use binary mixing calculations between compiled datasets of SCLM, lower crust and modern marine sediments with an assumed, suitable starting mantle source region composition to determine whether the addition of any of these components can account for the unusual composition of the Gough Island mantle source region.

8.1.1 The Gough Island Suite of Lavas

Global OIB and MORB samples exhibit contrasting compositions in isotope space (Fig 6-4 and Fig 6-5), MORB samples tend to cluster together whereas OIB fan away from the MORB cluster (Hofmann, 1997, Zindler & Hart, 1986). This trend suggests that the various global OIB plot on a mixing line between less radiogenic (depleted relative to PM) and more radiogenic (enriched relative to PM) mantle components (Hart, 1988, Hart *et al.*, 1992, Hofmann, 1997, Zindler & Hart, 1986).

Since the Gough Island lavas exhibit some of the most enriched (relative to PM) $^{176}Hf/^{177}Hf$ (0.282699±12 – 0.282778±10), $^{143}Nd/^{144}Nd$ (0.512517±9 – 0.512596±23) and $^{87}Sr/^{86}Sr$ (0.704859±12 – 0.705321±12) isotope ratios of all OIB, these lavas may exhibit a strong contribution from an isotopically enriched (relative to PM) recycled component. These lavas also exhibit anomalously high Ba/Nb ratios (11.6-18.0; discussed in Chapter 5) and prominent negative Ce-anomalies (0.92-1.04) (Class & le Roex, 2008). Their combined characteristics make Gough Island lavas unique within the global OIB dataset.

8.1.2 Ce-Anomalies

Ce anomalies are expressed as $(Ce/Ce^*)_{Nd}$ which is defined as the ratio between Ce_N (chondrite normalised Ce) and the interpolated Ce_N concentration of a smooth REE pattern calculated from the neighbouring elements in a chondrite normalised REE diagram (i.e. La_N and Nd_N).

$$\left(\frac{Ce}{Ce*}\right)_{Nd} = \frac{Ce_N}{[(La_N)^{2/3}(Nd_N)^{1/3}]}$$

Equation 8.1: Calculation of Ce-anomalies relative to La and Nd, expressed as $(Ce/Ce^*)_{Nd}$ (Class & le Roex, 2008).

Ce anomalies present in OIB can be used in determining the contribution of recycled sediment to intra-plate magmatism (Ben Othman *et al.*, 1989, Class & le Roex, 2008, Shimizu *et al.*, 1992, White *et al.*, 1985). This is because Ce can be oxidised to Ce^{4+} under highly oxidising conditions, whereas all other REE remain in a trivalent oxidation state, thus allowing fractionation of Ce^{4+}, relative to other REE, to occur (Class & le Roex, 2008). Fe-Mn flocs and manganese nodules exhibit a positive Ce anomaly as a result of preferential scavenging of Ce^{4+} from ocean water (Elderfield *et al.*, 1981, Piper, 1974), which results in ocean water exhibiting a complementary negative Ce anomaly (Elderfield & Greaves, 1982). Therefore sediment in the oceans are able to inherit the negative Ce-anomaly from the ocean water (Ben Othman *et al.*, 1989, Cronan & Hodkinson, 1997, Hole *et al.*, 1984, Plank & Langmuir, 1998, Toyoda *et al.*, 1990) and when recycled and mixed with a mantle source region can result in the source region developing a negative Ce-anomaly signature.

8.1.3 Previous Work

On the basis of trace element and limited Sr and Nd isotope data, le Roex (1985) argued that the Gough Island mantle source region must have been enriched relative to a more depleted MORB source region. This argument was based on low Zr/Nb, Y/Nb and high Ba/Nb trace element ratios present in the Gough Island lavas. le Roex (1985) suggested that the high Ba/Nb ratios could have formed as a result of veining by low degree partial melts, metasomatic fluids or sediment recycling. Willbold & Stracke (2006) argued, based on previously measured trace element data (le Roex, 1985, Weaver *et al.*, 1987), that the trace element geochemistry of the Gough Island lavas can be explained by a recycled oceanic lithospheric component with variable upper and lower continental crust.

Recently, Class & le Roex (2008) argued, based on high precision trace element data, that the Gough Island lavas exhibit a significant negative Ce-anomaly, which they argue did not form by near-surface contamination or by weathering processes since the Ce/Pb ratios are typical for OIB compositions. They argue that the negative Ce anomaly formed as a result of the interaction of the Gough Island mantle source region with a recycled sediment component which had a negative Ce anomaly that developed prior to subduction.

All of these previous studies have argued that the Gough Island lavas must have formed from a mantle source region which interacted with a recycled component. Thus the models presented in the remainder of this Chapter involve calculating binary mixing curves between a suitable starting component (discussed later) and marine sediment, SCLM or lower crust using the key geochemical ratios discussed thus far (i.e. Ba/Nb, $^{176}Hf/^{177}Hf$, $^{143}Nd/^{144}Nd$, $^{87}Sr/^{86}Sr$ and $(Ce/Ce^*)_{Nd}$).

8.2 End-Member Components used in Binary Mixing Calculations

The calculated binary mixing curves presented in this Chapter are between various end-member compositions from various datasets. In order to produce meaningful models and due to the limited availability of geochemical data, special consideration had to be taken in choosing each of the datasets. This section aims at introducing each of the datasets and end-member compositions as well as discussing any assumptions made in compiling the datasets so as to allow for a meaningful interpretation of the results.

- **Lower Crust**

The Lower Crust dataset consists of lower crustal xenoliths from the Namaqua-Natal belt, South Africa (le Roex & Class, unpublished data; Long, 2005). Lower crustal xenoliths exhibit high Ba/Nb ratios (7.72-3384) as well as predominantly positive Ce-anomalies (0.93-1.17).

- **SCLM**

The SCLM dataset consists of 18 garnet lherzolite mantle xenolith samples originating from the Kaapvaal Craton, South Africa (Gregoire *et al.*, 2003). The compositions of these samples are reconstituted from analyses of constituent minerals and exhibit high Ba/Nb ratios (5.00-86.7) as well as predominantly positive Ce-anomalies (0.94-1.12).

- **Modern Marine Sediments**

Vervoort *et al.*, (1999) measured $^{143}Nd/^{144}Nd$ and $^{176}Hf/^{177}Hf$ isotope ratios of numerous types of sediments from around the world. Their dataset includes 35 pelagic, deep-sea turbidite and river sediments as well as 73 ancient sediments from various ages and depositional environments. The modern deep-sea turbidite and pelagic sediments (33 samples) are used here to represent global modern marine sediments. Trace element data for these sediments are reported by McLennan *et al.*, (1990). These sediments exhibit $^{176}Hf/^{177}Hf$ and $^{143}Nd/^{144}Nd$ isotope ratios that range between 0.281279 to 0.283153 and 0.511320 to 0.513060, respectively, and form a linear array in Hf-Nd isotope space which Vervoort *et al.*, (1999) termed the Hf-Nd crustal array line ($\varepsilon Hf=1.34\varepsilon Nd+2.82$). These sediments exhibit Ba/Nb ratios which range from 12.5 to 201 and a $(Ce/Ce^*)_{Nd}$ ratio which ranges from 0.65 to 1.93.

Plank & Langmuir (1998) measured trace element concentrations as well as $^{143}Nd/^{144}Nd$ and $^{87}Sr/^{86}Sr$ isotope data for a number of subduction zone sediment columns from around the world in order to understand the nature and composition of global subducting sediments. These sediment columns range in $^{143}Nd/^{144}Nd$ from 0.511820 to 0.512670 with Ba/Nb and $(Ce/Ce^*)_{Nd}$ ratios ranging from 11.1 to 1428 and 0.36 to 1.28, respectively. Since Plank & Langmuir (1998) did not report $^{176}Hf/^{177}Hf$ isotope ratios for these sediments, they were calculated using the Hf-Nd crustal array line ($\varepsilon Hf=1.34\varepsilon Nd+2.82$) of Vervoort *et al.*, (1999) and range from 0.282247 to 0.282875. Plank & Langmuir (1998) also estimated an average global subducting sediment composition, which they

termed GLOSS (global subducting sediment column) and is defined as having a $^{143}Nd/^{144}Nd$ isotope ratio of 0.51218 and a Ba/Nb ratio of 86.8. GLOSS exhibits a $(Ce/Ce^*)_{Nd}$ ratio of 0.99, similar to the average subducting sediment columns. The $^{176}Hf/^{177}Hf$ isotope ratio was not reported for GLOSS and therefore was calculated using the Hf-Nd crustal array line ($\varepsilon Hf=1.34\varepsilon Nd+2.82$) of Vervoort *et al.*, (1999) and yields a value of 0.282513.

8.2.1 Starting Composition

In order to calculate binary mixing curves, a starting end-member composition representing the Gough Island mantle source region prior to enrichment is needed. As discussed above, OIB are argued to plot along mixing lines between more depleted (relative to PM) and more enriched (relative to PM) mantle components (Hart, 1988, Hart *et al.*, 1992, Hofmann, 1997, Zindler & Hart, 1986). Possible enriched (relative to PM) end-member components include SCLM, lower crust and marine sediment, whereas one possible depleted end-member component could be depleted MORB mantle (DMM). However, Fig 8-1 clearly shows that the Gough Island array does not extend towards DMM in $^{176}Hf/^{177}Hf$-Ba/Nb-Zr/Nb space and therefore this end-member cannot be significantly involved in the production of these lavas.

The possibility of a PM starting composition was also investigated (Fig 8-1). A binary mixing curve between PM and GLOSS plots parallel to the Gough Island array in Ba/Nb vs. $^{176}Hf/^{177}Hf$ isotope space, however, the Zr/Nb ratios of a PM component are too high to account for the Gough Island array in Ba/Nb vs. Zr/Nb space.

Since the focus of this study is to determine the role that a recycled lithospheric component plays in producing the geochemically anomalous Gough Island lavas and not OIB in general, it was assumed that the starting mantle source composition reflects a mantle source region of typical OIB. Therefore, it was decided to use a starting end-member composition which reflects Bouvet, Ascension Island and Marion Island OIB (end-member composition and respective references listed in Table 8-1). The OIB end-member composition reflects similar trace element concentrations and Hf-Nd-Sr isotope ratios as the islands mentioned above, however due to the limited availability of $^{176}Hf/^{177}Hf$ isotope data for these islands, an average $^{176}Hf/^{177}Hf$ isotope ratio was calculated by using the Hf-Nd mantle array line ($\varepsilon Hf=1.34\varepsilon Nd+2.82$) of Vervoort *et al.*, (1999) and yielded a value of 0.283112. The calculated $^{143}Nd/^{144}Nd$ and $^{87}Sr/^{86}Sr$ isotope ratios are 0.512990 and 0.70332, respectively, whereas the calculated Ba/Nb and Zr/Nb ratios are 6.70 and 5.99, respectively. The assumed trace element and isotope ratios of a generic OIB end-member are used in the subsequent models, unless otherwise stated.

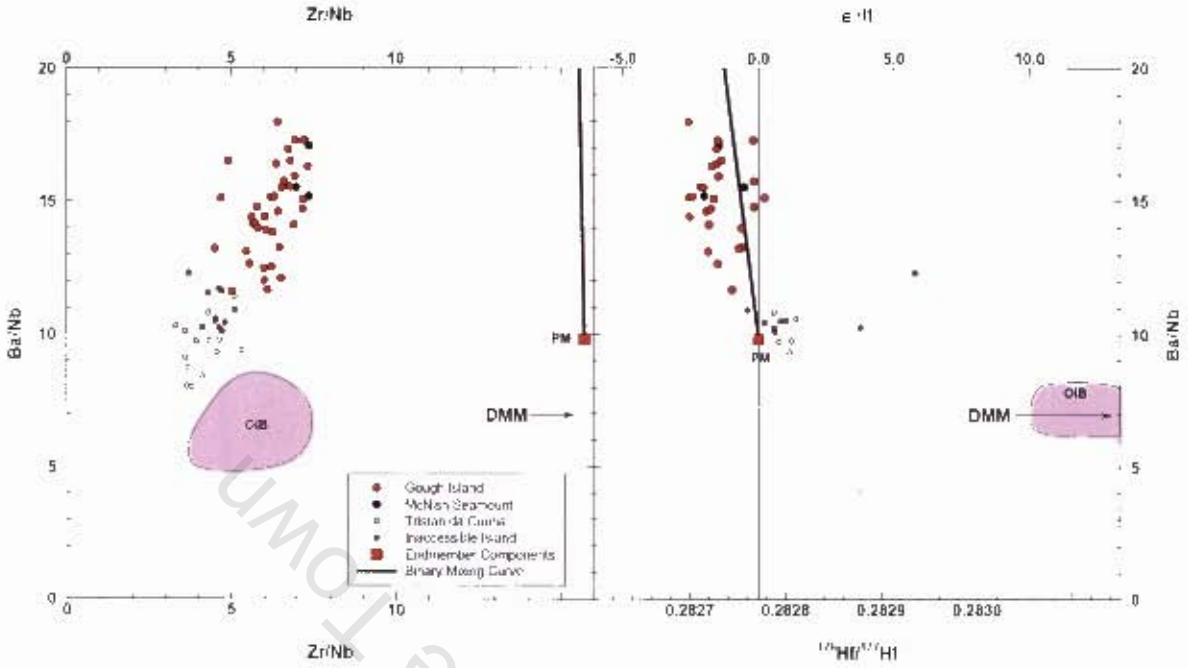

Fig 8-1: Gough Island and the McNish Seamount represented in Ba/Nb vs. Zr/Nb and $^{176}Hf/^{177}Hf$ space superimposed on a binary mixing curve between PM and GLOSS end-member compositions. Tristan da Cunha, Inaccessible Island, DMM and a field representing Marion Island, Bouvet and Ascension Island OIB are shown for comparison. $^{176}Hf/^{177}Hf$ isotope data for Bouvet and Marion Island from Janney & le Roex (2005); trace element data for Bouvet from le Roex & Erlank (1982). Trace element data for Tristan da Cunha and Inaccessible Island from Class & le Roex (unpublished data); $^{176}Hf/^{177}Hf$ isotope data for Tristan da Cunha and Inaccessible Island from Class *et al.*, (unpublished data). References for OIB data listed in the caption for Table 8-1. $^{176}Hf/^{177}Hf$ isotope ratio for GLOSS, Plank & Langmuir (1998), was calculated using the Hf-Nd crustal array line (εHf=1.34εNd+2.82) from Vervoort *et al.*, (1999). εHf calculated using $(^{176}Hf/^{177}Hf)_{CHUR}$ of 0.282772 (at t (0Ga). DMM from Salters & Stracke (2004), PM from Sun & McDonough (1989).

Table 8-1: Assumed OIB mantle source region composition used in all mixing models.

Trace Element Concentrations (ppm)		Trace Element and Isotope Ratios	
Hf	0.68	Ba/Nb	6.70
Ba	33.4	Zr/Nb	5.99
Zr	29.9	Nb/Hf	7.30
Nb	4.99	Hf/Nd	0.16
Sr	57.6	Nd/Sr	0.073
Ce	7.53	$^{176}Hf/^{177}Hf$	0.283112
La	3.41	$^{143}Nd/^{144}Nd$	0.512980
Nd	4.22	$^{87}Sr/^{86}Sr$	0.703332

Assumed OIB mantle source region composition ratios fall within fields of Bouvet, Marion Island and Ascension Islands. Trace element concentrations (ppm) are calculated by assuming 10% melting of a typical peridotite source giving rise to those lavas. $^{176}Hf/^{177}Hf$ isotope ratio was calculated by using the Hf-Nd mantle array line (εHf=1.34εNd+2.82) of Vervoort *et al.*, (1999). Marion Island trace element data as well as Bouvet and Marion Island isotope data from Janney & le Roex (2005); Bouvet trace element data from le Roex & Erlank (1982); all other OIB data from the PETDB (http://www.petdb.org) and precompiled files of the GEOROC (http://georoc.mpch-mainz.gwdg.de/georoc/) databases.

8.3 Geochemistry of End-Member Components

8.3.1 $(Ce/Ce^*)_{Nd}$ Ratios

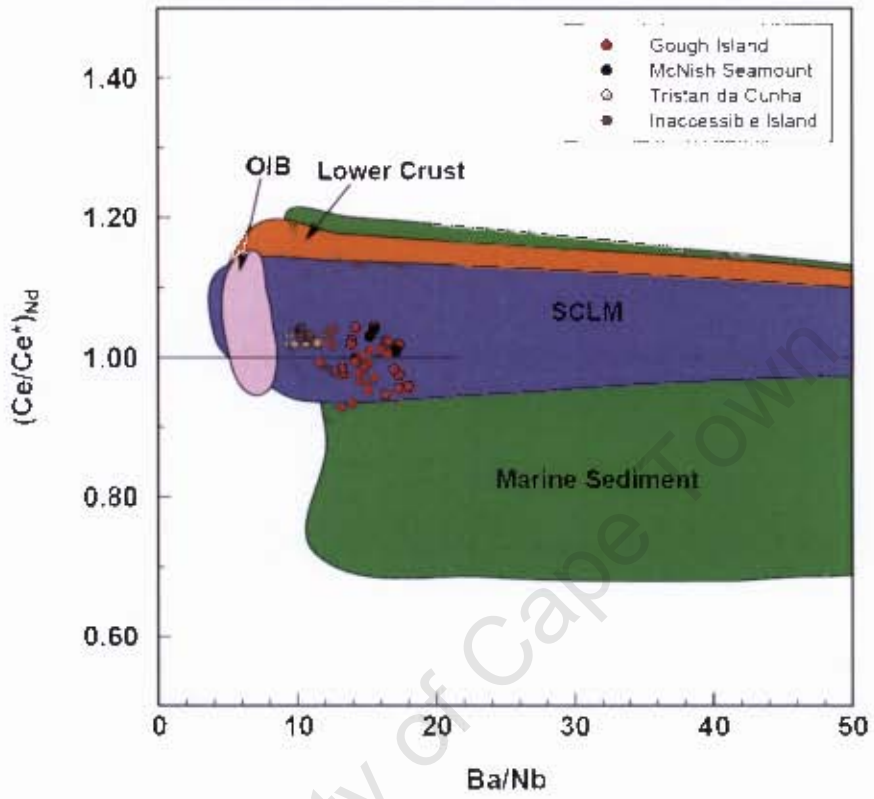

Fig 8-2: Gough Island, McNish Seamount, Inaccessible Island and Tristan da Cunha lavas represented in $(Ce/Ce^*)_{Nd}$ vs. Ba/Nb space superimposed on fields of South African lower crustal xenoliths, mantle xenoliths representing South African SCLM, global modern marine sediments as well as a field representing Marion Island, Bouvet and Ascension Island OIB. Lower crustal xenoliths from Long (2005) and le Roex & Class (unpublished data); SCLM from Gregoire *et al.*, (2003); marine sediments from Plank & Langmuir (1998), Vervoort *et al.*, (1999), McLennan *et al.*, (1990). Tristan da Cunha and Inaccessible Island trace element data from Class & le Roex (unpublished data). References for OIB data listed in the caption for Table 8-1. Normalisation values used in calculation of $(Ce/Ce^*)_{Nd}$ from Sun & McDonough (1989).

Fig 8-2 shows a plot of $(Ce/Ce^*)_{Nd}$ vs. Ba/Nb, with fields representing lower crust, SCLM, modern marine sediment and OIB (defined by Marion Island, Bouvet and Ascension Island) together with data from Tristan da Cunha, Inaccessible Island, Gough Island and the McNish Seamount lavas (references listed in the caption of Fig 8-2). Marine sediments exhibit both positive and large negative Ce-anomalies whereas SCLM and lower crust tend towards slightly positive Ce-anomalies. All three of these components exhibit high Ba/Nb ratios and therefore form horizontal fields in Fig 8-2, with only the marine sediment field stretching down into the negative Ce-anomaly region. OIB exhibit a restricted range in Ba/Nb ratios, but show variable Ce-anomalies and therefore form a vertical field in $(Ce/Ce^*)_{Nd}$ vs. Ba/Nb space, stretching from positive to small negative Ce-anomalies. The magnitude of the positive Ce-anomalies exhibited by the OIB, which define this field, is considered high and is attributed to a lack of available high precision trace element data for these islands. The Gough Island

lavas are displaced to the right of the OIB field (high Ba/Nb ratios) and form a field stretching from the positive to negative Ce-anomaly regions. Tristan da Cunha and Inaccessible Island arrays do not exhibit negative $(Ce/Ce^*)_{Na}$ anomalies and therefore plot towards the low Ba/Nb and high $(Ce/Ce^*)_{Nd}$ end of the Gough Island array.

8.3.2 Ba/Nb Ratios

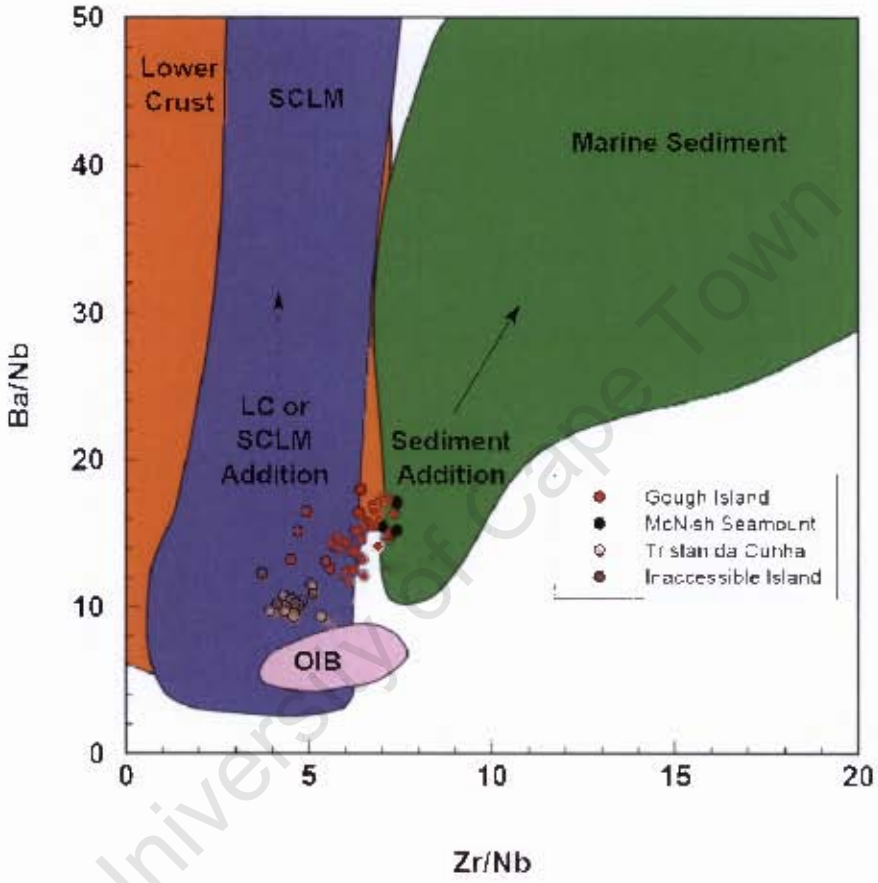

Fig 8-3: Gough Island and the McNish Seamount lavas represented in Ba/Nb vs. Zr/Nb space superimposed on fields of South African lower crustal xenoliths, mantle xenoliths representing South African SCLM and global modern marine sediments. Tristan da Cunha, Inaccessible Island and a field representing Marion Island, Bouvet and Ascension Island OIB are shown for comparison. Lower crustal xenoliths from Long (2005) and le Roex & Class (unpublished data); SCLM from Gregoire *et al.* (2003); marine sediments from Plank & Langmuir (1998), Vervoort *et al.*, (1999), McLennan *et al.*, (1990); Tristan da Cunha and Inaccessible Island trace element data from Class & le Roex (unpublished data). References for OIB data listed in the caption for Table 8-1.

Fig 8-3 shows a plot of Ba/Nb vs. Zr/Nb with fields of lower crust, SCLM and marine sediment relative to Gough Island, the McNish Seamount, Tristan da Cunha and Inaccessible Island as well as a field representing Bouvet, Ascension Island and Marion Island OIB. SCLM, lower crust and marine sediments all exhibit variable, but generally high Ba/Nb ratios, where the Ba/Nb ratios are highest for the lower crust, followed by the marine sediments and SCLM which exhibit the lowest Ba/Nb ratios. Marine sediments exhibit high Zr/Nb ratios in comparison to SCLM and lower crust, which exhibit the lowest Zr/Nb ratios. Therefore, SCLM, lower crust and marine sediments form vertical fields in

Ba/Nb vs. Zr/Nb space. Marion Island, Ascension Island and Bouvet Island OIB form a field in Ba/Nb vs. Zr/Nb space where Ba/Nb and Zr/Nb ratios are less than 10.

The Tristan da Cunha and Inaccessible Island arrays plot towards lower Zr/Nb and Ba/Nb ratios in comparison to the Gough Island and McNish Seamount array, although all of these islands exhibit higher Ba/Nb ratios in comparison to other OIB.

Partial melting processes in the mantle are able to fractionate Zr/Nb ratios because of the difference in bulk partition coefficients of Zr and Nb. Zr is more compatible than Nb during partial melting processes ($^{Zr}D_{grnt}$=0.27; $^{Nb}D_{grnt}$=0.004; $^{Zr}D_{cpx}$=0.128; $^{Nb}D_{cpx}$=0.007; partition coefficients are listed in Table 7-1 and start modes listed in Table 7-3; references are listed in the caption of respective tables). These bulk partition coefficients indicate that partial melting processes result in a decrease of the Zr/Nb ratio. Therefore the lower Zr/Nb ratios of the Tristan da Cunha and Inaccessible Island lavas may, in part, be a partial melting effect.

Ba/Nb ratios are also able to fractionate during partial melting processes if amphibole or ilmenite is present in the mantle source region and exist as residual phases after melting. Ba is more compatible than Nb in amphibole ($^{Ba}D_{amph}$=6.40 and $^{Nb}D_{amph}$=0.80 (McKenzie & O'Nions, 1991, Villemant *et al.*, 1981) whereas Nb is more compatible than Ba in ilmenite ($^{Ba}D_{ilm}$=0.0003 and $^{Nb}D_{ilm}$=2.00 (Zack & Brumm, 1998)). Therefore, if residual amphibole or ilmenite is present in the source after melting, the resulting melt will exhibit negative Ba and Nb anomalies, respectively. However, the Gough Island lavas exhibit a positive Ba anomaly and no anomaly over Nb (Fig 5-6). This indicates that neither residual amphibole nor ilmenite is present in the Gough Island mantle source region.

8.3.3 $^{176}Hf/^{177}Hf$, $^{143}Nd/^{144}Nd$ and $^{87}Sr/^{86}Sr$ Isotope Ratios

Modern marine sediments exhibit enriched (relative to PM) $^{176}Hf/^{177}Hf$, $^{143}Nd/^{144}Nd$ and $^{87}Sr/^{86}Sr$ isotope ratios, and therefore form a field which plots mainly in the enriched quadrant, but stretches to the depleted quadrant, in $^{176}Hf/^{177}Hf$ vs. $^{143}Nd/^{144}Nd$ isotope space (Fig 8-4). OIB (in general, but particularly Bouvet, Ascension Island and Marion Island) exhibit more depleted (relative to PM) $^{176}Hf/^{177}Hf$, $^{143}Nd/^{144}Nd$ and $^{87}Sr/^{86}Sr$ isotope ratios and therefore form a field which plots in the depleted quadrant in Hf-Nd-Sr isotope space. As discussed in Chapter 6, the Gough Island and the McNish Seamount lavas form an array which plots in the enriched quadrant in Hf-Nd-Sr isotope space. Tristan da Cunha straddles the referenced line and the Inaccessible Island array parallels the referenced line.

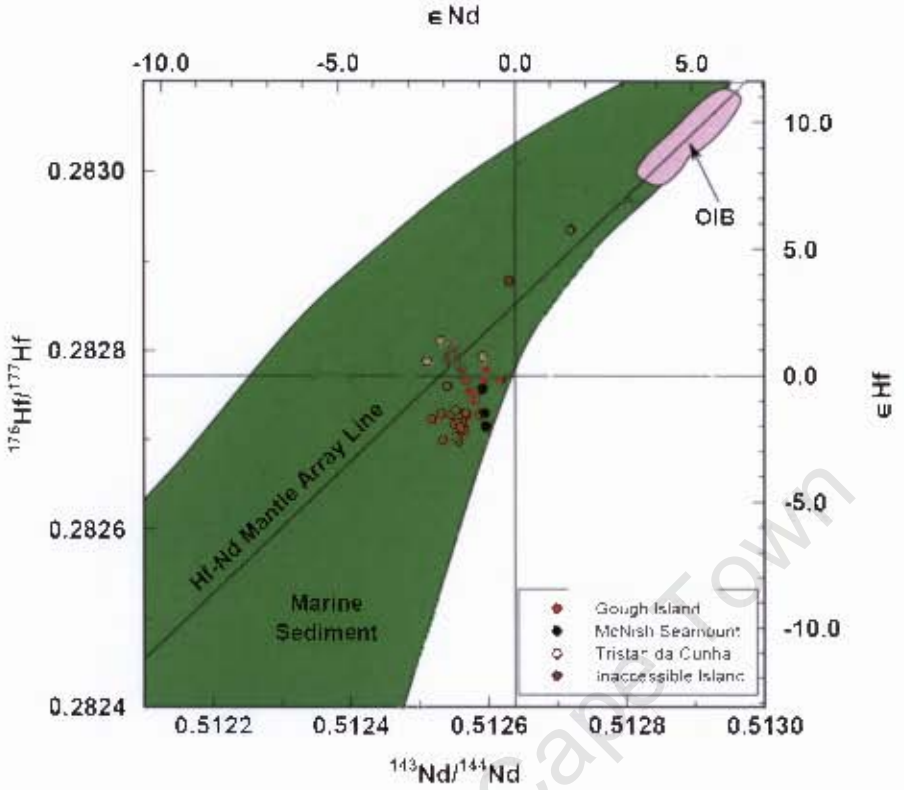

Fig 8-4: Gough Island and the McNish Seamount lavas represented in $^{176}Hf/^{177}Hf$ vs. $^{143}Nd/^{144}Nd$ isotope space superimposed on fields representing global modern marine sediments as well as Bouvet, Ascension Island and Marion Island OIB. Marine sediment isotope data from Plank & Langmuir (1998) and Vervoort *et al.*, (1999). $^{176}Hf/^{177}Hf$ isotope data for the subducting sediment columns from Plank & Langmuir (1998) were calculated using the Hf-Nd crustal array line (εHf= 1.34εNd+2.82) from Vervoort *et al.*, (1999). εHf calculated using $(^{176}Hf/^{177}Hf)_{CHUR}$ of 0.282772 (at t=0Ga) and εNd calculated using $(^{143}Nd/^{144}Nd)_{CHUR}$ of 0.512638 (at t=0Ga) (Blichert-Toft & Albarède, 1997). All isotope data reflects present day values. The Hf-Nd mantle array line (εHf=1.33εNd+3.19; shown in Fig) from Vervoort *et al.*, (1999). Tristan da Cunha and Inaccessible Island isotope data from Class *et al.*, (unpublished data). References for OIB data listed in the caption for Table 8-1.

8.4 Binary Mixing Calculations

8.4.1 The Role of Lower Crust

The majority of lower crustal xenoliths exhibit positive to small negative Ce-anomalies as well as a large range of high Ba/Nb ratios, and therefore form a horizontal field in $(Ce/Ce^*)_{Nd}$ vs. Ba/Nb space (Fig 8-5). Binary mixing curves between the average OIB end-member composition and three lower crustal xenolith samples (12133, 25023 and 06043; le Roex & Class (unpublished data)) are shown in order to illustrate the full range of possible binary mixing curves.

The calculated mixing curves indicate that the high Ba/Nb ratios of the Gough Island lavas can be produced by mixing with lower crust, whereas the low $(Ce/Ce^*)_{Nd}$ ratios cannot. Thus, mixing of lower crust with an OIB mantle source region cannot account for the broad trend of the Gough Island compositional spectrum.

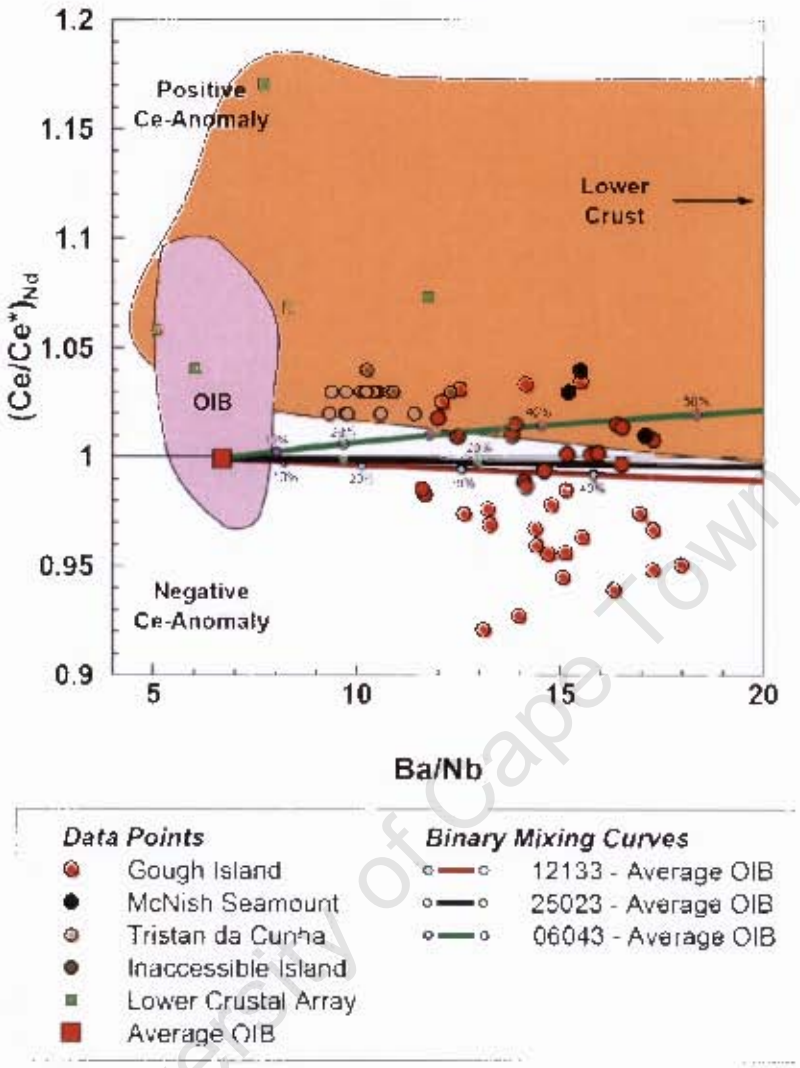

Fig 8-5: Gough Island and the McNish Seamount represented in $(Ce/Ce^*)_{Nd}$ vs. Ba/Nb space superimposed on binary mixing curves between a typical OIB mantle source region end-member composition and select lower crustal xenoliths compositions (12133, 25023, 06043). Samples were chosen to illustrate the full range of possible binary mixing curves. Tristan da Cunha, Inaccessible Island and a field representing Marion Island, Bouvet and Ascension Island OIB are shown for comparison. References listed in the caption for Fig 8-2. Mixing curves shown in 10% increments. Normalisation values used in calculation of $(Ce/Ce^*)_{Nd}$ from Sun & McDonough (1989).

8.4.2 The Role of SCLM

The majority of mantle xenoliths, representing South African SCLM, exhibit a large range of high Ba/Nb ratios as well as positive to small negative Ce-anomalies and therefore form a horizontal field in $(Ce/Ce^*)_{Nd}$ vs. Ba/Nb space (Fig 8-6). Binary mixing curves between the OIB end-member composition and two select mantle xenolith samples (PR89-1 and PR90-57; Gregoire *et al.*, (2003)) were calculated in order to illustrate the full compositional range of SCLM.

The calculated binary mixing curves between SCLM and an OIB mantle source region indicate that the high Ba/Nb ratios of the Gough Island lavas can be reproduced, however the low

$(Ce/Ce^*)_{Nd}$ ratios cannot. Therefore mixing of SCLM with an OIB mantle source region cannot account for the broad trend of the Gough Island compositional spectrum.

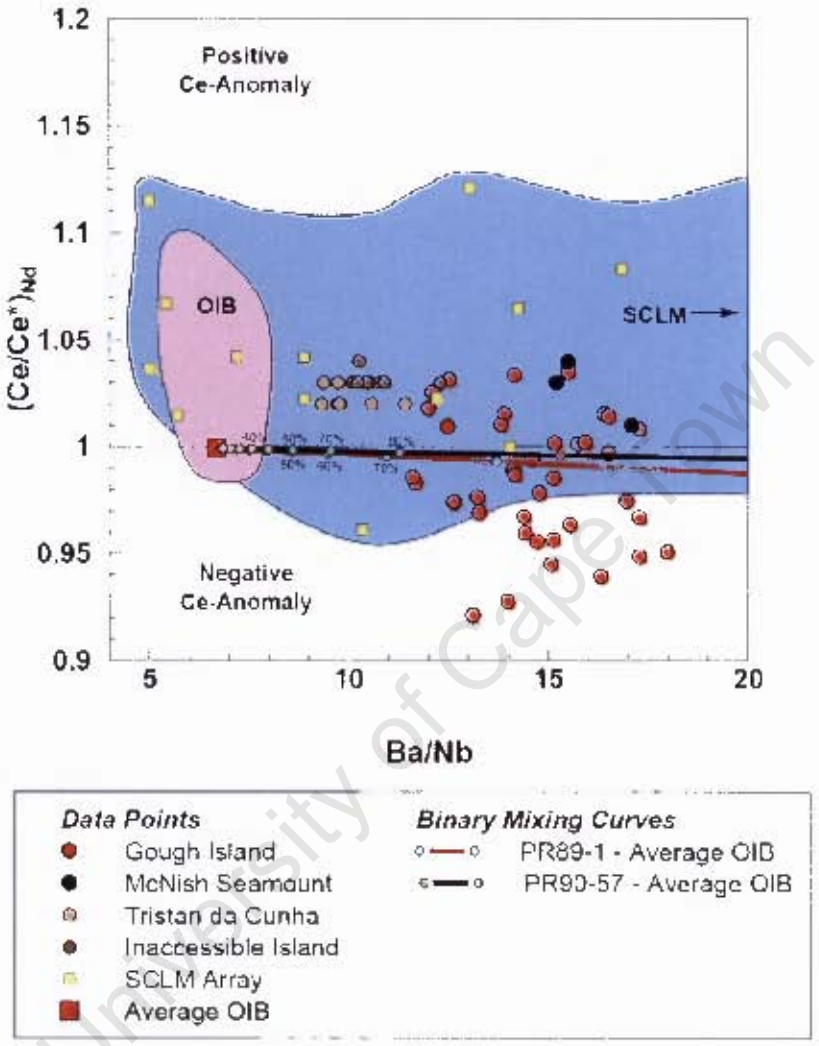

Fig 8-6: Gough Island and the McNish Seamount represented in $(Ce/Ce^*)_{Nd}$ vs. Ba/Nb space superimposed on binary mixing curves between a typical OIB mantle source region end-member composition and various mantle xenolith compositions (PR89-1 and PR90-57) representing South African SCLM. Samples were chosen to illustrate the full range of possible binary mixing curves. Tristan da Cunha, Inaccessible Island and a field representing Marion Island, Bouvet and Ascension Island OIB are shown for comparison. References listed in the caption for Fig 8-2. Mixing curves shown in 10% increments. Normalisation values used in calculation of $(Ce/Ce^*)_{Nd}$ from Sun & McDonough (1989).

8.4.3 The Role of Sediment

The mixing event of marine sediment and the OIB mantle source region would have occurred some time in the past and therefore the isotope composition of the these two components would have been different to present day values. The isotope composition of a resulting mixture would evolve forward in time to present day. Therefore, isotope modelling of this nature should take the isotope evolution paths of these components into account. However, given all of the uncertainties and lack of

constraints particularly in estimating the isotope composition of ancient subducted sediment (Chauvel *et al.*, 2008), the presented models which involve isotope ratios are modelled assuming present day values.

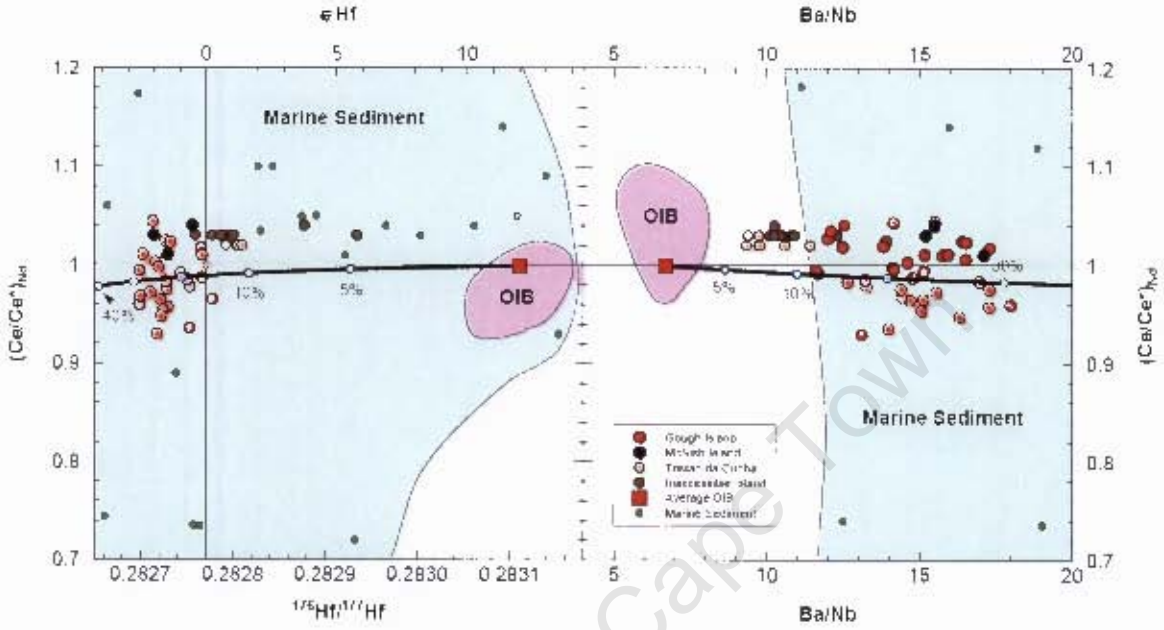

Fig 8-7: Gough Island and the McNish Seamount represented in $(Ce/Ce^*)_{Nd}$ vs. $^{176}Hf/^{177}Hf$ and Ba/Nb space, superimposed on binary mixing curves between an OIB mantle source region composition and marine sediment. Tristan da Cunha and Inaccessible Island as well as a field representing Bouvet, Marion Island and Ascension Island OIB are shown for comparison. All OIB and sediment data reflect present day isotope compositions. References as listed in the caption for Fig 8-2 and Fig 8-4. Normalisation values used in calculation of $(Ce/Ce^*)_{Nd}$ from Sun & McDonough (1989).

The binary mixing curves were calculated between suitable modern marine sediment and OIB mantle source region end-member compositions. Since the OIB array (defined by Marion Island, Bouvet and Ascension Island OIB) as well as the modern marine sediment array exhibits variation in trace element and isotope compositions, the composition of these end-member components were chosen so that the calculated binary mixing curves intersect the Gough Island array at similar mixing proportions. This required adjusting the Zr concentration of the average OIB end-member (Table 8-1) from 29.9ppm to 26.0ppm. Both components plot within their respective fields and therefore exhibit similar trace element and isotope compositions as other marine sediments as well as the Bouvet, Marion Island and Ascension Island OIB.

All of the calculated binary mixing curves intersect the Gough Island array between ~10-30% mixing of the marine sediment with the OIB mantle source region component (Fig 8-7 and Fig 8-8), although the mixing curves intersect the Gough Island array between ~20-30% mixing in Hf-Nd-Sr isotope space (Fig 8-9). These mixing curves indicate that mixing of marine sediment with a typical OIB mantle source region composition is able to effectively account for the Ba/Nb, Zr/Nb and $(Ce/Ce^*)_{Nd}$ as well as Hf-Nd-Sr isotope geochemistry of the Gough Island and the McNish Seamount lavas.

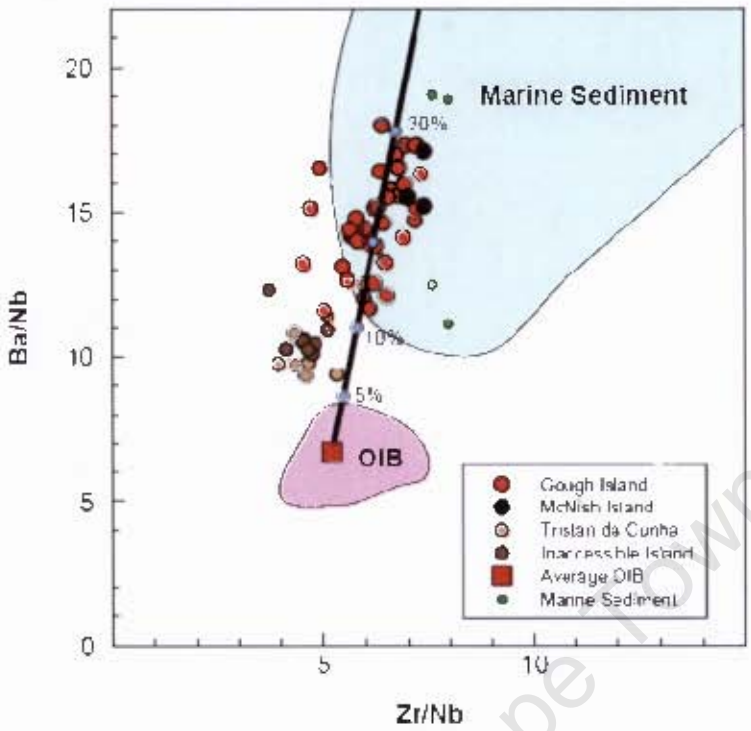

Fig 8-8: Gough Island and the McNish Seamount represented in Ba/Nb vs. Zr/Nb space superimposed on a binary mixing curve between an OIB mantle source region composition and marine sediment. Tristan da Cunha and Inaccessible Island as well as fields representing global modern marine sediments as well as Bouvet, Marion Island and Inaccessible Island OIB are shown for comparison. References as listed in the caption for Fig 8-3

Class & le Roex (2008) showed that the addition of bulk sediment to the Gough Island lavas is unable to account for the low $(Ce/Ce^*)_{Nd}$ ratios of the Gough Island lavas. However, they argue this could indicate decoupling of trace element concentrations and $\delta^{18}O$ ratios, which could occur either by equilibration of oxygen isotopes with mantle oxygen or by the metasomatism of the Gough Island mantle source region with sediment melt. Regardless of the mechanism, Class & le Roex (2008) argue that ~0.5-1% addition of sediment melt (F=25%) is able to effectively account for the range in trace element, isotope and $(Ce/Ce^*)_{Nd}$ signature shown by the Gough Island lavas. This proportion of recycled sediment is significantly lower than indicated by the presented models. However, the presented models differ from those of Class & le Roex (2008) in two aspects:

Firstly, the presented models assume that partial melting of the recycled sediment did not occur prior to mixing (i.e. mixing of a bulk sediment composition occurred). The mixing of a sediment melt with a mantle source region composition would lower the proportions required to explain the trace element characteristics of the Gough Island lavas. This is because the composition of a sediment melt differs to the composition of the bulk sediment because compatible trace elements remain in the residue whereas incompatible trace elements are concentrated in the melt.

Secondly, the starting mantle source region composition was of a typical OIB composition defined by Marion Island, Bouvet and Ascension Island OIB, whereas the source region composition used by Class & le Roex (2008) is calculated by 5% partial melting which gives rise to the Gough Island lavas. Therefore, the proportions required to explain the geochemistry the Gough Island lavas, in the presented models, are larger than the proportions indicated by Class & le Roex (2008).

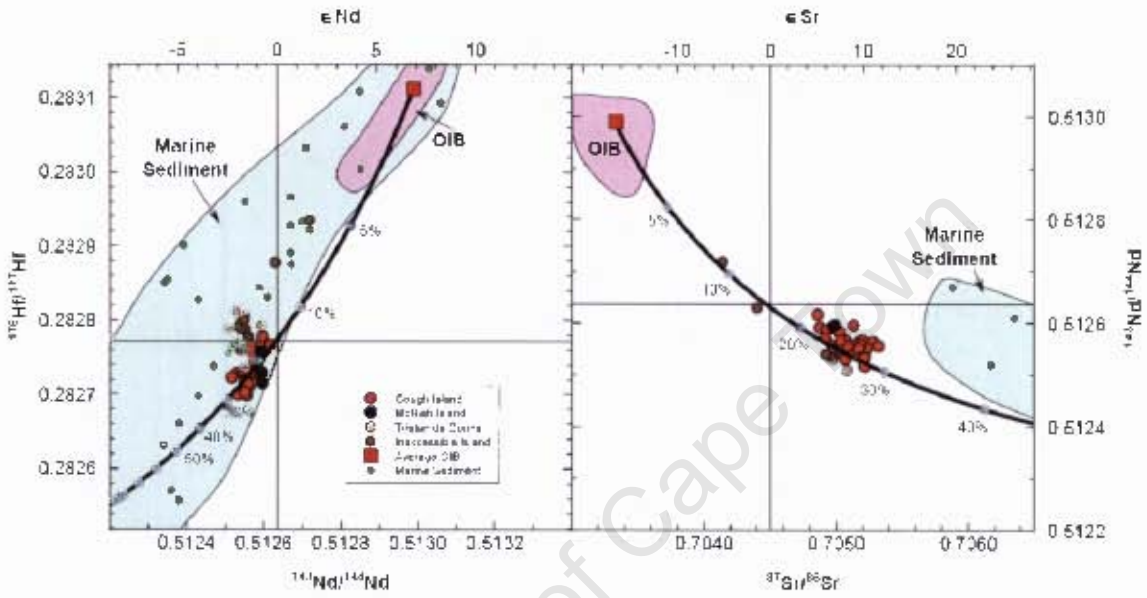

Fig 8-9: Gough Island and the McNish Seamount represented in Hf-Nd-Sr isotope space superimposed on binary mixing curves between an OIB mantle source region composition and marine sediment. Tristan da Cunha and Inaccessible Island as well as fields representing global modern marine sediments as well as Bouvet, Marion Island and Inaccessible Island OIB are shown for comparison. All OIB and marine sediment data reflects present day values. References as listed in the caption for Fig 8-4. εHf calculated using $(^{176}Hf/^{177}Hf)_{CHUR}$ of 0.282772 (at t=0Ga), εNd calculated using $(^{143}Nd/^{144}Nd)_{CHUR}$ of 0.512638 (at t=0Ga) (Blichert-Toft & Albarède, 1997) and εSr calculated using $(^{87}Sr/^{86}Sr)_{CHUR}$ of 0.7045 (at t=0Ga).

8.5 Summary

The high Ba/Nb ratios characteristic of the Gough Island lavas can be accounted for by binary mixing between a typical OIB mantle source region composition and lower crust or SCLM. However, such material is not able to account for the negative Ce-anomalies. This is because SCLM and lower crust exhibit $(Ce/Ce^*)_{Nd}$ ratios which are too high. Therefore, it is argued that the Gough Island lavas do not exhibit a SCLM or lower crust signature.

OIB mantle source region and marine sediment components were chosen in order to produce a calculated binary mixing curve that intersects the Gough Island array, where the chosen components are typical OIB (defined by Marion Island, Bouvet and Ascension Island OIB) and marine sediment compositions. The resulting binary mixing curves indicate that the Gough Island and McNish Seamount arrays can be produced by the addition of ~10-30% bulk modern marine sediment with a typical OIB mantle source region. Class & le Roex (2008) argue that these proportions indicate decoupling of $\delta^{18}O$ and trace element ratios. However, they also indicate that the addition of a sediment melt to a starting mantle source region composition is able to account for the $\delta^{18}O$, trace

element and $(Ce/Ce^*)_{Nd}$ ratio of these lavas. The addition of a sediment melt would also decrease the proportions of sediment required to account for the production of these lavas.

In Chapter 6 it was shown that the Gough Island lavas exhibit low $^{176}Hf/^{177}Hf$ isotope ratios in comparison to other OIB and this array in Hf-Nd isotope space plots below the Hf-Nd mantle array line, indicating decoupling between these two isotope systems. This can be explained by the Zircon Effect (Chapter 6) which indicates that the Gough Island lavas formed from a mantle source region which had previously interacted with a recycled zircon-rich, pelagic sediment. This observation substantiates the models presented in this chapter and therefore it is concluded that the Gough Island lavas are derived fro a source more typical of South Atlantic OIB, but with a significant, recycled marine sediment component.

9 Summary and Conclusions

9.1 Overview

Basalts from Gough Island and the McNish Seamount were selected for a detailed geochemical study using major element, high precision trace element, $^{143}Nd/^{144}Nd$ and $^{87}Sr/^{86}Sr$ and newly acquired $^{176}Hf/^{177}Hf$ isotope data. The geochemical data for the Gough Island lavas is subsequently used determine the petrogenesis of these lavas and the evolution of the underlying mantle source region.

9.2 Petrography

The Gough Island lavas consist of picrite basalts, olivine basalts, trachybasalts, trachytes and aegirine-augite trachytes (le Maitre, 1962). le Roex (1985) recognised, based on petrography, that three different varieties of olivine basalts exist in this suite of lavas - the coarsely pyroxene-olivine phyric basalts, moderately pyroxene-olivine phyric basalts and aphyric to finely porphyritic basalts.

The sample set used in this study consists of thirty-nine lavas (10 Lower Basalts, 27 Middle Basalts and 1 Upper Basalt) which include basalts, trachybasalts and trachyandesites. These lavas all range from aphyric through finely to coarsely porphyritic. Two distinct petrographic groups exist in the Lower and Middle Basalt series, where the first group consists of anhedral to euhedral olivine phenocrysts and anhedral to subhedral clinopyroxene as the major and minor phenocrysts phases, respectively. The second group consists of anhedral to subhedral clinopyroxene and subhedral olivine as the major and minor phenocryst phases, respectively. The single Upper Basalt sample is a basaltic trachyandesite and contains anhedral to euhedral olivine and plagioclase as the major and minor phenocryst phases, respectively. All lavas exhibit an intergranular texture with a matrix assemblage of olivine, plagioclase, clinopyroxene, titanomagnetite, ilmenite and apatite. Vesicles as well as cumulocrysts and glomercrysts are present in some of the lavas. Eleven lavas are petrographically fresh, whereas the remainder of the samples exhibit evidence for hydrothermal alteration and development of indingsite and/or bowlingsite after olivine.

9.3 Bulk Rock Geochemistry

The Gough Island lavas consist of basalts, trachybasalts and basaltic trachyandesites and therefore form an alkali basalt – trachyte series on a TAS diagram (even though trachytes do not form part of the dataset used in this study). Both the Lower and Middle Basalts range from basalt to basaltic trachyandesite whereas the single Upper Basalt sample plots within the basaltic trachyandesite field on a TAS diagram and therefore is the most evolved sample in this dataset.

SiO_2, K_2O and Al_2O_3 all exhibit a negative correlation with Mg#, whereas CaO exhibits a scattered positive correlation with Mg#. Clinopyroxene appears to have been an important fractionation phase during magma differentiation (indicated by the positive gradient in CaO vs. Mg#

space), whereas plagioclase and apatite were not important fractionating phases as indicated by the negative gradients in variation diagrams of Al_2O_3, Na_2O and P_2O_5 vs. Mg#. TiO_2 exhibits a tight, negative correlation with Mg# greater than 54 and a scattered positive correlation with lower Mg#, indicating the importance of fractionating Fe-Ti oxides with increasing differentiation.

The Lower, Middle and Upper Basalts all exhibit similar incompatible, moderately incompatible and compatible trace element concentrations and therefore these arrays are superimposed on all trace element variation diagrams. The incompatible trace element concentrations of Ba, Ta, Nb and Rb are high, and Ba, Rb and especially Ta exhibit a strong positive correlation with Nb and Zr. The Ba/Nb ratios of these lavas is high (11.6-18.0) whereas the Zr/Nb and La/Nb ratios are moderate and range from 4.51-7.32 and 0.84-1.18, respectively.

The moderately incompatible trace element concentrations of Hf, Y, Ce and Sr are high in absolute abundance and exhibit a large range. Sr and Y exhibit broad positive correlations with Zr which breaks down at Zr abundances greater than ~300ppm, whereas Ce and Hf exhibit strong positive correlations with Zr for the entire range of Zr concentrations. The Zr/Hf, Y/Nb and Ce/Pb ratios for Gough Island range from 44.5-54.0, 0.28-0.82 and 18.5-34.0, respectively, whereas the $(La/Sm)_N$ and $(La/Yb)_N$ ratios range from 2.55-5.08 and 11.8-30.5, respectively (values normalised to chondrite (Sun & McDonough, 1989)).

The compatible ferro-magnesian trace elements Co, Ni and Cr exhibit a large range in concentrations and the array forms a positive gradient with Mg#. This indicates the importance of the continuous fractionation of ferro-magnesian minerals (e.g. olivine and clinopyroxene) during magma differentiation.

Primitive mantle normalised trace element patterns for the Gough Island lavas are generally sub-parallel with positive Ba and Pb as well as negative Th, U and Zr anomalies. The chondrite normalised REE patterns are generally sub-parallel and LREE enriched relative to HREE. Crossing patterns towards the MREE (especially Dy) are observed and form as the result of slight gradient variations between samples.

The three analysed McNish Seamount samples (AG51-7-1, AG51-7-2 and AG51-7-3) all exhibit similar major and trace element geochemistry and therefore are thought to represent three samples from the same lava flow. These three samples also exhibit similar major and trace element geochemistry in comparison to the Gough Island lavas, and therefore plots within the Gough Island array in the TAS diagram and all the major and trace element variation diagrams. Similar to the Gough Island lavas the Ba/Nb trace element ratio ranges from 15.2-17.1 whereas the Zr/Nb and La/Nb ratios are moderate and the Ce/Pb, $(La/Sm)_N$ and $(La/Yb)_N$ ratios range from 20.7-23.7, 3.00-3.03 and 16.6-17.3, respectively.

The McNish Seamount primitive mantle normalised trace element patterns and chondrite normalised REE patterns are identical to the majority of the Gough Island trace element diagrams. Therefore, the McNish Seamount trace element and REE patterns are all sub-parallel and exhibit similar abundances as the Gough Island lavas. They also exhibit positive Ba and Pb and negative Th, U and Zr anomalies and the REE patterns are LREE enriched relative to the MREE and HREE. Therefore, it is argued that the McNish Seamount lavas form part of the same igneous province as the Gough Island lavas.

9.4 Isotope Geochemistry

The Gough Island and McNish lavas exhibit $^{176}Hf/^{177}Hf$ isotope ratios which range from 0.282699-0.282778, and therefore are enriched relative to PM. The single Upper Basalt sample was not analysed for $^{176}Hf/^{177}Hf$, but the Lower and Middle Basalts range in $^{176}Hf/^{177}Hf$ isotope ratios from 0.282699 to 0.282778 and 0.282703 to 0.282767, respectively. These lavas exhibit $^{143}Nd/^{144}Nd$ and $^{87}Sr/^{86}Sr$ isotope ratios of 0.512517-0.512596 and 0.704859-0.705321, respectively, whereas the McNish lavas range from 0.512591-0.512596 and 0.704977-0.704992, respectively (Class & le Roex, unpublished data). As a result, the Gough Island lavas and the McNish Seamount lavas form arrays which plot within the enriched (relative to PM) quadrant in Hf-Nd-Sr isotope space. These arrays also plot sub-parallel to, but below the Hf-Nd mantle array line ($\varepsilon Hf=1.33\varepsilon Nd+3.19$ (Vervoort *et al.*, 1999)) with $\Delta\varepsilon Hf$ ranging from 1.5 to 3.4 for Gough Island lavas and 2.5 to 4.1 for the McNish Seamount.

The Gough Island lavas also exhibit $^{176}Hf/^{177}Hf$, $^{143}Nd/^{144}Nd$ and $^{87}Sr/^{86}Sr$ isotope ratios similar to the Tristan da Cunha and Inaccessible Island suite of lavas. However, the Inaccessible Island lavas plot along the Hf-Nd mantle array line in Hf-Nd isotope space whereas the Tristan da Cunha lavas form a horizontal array intersecting the Hf-Nd mantle array line. The Gough Island and McNish Seamount arrays plot towards the enriched end of the global OIB arrays within the more depleted end of the continental array (Vervoort *et al.*, 1999) in Hf-Nd-Sr isotope space.

Since the Lower and Middle Basalts of the Gough Island lavas, as well as the McNish Seamount lavas, exhibit similar Ba/Nb, Zr/Nb and La/Sm trace element ratios, these arrays are superimposed in a plot of these incompatible trace element ratios vs. $^{176}Hf/^{177}Hf$. However, the Lower Basalts exhibit lower Zr/Hf ratios than the Middle Basalts and therefore these arrays are not superimposed in Zr/Hf vs. $^{176}Hf/^{177}Hf$ isotope space. This suggests that the Gough Island mantle source region is heterogeneous, where the Lower Basalts were generated from a source that exhibits similar Hf isotope ratios as the Middle Basalts but has different Zr and Hf concentrations.

9.5 Petrogenesis of the Gough Island Suite of Lavas

In order to evaluate a mantle source region composition and partial melting models, ten Gough Island primary magma compositions were calculated by correcting for crystal fractionation processes.

The primary magma trace element compositions were calculated by adding clinopyroxene and equilibrium olivine back into the primitive lava composition (in equal proportions) in 1% increments until an Mg# of 69 was reached. This required the addition of 14-28% addition of olivine and clinopyroxene. The resulting primary magma chondrite normalised REE patterns are all LREE enriched relative to the HREE and exhibit crossing REE patterns between Tb and Dy as a result of minor gradient variations between patterns.

OIB mantle source regions are traditionally thought to be composed of peridotite as this is the most common rock type in the upper mantle (Jaques & Green, 1980, Kushiro, 1968, Ringwood, 1975, Sun & McDonough, 1995) where moderate degrees of partial melting (<15%) results in the formation of alkali basalts (Jaques & Green, 1980, Kushiro, 1968). However, recently it has been argued that pyroxenite and eclogite may be present in the source regions of some OIB (Sobolev *et al.*, 2007, Sobolev *et al.*, 2005), where partial melts of a silica-deficient garnet pyroxenite between 2.5-5.0GPa are able to produce similar major element compositions to ocean island alkali basalts (Hirschmann *et al.*, 2003, Kogiso *et al.*, 2003).

Constrained forward modelling of REE was used to determine whether the Gough Island primary magmas were produced from a peridotite (spinel or garnet lherzolite) or a garnet pyroxenite mantle source region as well as to determine the required melting conditions.

The models indicate that the trace element geochemistry of the Gough Island lavas cannot be explained by the partial melting of a spinel lherzolite mantle source region, but can be explained by the partial melting of a garnet lherzolite or a garnet pyroxenite mantle source region. The calculated REE patterns for these two source regions are able to explain the overall REE geochemistry of the Gough Island primary magmas as well as the crossing REE patterns at Dy. Therefore, constrained forward modelling indicates that the Gough Island lavas formed by either 5-8% equilibrium melting of a garnet lherzolite or ~30-50% equilibrium melting of a garnet pyroxenite mantle source region.

9.6 Evolution of the Gough Island Mantle Source Region

Numerous studies of OIB from around the world have argued that the enriched trace element and isotope compositions of OIB require involvement of a lithospheric component. Since the geochemistry of the Gough Island is unique (high Ba/Nb, large negative Ce anomaly and enriched Hf-Nd-Sr isotope ratios), a better understanding of the interaction of OIB mantle source regions with a recycled lithospheric component can be gained by studying these lavas. All previous studies of these lavas have recognised the need for a recycled lithospheric component to account for their unique geochemistry (Class & le Roex, 2008, le Roex, 1985, Willbold & Stracke, 2006). Thus, in order to evaluate the evolution of the Gough Island mantle source region, binary mixing curves were calculated between an OIB mantle source region composition and SCLM, lower crust and marine sediment compositions in $^{176}Hf/^{177}Hf$-$^{143}Nd/^{144}Nd$-$^{87}Sr/^{86}Sr$-Ba/Nb-Zr/Nb-$(Ce/Ce^*)_{Nd}$ space.

Binary mixing curves using $(Ce/Ce^*)_{Nd}$ between a typical OIB mantle source region component (defined by Marion Island, Bouvet and Ascension Island OIB) and SCLM as well as lower crust indicates that the Gough Island lavas do not exhibit either SCLM or lower crust signatures, as these component exhibit Ce-anomalies which are too high. However, the calculated binary mixing curves indicate that the $^{176}Hf/^{177}Hf$, $^{143}Nd/^{144}Nd$, $^{87}Sr/^{86}Sr$, $(Ce/Ce^*)_{Nd}$, Zr/Nb and Ba/Nb ratios are able to be satisfactorily explained by the addition of ~10-30% recycled marine sediment to a typical OIB mantle source region composition. Thus, the Gough Island lavas are derived from a source more typical of South Atlantic OIB, but with a significant recycled marine sediment component.

10 References

Andres, M., Blichert-Toft, J. & Schilling, J. G. (2002) Hafnium isotopes in basalts from the southern Mid-Atlantic Ridge from 40 S to 55 S: Discovery and Shona plume-ridge interactions and the role of recycled sediments. *Geochemistry, Geophysics, Geosystems,* 3, 1.

Beattie, P. (1993) The effect of partial melting of spinel peridotite on uranium series disequilibria: constraints from partitioning studies. *Earth and Planetary Science Letters,* 177, 379-391.

Ben Othman, D., White, W. M. & Patchett, J. (1989) The geochemistry of marine sediments, island arc magma genesis, and crust-mantle recycling. *Earth and Planetary Science Letters,* 94, 1-21.

Blichert-Toft, J. (2001) On the Lu–Hf isotope geochemistry of silicate rocks. *Geostandards Newsletter,* 25, 41–56.

Blichert-Toft, J. & Albarède, F. (1997) The Lu-Hf isotope geochemistry of chondrites and the evolution of the mantle-crust system. *Earth and Planetary Science Letters,* 148, 243-258.

Blichert-Toft, J., Chauvel, C. & Albarède, F. (1997) Separation of Hf and Lu for high-precision isotope analysis of rock samples by magnetic sector-multiple collector ICP-MS. *Contributions to Mineralogy and Petrology,* 127, 248-260.

Blichert-Toft, J., Frey, F. A. & Albarede, F. (1999) Hf isotope evidence for pelagic sediments in the source of Hawaiian basalts. *Science,* 285, 879-882.

Blichert-Toft, J. & White, W. M. (2001) Hf isotope geochemistry of the Galápagos Islands. *Geochemistry, Geophysics, Geosystems,* 2.

Bougault, H. & Hekinian, R. (1974) Rift valley in the Atlantic Ocean near 36 degrees 50'N; petrology and geochemistry of basalt rocks. *Earth and Planetary Science Letters,* 24, 249-261.

Boyd, F. R. & England, J. L. (1960) Apparatus for phase equilibrium studies at pressures up to 50kbars and temperatures up to 1750°C. *Journal of Geophysical Research,* 65, 741-748.

Carroll, P. (2003) The South Atlantic & Subantarctic Islands. http://www.btinternet.com/~sa_sa/gough_island/gough_island.html Last Accessed on February, 2007

Chauvel, C., Hofmann, A. W. & Vidal, P. (1992) HIMU-EM: The French Polynesian connection. *Earth and Planetary Science Letters,* 110, 99-119.

Chauvel, C., Lewin, E., Carpentier, M., Arndt, N. T. & Marini, J.-C. (2008) Role of recylced oceanic basalt and sediment in generating the Hf-Nd mantle array. *Nature,* 1, 64-67.

Class, C., Altherr, R., Volker, F., Eberz, G. & Mcculloch, M. T. (1994) Geochemistry of Pliocene to Quaternary alkali basalts from the Huri Hills, northern Kenya. *Chemical Geology,* 113, 1-22.

Class, C. & Le Roex, A. P. (2006) Continental material in the shallow oceanic mantle-How does it get there? *Geology,* 34, 129-132.

Class, C. & Le Roex, A. P. (2008) Ce anomalies in Gough Island lavas - Trace element characteristics of a recycled sediment component. *Earth and Planetary Science Letters,* 265, 475-486.

Cronan, D. S. & Hodkinson, R. A. (1997) Geochemistry of hydrothermal sediments from ODP sites 834 and 835 in the Lau Basin, southwest Pacific. *Marine Geology,* 141, 237-268.

Davis, M. G., Garcia, M. O. & Wallace, P. (2003) Volatiles in glasses from Mauna Loa Volcano, Hawai'i: implications for magma degassing and contamination, and growth of Hawaiian volcanoes. *Contributions To Mineralogy And Petrology,* 114, 570-591.

Dickin, A. P. (1995) *Radiogenic Isotope Geology,* Cambridge, Cambridge University Press.

Donnelly, K. E., Goldstein, S. L., Langmuir, C. H. & Spiegelman, M. (2004) Origin of enriched ocean ridge basalts and implications for mantle dynamics. *Earth And Planetary Science Letters,* 226, 347-366.

Eisele, J., Sharma, M., Galer, S. J. G., Blichert-Toft, J., Devey, C. W. & Hofmann, A. W. (2002) The role of sediment recycling in EM-1 inferred from OS, Pb, Hf, Nd, Sr isotope and trace element systematics of the Pitcairn hotspot. *Earth and Planetary Science Letters,* 196, 197-212.

Elderfield, H. & Greaves, M. J. (1982) The rare earth elements in seawater. *Nature,* 296, 214-219.

Elderfield, H., Hawkesworth, C. J., Greaves, M. J. & Calvert, S. E. (1981) Rare earth element geochemistry of oceanic ferromanganese nodules and associated sediment. *Geochimica Et Cosmochimica Acta,* 45, 513-528.

Feigenson, M. D., Patino, L. C. & Carr, M. J. (1996) Constraints on partial melting imposed by rare earth element variations in Mauna Kea basalts. *Journal of Geophysical Research,* 101, 11815-11829.

Foley, S. F., Barth, M. G. & Jenner, G. A. (2000) Rutile/melt partition coefficients for trace elements and an assessment of the influence of rutile on the trace element characteristics of subduction zone magmas. *Geochimica Et Cosmochimica Acta,* 64, 933-938.

Frey, F. A. & Rhodes, J. M. (1993) Intershield Geochemical differences among Hawaiian Volcanoes: Implications for Source Compositions, Melting Process and Magma Ascent Paths. *Philosophical Transactions: Physical Sciences and Engineering,* 342, 121-136.

Fujimaki, H. (1986) Partition-Coefficients Of Hf, Zr, And Ree Between Zircon, Apatite, And Liquid. *Contributions To Mineralogy And Petrology,* 94, 42-45.

Gasperini, D., Blichert-Toft, J., Bosch, D., Del Moro, A., Macera, P., Telouk, P. & Albarede, F. (2000) Evidence from Sardinian basalt geochemistry for recycling of plume heads into the Earth's mantle. *Nature,* 408, 701-704.

Gast, P. W. (1968) Trace element fractionation and the origin of tholeiitic and alkaline magma types. *Geochimica Et Cosmochimica Acta,* 32, 1057-1086.

Gast, P. W., Tilton, G. R. & Hedge, C. (1964) Isotopic Composition of Lead and Strontium from Ascension and Gough Islands. *Science,* 145, 1181.

Gibson, S. A., Thompson, R. N., Day, J. A., Humphris, S. E. & Dickin, A. P. (2005) Melt-generation processes associated with the Tristan mantle plume: Constraints on the origin of EM-1. *Earth and Planetary Science Letters,* 237, 744-767.

Green, D. H. & Ringwood, A. E. (1967) The genesis of basaltic magmas. *Contributions To Mineralogy And Petrology,* 15, 103-190.

Gregoire, M., Bell, D. R. & Le Roex, A. P. (2003) Garnet lherzolites from the Kaapvaal Craton (South Africa): trace element evidence for a metasomatic history. *Journal Of Petrology,* 44, 629-657.

Hansteen, T. H. & Troll, V. R. (2003) Oxygen isotope composition of xenoliths from oceanic crust and volcanic edifice beneath Gran Canaria (Canary Islands): consequences for crustal contamination of ascending magmas. *Chemical Geology,* 193, 181-193.

Harris, C., Smith, H. S. & Le Roex, A. P. (2000) Oxygen isotope composition of phenocrysts from Tristan da Cunha and Gough Island lavas: variation with fractional crystallization and evidence for assimilation. *Contributions To Mineralogy And Petrology,* 138, 164-175.

Hart, S. R. (1988) Heterogeneous mantle domains: Signatures, genesis and mixing chronologies. *Earth and Planetary Science Letters,* 90, 273-296.

Hart, S. R. & Davis, K. E. (1978) Nickel partitioning between olivine and silicate melt. *Earth and Planetary Science Letters,* 40, 203-219.

Hart, S. R., Hauri, E. H., Oschmann, L. A. & Whitehead, J. A. (1992) Mantle Plumes and Entrainment: Isotopic Evidence. *Science,* 256, 517.

Hauri, E. H., Wagner, T. P. & Grove, T. L. (1994) Experimental And Natural Partitioning Of Th, U, Pb And Other Trace-Elements Between Garnet, Clinopyroxene And Basaltic Melts. *Chemical Geology,* 117, 149-166.

Herzberg, C. (2006) Petrology and thermal structure of the Hawaiian plume from Mauna Kea volcano. *Nature,* 444, 605-609.

Hirose, K. & Kushiro, I. (1993) Partial melting of dry peridotites at high pressures: determination of compositions of melts segregated from peridotite using aggregates of diamond. *Earth and Planetary Science Letters,* 114, 477-489.

Hirschmann, M. M., Kogiso, T., Baker, M. B. & Stolper, E. M. (2003) Alkalic magmas generated by partial melting of garnet pyroxenite. *Geology,* 31, 481-484.

Hofmann, A. W. (1997) Mantle geochemistry: the message from oceanic volcanism. *Nature,* 385, 219-229.

Hole, M. J., Saunders, A. D., Marriner, G. F. & Tarney, J. (1984) Subduction of pelagic sediment: implications for the origin of Ce-anomalous basalts from the Mariana Islands. *Journal of the Geological Society of London,* 141, 453-472.

Horn, I., Foley, S. F., Jackson, S. E. & Jenner, G. A. (1994) Experimentally Determined Partitioning Of High-Field Strength-Elements And Selected Transition-Elements Between Spinel And Basaltic Melt. *Chemical Geology,* 117, 193-218.

Ito, K. & Kennedy, G. C. (1967) Melting and phase relations in a natural peridotite to 40 kbar. *American Journal of Science,* 265, 519-538.

Janney, P. E. & Le Roex, A. P. (2005) Hafnium Isotope and Trace Element Constraints on the Nature of Mantle Heterogeneity beneath the Central Southwest Indian Ridge (13 {degrees} E to 47 {degrees} E). *Journal of Petrology,* 46, 2427.

Jaques, A. L. & Green, D. H. (1980) Anhydrous melting of peridotite at 0-15 kb pressure and the genesis of tholeiitic basalts. *Contributions To Mineralogy And Petrology,* 73, 287-310.

Johnson, C. M. & Beard, B. L. (1993) Evidence from hafnium isotopes for ancient sub-oceanic mantle beneath the Rio Grande rift. *Nature,* 362, 441-444.

Johnson, K. T. M. (1994) Experimental cpx/ and garnet/melt partitioning of REE and other trace elements at high pressures; petrogenetic implications. *Mineralogical Magazine,* 58, 454-455.

Johnson, K. T. M., Dick, H. J. B. & Shimizu, N. (1990) Melting in the Oceanic Upper Mantle - an Ion Microprobe Study of Diopsides in Abyssal Peridotites. *Journal of Geophysical Research-Solid Earth and Planets,* 95, 2661-2678.

Johnson, K. T. M. & Kushiro, I. (1992) Segregation of high pressure partial melts from peridotite using aggregates of diamond: a new experimental approach. *Geophysical Research Letters,* 19, 1703-1706.

Kelemen, P. B., Dick, H. J. B. & Quick, J. E. (1992) Formation of harzburgite by pervasive melt/rock reaction in the upper mantle. *Nature,* 358, 635-641.

Kelemen, P. B., Yogodzinski, G. & Scholl, D. W. (2003) Along-strike variation in the Aleutian island arc: Genesis of high Mg# andesite and implications for continental crust. IN Eiler, J. (Ed.) *Inside the Subduction Factory, Geophys. Monogr. Ser.* Washington, D.C., AGU.

Kennedy, A. K., Lofgren, G. E. & Wasserburg, G. J. (1993) An Experimental-Study Of Trace-Element Partitioning Between Olivine, Ortho-Pyroxene And Melt In Chondrules - Equilibrium Values And Kinetic Effects. *Earth And Planetary Science Letters,* 115, 177-195.

Keshav, S., Gudfinnsson, G. H., Sen, G. & Fei, Y. (2004) High-pressure melting experiments on garnet clinopyroxenite and the alkalic to tholeiitic transition in ocean-island basalts. *Earth and Planetary Science Letters,* 223, 365-379.

Kinzler, R. J. & Grove, T. L. (1992) Primary magmas of mid-ocean ridge basalts 1. Experiments and Methods. *Journal of Geophysical Research,* 97, 6885-6906.

Klügel, A., Hansteen, T. H. & Galipp, K. (2005) Magma storage and underplating beneath Cumbre Vieja volcano, La Palma (Canary Islands). *Earth and Planetary Science Letters,* 236, 211-226.

Kogiso, T., Hirose, K. & Takahasi, E. (1998) Melting experiments on homogeneous mixtures of peridotite and basalt: application to the genesis of ocean island basalts. *Earth and Planetary Science Letters,* 162, 45-61.

Kogiso, T. & Hirschmann, M. M. (2006) Partial melting experiments of bimineralic eclogite and the role of recylced mafic oceanic crust in the genesis of ocean island basalts. *Earth and Planetary Science Letters,* 249, 188-199.

Kogiso, T., Hirschmann, M. M. & Frost, D. J. (2003) High-pressure partial melting of garnet pyroxenite: possile mafic lithologies in the source of ocean island basalts. *Earth and Planetary Science Letters,* 216, 603-617.

Kurz, M. D., Jenkins, W. J. & Hart, S. R. (1982) Helium-isotopic systematics of oceanic islands and mantle heterogeneity. *Nature,* 297, 43-47.

Kushiro, I. (1968) Compositions of Magmas Formed by Partial Zone Melting of the Earth's Upper Mantle. *Journal of Geophysical Research,* 73, 619-634.

Kushiro, I., Shimizu, N., Nakamura, Y. & Akimoto, S. (1972) Compositions of coexisting liquid and solid phases formed upon melting of natural garnet and spinel lherzolites at high pressures: a preliminary report. *Earth and Planetary Science Letters,* 14, 19-25.

Kushiro, I. & Yoder, H. S. (1966) Anorthite-forsterite and anorthite-enstatite reactions and their bearing on the basalt-eclogite transformation. *Journal Of Petrology,* 7, 337-362.

Langmuir, C. H., Vocke, R. D., Hanson, G. N. & Hart, S. R. (1978) General Mixing Equation With Applications To Icelandic Basalts. *Earth And Planetary Science Letters,* 37, 380-392.

Le Maitre, R. W. (1960) The Geology of Gough Island, South Atlantic. *Overseas Geol. Miner. Resour.,* 7, 371-380.

Le Maitre, R. W. (1962) Petrology of volcanic rocks, Gough island, south Atlantic. *Bulletin of the Geological Society of America,* 73, 1309.

Le Roex, A. P. (1985) Geochemistry, Mineralogy and Magmatic Evolution of the Basaltic and Trachytic Lavas from Gough Island, South Atlantic. *Journal of Petrology,* 26, 149.

Le Roex, A. P. & Erlank, A. J. (1982) Quantitative evaluation of fractional crystallization in Bouvet Island lavas. *Journal of Volcanology and Geothermal Research,* 13, 309–338.

Le Roux, P. J., Le Roex, A. P., Schilling, J. G., Shimizu, N., Perkins, W. W. & Pearce, N. J. G. (2002) Mantle heterogeneity beneath the southern Mid-Atlantic Ridge: trace element evidence for contamination of ambient asthenospheric mantle. *Earth and Planetary Science Letters,* 203, 479-498.

Long, D. J. (2005) The Geothermobarometry of Lower Crustal Xenoliths from the Goedehoop Kimberlite, South Africa. *Department of Geological Sciences.* Cape Town, University of Cape Town (Hons Project).

Lustrino, M. (2005) How the delamination and detachment of lower crust can influence basaltic magmatism. *Earth-Science Reviews,* 72, 21-38.

Maund, J. G., Rex, D. C., Le Roex, A. P. & Reid, D. L. (1988) Volcanism on Gough Island: a revised stratigraphy. *Geological Magazine,* 125, 175-181.

Mckay, G., Le, L., Wagstaff, J. & Crozaz, G. (1994) Experimental Partitioning Of Rare-Earth Elements And Strontium - Constraints On Petrogenesis And Redox Conditions During Crystallization Of Antarctic Angrite Lewis Cliff-86010. *Geochimica Et Cosmochimica Acta,* 58, 2911-2919.

Mckenzie, D. & O'nions, R. K. (1991) Partial Melt Distributions From Inversion Of Rare-Earth Element Concentrations. *Journal Of Petrology,* 32, 1021-1091.

Mckenzie, D. & Onions, R. K. (1995) The Source Regions Of Ocean Island Basalts. *Journal Of Petrology,* 36, 133-159.

Mclennan, S. M., Taylor, S. R., Mcculloch, M. T. & Maynard, J. B. (1990) Geochemical And Nd-Sr Isotopic Composition Of Deep-Sea Turbidites - Crustal Evolution And Plate Tectonic Associations. *Geochimica Et Cosmochimica Acta,* 54, 2015-2050.

Miller, J. A. (1964) Age determinations made on samples from the Tristan da Cunha group and other parts of the mid-Atlantic Ridge. Appendix II. *The volcanological report of the Royal Society Expedition to Tristan da Cunha, 1962.*, Philosophical Transactions of the Royal Society of London.

Milner, S. C. & Le Roex, A. P. (1996) Isotope characteristics of the Okenyenya igneous complex, northwestern Namibia: constraints on the composition of the early Tristan plume and the origin of the EM1 mantle component. *Earth and Planetary Science Letters,* 141, 277-291.

Münker, C., Weyer, S., Scherer, E. & Mezger, K. (2001) Separation of high field strength elements (Nb, Ta, Zr, Hf) and Lu from rock samples for MC-ICPMS measurements. *Geochemistry Geophysics Geosystems,* 2, 2001.

Münker, C., Worner, G., Yogodzinski, G. & Churikova, T. (2004) Behaviour of high field strength elements in subduction zones: constraints from Kamchatka-Aleutian arc lavas. *Earth And Planetary Science Letters,* 224, 275-293.

Mysen, B. (1978) Experimental determination of nickel partition coefficients between liquid, pargasite and garnet peridotite minerals and concentration limits of behaviour to Henry's Law at high pressure and temperature. *American Journal of Science,* 278, 217-243.

O'hara, M. J. (1965) Primary magmas and the origin of basalts. *Scottish Journal of Geology,* 1, 19-40.

Ohtani, E. & Kumazawa, M. (1981) Melting of forsterite Mg_2SiO_4 up to 15GPa. *Physics of the Earth and Planetary Interiors,* 27, 32-38.

Patchett, P. J. & Tatsumoto, M. (1980) Hafnium isotope variations in oceanic basalts. *Geophysical Research Letters,* 7, 1077-1080.

Patchett, P. J., White, W. M., Feldmann, H., Kielinczuk, S. & Hofmann, A. W. (1984) Hafnium/rare earth element fractionation in the sedimentary system and crustal recycling into the Earth's mantle. *Earth and Planetary Science Letters,* 69, 365-378.

Pilet, S., Hernandez, J., Sylvester, P. & Poujol, M. (2005) The metasomatic alternative for ocean island basalt chemical heterogeneity. *Earth and Planetary Science Letters,* 236, 148-166.

Piper, D. Z. (1974) Rare earth elements in ferromanganese nodules and other marine phases. *Geochimica Et Cosmochimica Acta,* 38, 1007-1022.

Plank, T. & Langmuir, C. H. (1998) The chemical composition of subducting sediment and its consequences for the crust and mantle. *Chemical Geology,* 145, 325-394.

Richardson, S. H., Erlank, A. J., Duncan, A. R. & Reid, D. L. (1982) Correlated Nd, Sr and Pb isotope variation in Walvis Ridge basalts and implications for the the evolution of their mantle source. *Earth and Planetary Science Letters,* 59, 327-342.

Richardson, S. H., Erlank, A. J., Reid, D. L. & Duncan, A. R. (1984) Major and Trace Elements and Nd and Sr Isotope Geochemistry of Basalts from the Deep Sea Drilling Project Leg 74 Walvis Ridge Transect. IN Moore, T. C. & Rabinowitz, P. D. (Eds.) *Initial Reports of the Deep Sea Drilling Project.* Washington D.C., U.S. Government Printing Office.

Ringwood, A. E. (1958) The constitution of the mantle, 3, Consequence of the olivine-spinel transition. *Geochimica Et Cosmochimica Acta,* 15, 195-212.

Ringwood, A. E. (1966) Mineralogy of the mantle. IN Hurley, P. M. (Ed.) *Advances in Earth Science.* Cambridge, Massachusetts, MIT Press.

Ringwood, A. E. (1975) *Composition and Petrology of the Earth's Mantle*, McGraw-Hill, New York.

Roeder, P. L. & Emslie, R. F. (1970) Olivine-liquid equilibrium. *Contributions To Mineralogy And Petrology,* 29, 275-289.

Rubatto, D. & Hermann, J. (2003) Zircon formation during fluid circulation in eclogites (Monviso, Western Alps): Implications for Zr and Hf budget in subduction zones. *Geochimica Et Cosmochimica Acta,* 67, 2173-2187.

Salters, V. J. M. & Hart, S. R. (1989) The hafnium paradox and the role of garnet in the source of mid-ocean-ridge basalts. *Nature,* 342, 420-422.

Salters, V. J. M. & Hart, S. R. (1991) The mantle sources of ocean ridges, islands and arcs: the Hf-isotope connection. *Earth and Planetary Science Letters,* 104, 364-380.

Salters, V. J. M. & Stracke, A. (2004) Composition of the depleted mantle. *Geochemistry Geophysics Geosystems,* 5.

Salters, V. J. M. & White, W. M. (1998) Hf isotope constraints on mantle evolution. *Chemical Geology,* 145, 447-460.

Sguigna, A. P., Larabee, A. J. & Waddington, J. C. (1982) The half-life of ^{176}Lu by a γ–γ coincidence measurement. *Canadian Journal of Physics,* 60, 361-364.

Shaw, D. M. (1970) Trace element fractionation during anatexis. *Geochimica et Cosmochimica Acta,* 34, 237-243.

Shimizu, N., Sawatari, H., Kawata, Y., Dunkley, P. N. & Masuda, A. (1992) Ce and Nd isotope geochemistry on island-arc volcanic rocks with negative Ce anomaly - existence of sourcess with concave REE patterns in the mantle beneath the Solomon and Bonin island arcs. *Contributions To Mineralogy And Petrology,* 110, 242-252.

Skulski, T., Minarik, W. & Watson, E. B. (1994) High-Pressure Experimental Trace-Element Partitioning between Clinopyroxene and Basaltic Melts. *Chemical Geology,* 117, 127-147.

Sobolev, A. V., Hofmann, A. W., Kuzmin, D. V., Yaxley, G. M., Arndt, N. T., Chung, S. L., Danyushevsky, L. V., Kerr, A. C., Krivolutskaya, N. A., Matvienkov, V. V., Nikogosian, I. K., Rocholl, A., Sigurdsson, I. A., Sushchevskaya, N. M. & Teklay, M. (2007) The Amount of Recycled Crust in Sources of Mantle-Derived Melts. *Sciencexpress,* 29 March 2007, 1-6.

Sobolev, A. V., Hofmann, A. W., Sobolev, S. V. & Nikogosian, I. K. (2005) An olivine-free mantle source of Hawaiian shield basalts. *Nature,* 434, 590-597.

Sobolev, A. V., Migdisov, A. A. & Portnyagin, M. V. (1996) Incompatible element partitioning between clinopyroxene and basalt liquid by the study of melt inclusions in minerals from Troodos lavas, Cyprus. *Petrology,* 4, 307-317.

Stolper, E. M. (1980) A phase diagram for mid-ocean ridge basalts: preliminary results and implications for petrogenesis. *Contributions To Mineralogy And Petrology,* 74.

Stracke, A., Bizmis, M. & Salters, V. J. M. (2003) Recycling oceanic crust: Quantitative constrains. *Geochemistry Geophysics Geosystems,* 4, 1-33.

Sun, S.-S. & Mcdonough, W. F. (1989) Chemical and isotopic systematics of oceanic basalts: implications for mantle composition and processes. IN Saunders, A. D. & Norry, M. J. (Eds.) *Magmatism in the Ocean Basins.* London, Geolocial Society Special Publication.

Sun, S.-S. & Mcdonough, W. F. (1995) The composition of the Earth. *Chemical Geology,* 120, 223-253.

Takahashi, E. (1986) Melting of a Dry Peridotite KLB-1 up to 14GPa: Implications on the Origin of Peridotitic Upper Mantle. *Journal of Geophysical Research,* 91, 9367-9382.

Takahashi, E. & Kushiro, I. (1983) Melting of a dry peridotite at high pressures and basalt magma genesis. *American Mineralogist,* 68, 859-879.

Thomas, J. B., Bodnar, R. J., Shimizu, N. & Sinha, A. K. (2002) Determination of zircon/melt trace element partition coefficients from SIMS analysis of melt inclusions in zircon. *Geochimica et Cosmochimica Acta,* 66, 2887-2901.

Toyoda, K., Nakamura, Y. & Masuda, A. (1990) Rare earth elements of Pacific pelagic sediments. *Geochimica Et Cosmochimica Acta,* 54, 1093-1103.

Vervoort, J. D., Patchett, P. J., Blichert-Toft, J. & Albarede, F. (1999) Relationships between Lu-Hf and Sm-Nd isotopic systems in the global sedimentary system. *Earth and Planetary Science Letters,* 168, 79-99.

Villemant, B., Jaffrezic, H., Joron, J. L. & Treuil, M. (1981) Distribution Coefficients of Major and Trace-Elements - Fractional Crystallization in the Alkali Basalt Series of Chaine-Des-Puys (Massif Central, France). *Geochimica Et Cosmochimica Acta,* 45, 1997-2016.

Walter, J. M. & Presnall, D. C. (1994) Melting Behavior of Simplified Lherzolite in the System CaO-MgO-Al_2O_3-SiO_2-Na_2O from 7 to 35 kbar. *Journal Of Petrology,* 35, 329-359.

Weaver, B. L. (1991) The origin of ocean island basalt end-member compositions: trace element and isotopic constraints. *Earth and Planetary Science Letters,* 104, 381-397.

Weaver, B. L., Wood, D. A., Tarney, J. & Joron, J. L. (1987) Geochemistry of ocean island basalts from South Atlantic: Ascension, Bouvet, St. Helena, Gough and Tristan da Cunha. *Geologistal Society, London, Special Publications,* 30, 253-267.

White, W. M., Dupre, B. & Vidal, P. (1985) Isotope and trace element geochemistry of sediments from the Barbados Ridge-Demerara Plain region, Atlantic ocean. *Geochimica Et Cosmochimica Acta,* 49, 1875-1886.

White, W. M. & Hofmann, A. W. (1982) Sr and Nd isotope geochemistry of oceanic basalts and mantle evolution. *Nature,* 296, 821-825.

Whittaker, E. J. W. & Muntus, R. (1970) Ionic radii for use in geochemistry. *Geochimica Et Cosmochimica Acta,* 34, 945-956.

Willbold, M. & Stracke, A. (2006) Trace element composition of mantle end-members: Implications for recycling of oceanic and upper and lower continental crust. *Geochemistry Geophysics Geosystems,* 7, 1-30.

Yoder, H. S. (1952) Change of melting point of diopside with pressure. *Journal of Geology,* 60, 364-374.

Yoder, H. S. J. (1976) *Generation of Basaltic Magma*, National Academy of Science, Washington D.C.

Zack, T. & Brumm, R. (1998) Ilmenite/liquid partition coefficients of 26 trace elements determined through ilmenite/clinopyroxene partitioning in garnet pyroxene. IN Gurney, J. J., Gurney, J. L., Pascoe, M. D. & Richardson, S. H. (Eds.) *7th International Kimberlite Conference.* Cape Town, Red Roof Design.

Zielinski, R. A. & Frey, F. A. (1970) Gough Island: Evaluation of a Fractional Crystallization Model. *Contributions to Mineralogy and Petrology,* 29, 242-254.

Zindler, A. & Hart, R. S. (1986) Chemical Geodynamics. *Annual Review of Earth and Planetary Sciences,* 14, 493-571.

Appendix A Sample Petrography

A.1 Gough Island

Sample Number	Rock Type	Stratigraphic Unit	Sample Location
AL15C	Ol-Cpx-Phyric Basalt	Lower Basalt	Pummel Crag Ridge
Phenocrysts	**Modal Abundances**	**Texture & Alteration**	**Groundmass**
Cpx Ol Plag (Phenocryst) Groundmass Minerals	40% 25% 20% 30%	Coarsely porphyritic, vesicular with an intergranular texture. Alteration indicates iddingsite ± bowlingite grain-boundary alteration.	This rock contains phenocrysts of anhedral cpx (>8mm), plag (1mm) and hypohyaline vesicles with glomerocrysts of anhedral to subhedral ol (0.5-5mm).

Sample Number	Rock Type	Stratigraphic Unit	Sample Location
ALR6G	Ol-Aphyric Basalt	Lower Basalt	Pummel Crag Ridge
Phenocrysts	**Modal Abundances**	**Texture & Alteration**	**Groundmass**
Ol Cpx Groundmass Minerals	30% 5% 30%	Aphyric to finely porphyritic, vesicular with an intergranular texture. Alteration is minimum.	This rock contains phenocrysts of anhedral cpx (1mm) and hypohyaline vesicles (<1mm) with glomerocrysts of anhedral ol (0.5-4mm).

Sample Number	Rock Type	Stratigraphic Unit	Sample Location
ALR7G	Ol-Phyric Basalt	Lower Basalt	Pummel Crag Ridge
Phenocrysts	**Modal Abundances**	**Texture & Alteration**	**Groundmass**
Ol Cpx Groundmass Minerals	60% 5% 35%	Coarsely porphyritic, vesicular with an intergranular texture. Alteration is minimum, bastitisation is present on ol grain boundaries.	This rock contains phenocrysts of subhedral cpx (0.5-2mm), anhedral to subhedral ol (0.5-10mm) and hypohyaline vesicles (0.5-2mm).

Sample Number	Rock Type	Stratigraphic Unit	Sample Location
AL28G	Ol-Aphyric Trachybasalt	Middle Basalt	Pummel Crag Ridge
Phenocrysts	**Modal Abundances**	**Texture & Alteration**	**Groundmass**
Ol Groundmass Minerals	5% 95%	Aphyric to finely porphyritic, vesicular with an intergranular texture. No alteration.	This rock contains phenocrysts of subhedral ol (0.5mm) and hypohyaline vesicles (0.5-2mm).

Sample Number	Rock Type	Stratigraphic Unit	Sample Location
ALR9G	Ol-Aphyric Trachybasalt	Middle Basalt	Pummel Crag Ridge
Phenocrysts	**Modal Abundances**	**Texture & Alteration**	**Groundmass**
Ol Cpx Plag (Phenocryst) Groundmass Minerals	20% 20% 10% 50%	Coarsely porphyritic, vesicular with an intergranular texture. Alteration is minimum, but idn is present along ol grain boundaries.	This rock contains phenocrysts of plag (1mm) and hypohyaline vesicles (0.5-6mm) with cumulocrysts of subhedral ol (0.5-2mm) and subhedral cpx (0.5mm).

Sample Number	Rock Type	Stratigraphic Unit	Sample Location
ALR10G	Ol-Phyric Trachybasalt	Middle Basalt	Pummel Crag Ridge
Phenocrysts	**Modal Abundances**	**Texture & Alteration**	**Groundmass**
Ol Cpx Plag (Phenocryst) Groundmass Minerals	10% 10% 10% 70%	Moderately porphyritic, vesicular with an intergranular texture. Alteration is minimum.	This rock contains phenocrysts of anhedral to subhedral ol (0.5-4mm), subhedral cpx (2mm), plag (1mm) as well as hypohyaline vesicles (0.5-2mm).

Sample Number	Rock Type	Stratigraphic Unit	Sample Location
ALR12G	Ol-Px-Aphyric Basalt	Middle Basalt	South Peak
Phenocrysts	**Modal Abundances**	**Texture & Alteration**	**Groundmass**
Ol Cpx Plag (Phenocryst) Groundmass Minerals	15% 10% 5% 70%	Finely porphyritic, vesicular with an intergranular texture. No alteration present.	This rock contains glomerocrysts of subhedral ol (0.5-2mm) and cpx (0.5mm) and plag (1mm) as well as hypohyaline vesicles.

Sample Number	Rock Type	Stratigraphic Unit	Sample Location
ALR13G	Ol Aphyric Trachybasalt	Middle Basalt	South Peak
Phenocrysts	**Modal Abundances**	**Texture & Alteration**	**Groundmass**
Ol Cpx Plag (Phenocryst) Groundmass Minerals	10% 5% 5% 80%	Aphyric to finely porphyritic, vesicular with an intergranular texture. Lots of alteration including idn on ol grain boundaries.	This rock contains phenocrysts of subhedral ol (0.5-2mm), subhedral cpx (0.5-2mm) and hypohyaline vesicles with glomerocrysts of plag (0.5-1mm).

Sample Number	Rock Type	Stratigraphic Unit	Sample Location
ALR14G	Ol Px Aphyric Trachybasalt	Middle Basalt	South Peak
Phenocrysts	**Modal Abundances**	**Texture & Alteration**	**Groundmass**
Ol Cpx Groundmass Minerals	20% 10% 70%	Finely cumuloporphyritic, vesicular with an intergranular texture. No alteration present.	This rock contains glomerocrysts and cumulocrysts of euhedral to anhedral ol (0.1-2mm), subhedral cpx (<2mm), plag (1mm) as well as hypohyaline vesicles.

Sample Number	Rock Type	Stratigraphic Unit	Sample Location
ALR23G	Ol-Aphyric Trachybasalt	Middle Basalt	South Peak
Phenocrysts	**Modal Abundances**	**Texture & Alteration**	**Groundmass**
Ol Cpx Groundmass Minerals	5% 5% 90%	Aphyric to finely porphyritic, vesicular with an intergranular texture. Alteration is minimum.	This rock contains phenocrysts of anhedral to subhedral ol (<0.5mm), anhedral to subhedral cpx (<0.5mm) and hypohyaline vesicles (0.5mm).

Sample Number	Rock Type	Stratigraphic Unit	Sample Location
ALR24G	Ol-Phyric Basalt	Middle Basalt	Mount Rowett
Phenocrysts	**Modal Abundances**	**Texture & Alteration**	**Groundmass**
Ol Cpx Groundmass Minerals	60% 5% 35%	Coarsely porphyritic, vesicular with an intergranular texture and complex zoning is seen in phenocrysts. No alteration present.	This rock contains phenocrysts and glomerocrysts of euhedral to anhedral ol (<0.5mm) as well as hypohyaline vesicles (1-6mm) with chill margins.

Sample Number	Rock Type	Stratigraphic Unit	Sample Location
ALR25G	Ol-Cpx-Aphyric Trachybasalt	Middle Basalt	Mount Rowett
Phenocrysts	**Modal Abundances**	**Texture & Alteration**	**Groundmass**
Ol Cpx Plag (Phenocryst) Groundmass Minerals	20% 15% 5% 60%	Aphyric to finely porphyritic, vesicular with an intergranular texture. Lots of alteration present, especially idin ol grain boundaries.	This rock contains phenocrysts of subhedral ol (0.5-4mm), subhedral cpx (0.5-1mm), plag (1mm) as well as hypohyaline vesicles (0.5mm).

Sample Number	Rock Type	Stratigraphic Unit	Sample Location
ALR27G	Ol-Phyric Basalt	Lower Basalt	South Peak
Phenocrysts	**Modal Abundances**	**Texture & Alteration**	**Groundmass**
Ol Plag (Phenocryst) Cpx Groundmass Minerals	50% 10% 5% 35%	Coarsely porphyritic, vesicular with an intergranular texture. Alteration is minimum but idin ol grain boundary alteration present.	This rock contains phenocrysts of euhedral to anhedral ol (0.5-4mm) and hypohyaline vesicles (0.5-4mm) with glomerocrysts of plag (2mm) and subhedral cpx (2mm).

Sample Number	Rock Type	Stratigraphic Unit	Sample Location
ALR30G	Cpx-Aphyric Basalt to Trachyandesite	Lower Basalt	Disney Ridge
Phenocrysts	**Modal Abundances**	**Texture & Alteration**	**Groundmass**
Cpx Ol Plag (Phenocryst) Groundmass Minerals	10% 5% 5% 80%	Aphyric to finely porphyritic, vesicular with an intergranular texture. Lots of alteration especially idin ol grain boundaries.	This rock contains phenocrysts of subhedral ol (0.5mm), subhedral cpx (4mm) and hypohyaline vesicles (<2mm) with glomerocrysts of plag (2-4mm).

Sample Number	Rock Type	Stratigraphic Unit	Sample Location
ALR42G	O-Plag Phyric Basaltic-Trachyandesite	Lower Basalt	Dell Rocks
Phenocrysts	**Modal Abundances**	**Texture & Alteration**	**Groundmass**
Cpx O Plag (Phenocryst) Groundmass Minerals	20% 5% 10% 65%	Finely to moderately porphyritic with an intergranular texture. Alteration is minimum.	This rock contains phenocrysts of anhedral to subhedral ol (0.5-2mm), anhedral cpx (2mm), Ti-mt (1mm) with glomerocrysts of plag (2mm).

Sample Number	Rock Type	Stratigraphic Unit	Sample Location
ALR33G	O-Phyric Basaltic Trachyandesite	Lower Basalt	Dell Rocks
Phenocrysts	**Modal Abundances**	**Texture & Alteration**	**Groundmass**
Ol Plag (Phenocryst) Opaque (Mt) Groundmass Minerals	40% 10% 5% 45%	Moderately porphyritic with an intergranular texture. Alteration is minimum but due to grain-boundary alteration present.	This rock contains phenocrysts of euhedral to anhedral ol (0.5-4mm), Ti-mt (0.5-2mm) and hypohya ine ves cles (0.5-4mm) with glomerocrysts of plag (4mm).

Sample Number	Rock Type	Stratigraphic Unit	Sample Location
ALR34G	Ol Aphyric Basaltic Trachyandesite	Middle Basalt	The Glen
Phenocrysts	**Modal Abundances**	**Texture & Alteration**	**Groundmass**
Plag (Phenocryst) Cpx O Groundmass Minerals	10% 5% 1% 84%	Aphyric to finely porphyritic, vesicular with an intergranular texture. No alteration.	This rock contains phenocrysts of euhedral cpx (6mm), plag (5mm) and hypohyaline vesicles (0.5-1mm) with glomerocrysts of ol (0.3-1mm).

Sample Number	Rock Type	Stratigraphic Unit	Sample Location
ALR45G	Ol-Cpx Aphyric Trachybasalt	Lower Basalt	The Glen
Phenocrysts	**Modal Abundances**	**Texture & Alteration**	**Groundmass**
Ol Cpx Groundmass Minerals	10% 3% 85%	Aphyric to finely porphyritic, vesicular with an intergranular texture. Lots of alteration present especially idin ol grain-boundary alteration.	This rock contains phenocrysts of anhedral cpx (1-4mm) and hypohya ine vesicles (0.3-4mm) with g omerocrysts of euhedral to anhedral ol (0.2-0.8mm).

Sample Number	Rock Type	Stratigraphic Unit	Sample Location
ALR36G	O-Phyric Basalt	Lower Basalt	Michard's Ridge
Phenocrysts	**Modal Abundances**	**Texture & Alteration**	**Groundmass**
Ol Cpx Plag (Phenocryst) Groundmass Minerals	50% 10% 5% 35%	Coarsely porphyritic, vesicular with an intergranular texture. Alteration is minimum.	This rock contains phenocrysts of euhedral to anhedral ol (0.5-8mm), cpx (4mm) and hypohya ine vesicles (0.5mm) with glomerocrysts of plag (6mm).

Sample Number	Rock Type	Stratigraphic Unit	Sample Location
ALR41G	Ol-Px-Plag-Phyric Basalt	Middle Basalt	Mount Rowett
Phenocrysts	**Modal Abundances**	**Texture & Alteration**	**Groundmass**
Ol Cpx Plag (Phenocryst) Groundmass Minerals	40% 20% 10% 30%	Coarsely porphyritic, vesicular with an intergranular texture. No Alteration.	This rock contains phenocrysts of cpx (6mm) and hypohyaline vesicles (2mm) with glomerocrysts of plag (2-4mm) and euhedral to subhedral olivine (0.5-5mm)

Sample Number	Rock Type	Stratigraphic Unit	Sample Location
ALR42E	Ol-Px-Plag-Phyric Basalt	Middle Basalt	Mount Rowett
Phenocrysts	**Modal Abundances**	**Texture & Alteration**	**Groundmass**
Ol Plag (Phenocryst) Cpx Groundmass Minerals	50% 20% 10% 20%	Coarsely porphyritic, vesicular with an intergranular texture. Minimum alteration	This rock contains phenocrysts of cpx (0.5-8mm), euhedral to anhedral ol (0.5-10mm), plag (4mm) and hypohyaline vesicles (2mm).

Sample Number	Rock Type	Stratigraphic Unit	Sample Location
ALR43C	Ol-Plag-Phyric Basalt	Middle Basalt	Mount Rowett
Phenocrysts	**Modal Abundances**	**Texture & Alteration**	**Groundmass**
Ol Plag Groundmass Minerals	40% 30% 30%	Moderately porphyritic, vesicular with an intergranular texture. Lots of alteration present, especially ol grain boundary alteration to idin.	This rock contains phenocrysts of ol (0.5-4mm) and hypohyaline vesicles (2mm) with glomerocrysts of plag (1-4mm).

Sample Number	Rock Type	Stratigraphic Unit	Sample Location
ALR44G	Px-Ol-Plag-Phyric Basalt	Middle Basalt	Mount Rowett
Phenocrysts	**Modal Abundances**	**Texture & Alteration**	**Groundmass**
Cpx Ol Plag (Phenocryst) Groundmass Minerals	15% 30% 5% 30%	Coarsely porphyritic, vesicular with an intergranular texture. Alteration is minimum, but idin ol grain boundary alteration present.	This rock contains phenocrysts of anhedral cpx (7-9mm), anhedral to subhedral ol (0.5-2mm) and hypohyaline vesicles with glomerocrysts of plag (3-5mm).

Sample Number	Rock Type	Stratigraphic Unit	Sample Location
ALR45G	Ol-Cpx-Plag-Phyric Basalt	Middle Basalt	Mount Rowett
Phenocrysts	**Modal Abundances**	**Texture & Alteration**	**Groundmass**
Ol Cpx Plag (Phenocryst) Groundmass Minerals	30% 30% 10% 30%	Coarsely porphyritic, vesicular with an intergranular texture. Lots of alteration present especially alteration of ol grain boundaries to idin.	This rock contains phenocrysts of subhedral to anhedral ol (0.5-5mm), and hypohyaline vesicles (1mm) with glomerocrysts of plag (2-8mm) and anhedral cpx (7mm).

Sample Number	Rock Type	Stratigraphic Unit	Sample Location
ALR47G	Ol-Pryric Trachybasalt	Middle Basalt	Mount Rowett
Phenocrysts	**Modal Abundances**	**Texture & Alteration**	**Groundmass**
Ol Cpx Plag (Phenocryst) Groundmass Minerals	30% 10% 10% 50%	Moderately porphyritic, vesicular with an intergranular texture. Lots of alteration present, especially alteration of ol grain boundaries to idin.	This rock contains phenocrysts of anhedral cpx (0.5-4mm), anhedral ol (0.5-4mm), and hypohyaline vesicles with glomerocrysts of plag (6mm).

Sample Number	Rock Type	Stratigraphic Unit	Sample Location
ALR49G	Ol-Plag-Aphyric Basaltic-Trachyandesite	Middle Basalt	Mount Rowett
Phenocrysts	**Modal Abundances**	**Texture & Alteration**	**Groundmass**
Ol Plag (Phenocryst) Groundmass Minerals	5% 5% 90%	Aphyric to finely porphyritic with an intergranular texture. Lots of alteration present, especially alteration of ol grain boundaries to idin ± bow.	This rock contains phenocrysts of anhedral to subhedral ol (6mm) and plag (4mm).

Sample Number	Rock Type	Stratigraphic Unit	Sample Location
ALR50G	Ol-Pryric Basalt	Middle Basalt	Mount Rowett
Phenocrysts	**Modal Abundances**	**Texture & Alteration**	**Groundmass**
Ol Cpx Plag (Phenocryst) Groundmass Minerals	20% 5% 10% 65%	Moderately porphyritic with an intergranular texture. Alteration is a minimum but there is ol grain boundaries alteration to idin present.	This rock contains phenocrysts of euhedral to anhedral ol (0.5-2mm), subhedral cpx (2mm) and hypohyaline vesicles (1mm) with glomerocrysts of plag (<2mm).

Sample Number	Rock Type	Stratigraphic Unit	Sample Location
ALR51G	Ol-Phyric Basalt	Middle Basalt	Mount Rowett
Phenocrysts	**Modal Abundances**	**Texture & Alteration**	**Groundmass**
Ol Cpx Groundmass Minerals	20% 10% 65%	Moderately to coarsely porphyritic with an intergranular texture. Alteration is minimum.	This rock contains phenocrysts of euhedral to subhedral ol (0.5-4mm), subhedral cpx (4mm) and hypohyaline vesicles (4mm).

Sample Number	Rock Type	Stratigraphic Unit	Sample Location
ALR52G	Ol-Plag-Phyric Basaltic-Trachyandesite	Middle Basalt	Mount Rowett
Phenocrysts	**Modal Abundances**	**Texture & Alteration**	**Groundmass**
Ol Plag (Phenocryst) Cpx Groundmass Minerals	30% 20% 10% 50%	Moderately porphyritic with an intergranular texture. Alteration is minimum.	This rock contains phenocrysts of anhedral cpx (4mm) and glomerocrysts of plag (6mm) and anhedral to subhedral ol (0.5-6mm).

Sample Number	Rock Type	Stratigraphic Unit	Sample Location
ALR55C	Cpx-Ol-Phyric Basalt	Middle Basalt	Mount Jewett
Phenocrysts	**Modal Abundances**	**Texture & Alteration**	**Groundmass**
Cpx Ol Groundmass Minerals	20% 10% 70%	Coarsely porphyritic, vesicular with an intergranular texture. Alteration is minimum.	This rock contains phenocrysts of anhedral ol (0.5-4mm), subedral cpx (0.5-8mm) and hypohyaline vesicles (4mm).

Sample Number	Rock Type	Stratigraphic Unit	Sample Location
ALR56G	Ol Aphyric Basalt	Upper Basalt	Mount Jewett
Phenocrysts	**Modal Abundances**	**Texture & Alteration**	**Groundmass**
Ol Plag (Phenocryst) Groundmass Minerals	25% 5% 70%	Aphyric to finely porphyritic, vesicular with an intergranular texture. Alteration is minimum.	This rock contains phenocrysts of anhedral ol (0.5-1mm), rare plag (1mm) and hypohyaline vesicles (0.5mm).

Sample Number	Rock Type	Stratigraphic Unit	Sample Location
ALR64A	Ol-Plag-Phyric Trachybasalt	Middle Basalt	Mount Jewett
Phenocrysts	**Modal Abundances**	**Texture & Alteration**	**Groundmass**
Ol Plag (Phenocryst) Groundmass Minerals	20% 20% 60%	Fine to moderately porphyritic with an intergranular texture. Lots of alteration, especially idin on ol grain boundaries.	This rock contains phenocrysts of subhedral to anhedral ol (0.5-1mm), plag (1-6mm) and subhedral cpx (2mm).

A.2 McNish Seamount

Sample Number	Rock Type	Stratigraphic Unit	Sample Location
AG32-7-1	Ol-Phyric Basalt	-	McNish Seamount
Phenocrysts	**Modal Abundances**	**Texture & Alteration**	**Groundmass**
Ol Cpx Glassy Matrix	20% 10% 70%	Fine to moderately porphyritic, vesicular with a glass matrix. Alteration is minimum	This rock contains phenocrysts of subhedral to euhedral ol (0.1-0.6mm), subhedral cpx (0.6mm) and hypohyaline vesicles.

Appendix B Sample Preparation

Samples were prepared in two stages; an initial sample digestion stage followed by a hafnium purification stage. A flowchart of the full procedure is shown in Fig B-1.

The first stage involves weighing 200mg of sample and the in-house standard K1919. Powdered samples are leached in a weak acid (1ml 3N HCl) in order to remove any surface contamination. Sample digestion involves adding a ~3:1 2.65ml $HF_{conc.}$:$HNO_{3\ conc.}$ solution to the dry, leached samples and allowing samples to sit at 130°C for 48 hours, in order to break-down the silicate minerals into fluorides. Addition of 350µl conc. HNO_3 is the next step, followed by a dry-down period at low heat, addition of 1ml 6N HCl and another dry-down step, the addition of 5ml 6N HCl:0.06N HF and heating the samples for 12 hours at 100°C in order to convert fluorides into chlorides.

The second stage of sample preparation involves the purification of Lu and Hf in the samples using reversed phase cation exchange one-column chromatography, adapted from Münker *et al.*, (2001) at L-DEO (Cai, *in prep*). This first step involves preparing columns (40xØ10mm spout and 50xØ5mm, volume of ~15ml) for each sample using EICHROM Ln-Spec® resin. To ensure no cross-contamination of samples, the resin is cleaned first by eluting 15ml QD[5], 15ml 6N HCl, 15ml of 2N HF, 15ml QD and 10ml 3N HCl. Prior to loading the sample, the sample has to be re-dissolved in 10ml 3N HCl, heated to 120°C for 24 hours, allowed to cool and added to 0.5ml 1M ascorbic acid in order for the ascorbic acid to complex to any iron in the sample. After loading the sample, the matrix elements are eluted with 10ml 3N HCl, followed by 40ml 6N HCl to remove HREE. The resin is subsequently rinsed with 6ml QD in order to rinse any remaining HCl from the resin followed by the addition of 40ml 0.09N Hcit:1wt%H_2O_2:0.45N HNO_3 in order to remove any Ti [6](and Cr) in the sample. This step is followed by rinsing the H_2O_2-Hcit-HNO_3 solution with 12ml QD[7] and Hf elution using 12ml 6N HCl:0.2N HF. The Hf-elution is collected and dried down at 80°C overnight whilst the remainder of sample is rinsed from the resin using 10ml 2N HF and 10ml QD. The dried down sample is subsequently picked up in 30µl conc. HNO_3 and 30µl conc. HF and dried down until only a very small drop remains. This is repeated three times until finally the sample is diluted with 500µl QD and ready to be analysed by the MC-ICP-MS.

[5] QD refers to milliq water

[6] Abundant Ti (and Cr) could lead to transmission errors and instrument drift in the MC-ICP-MS (Blichert-Toft & Albarède, 1997).

[7] It is important to ensure that all citric acid and H_2O_2 have been removed from the sample as the presence of organic molecules in the sample can be detrimental to the MC-ICP-MS and may result in anomalous results.

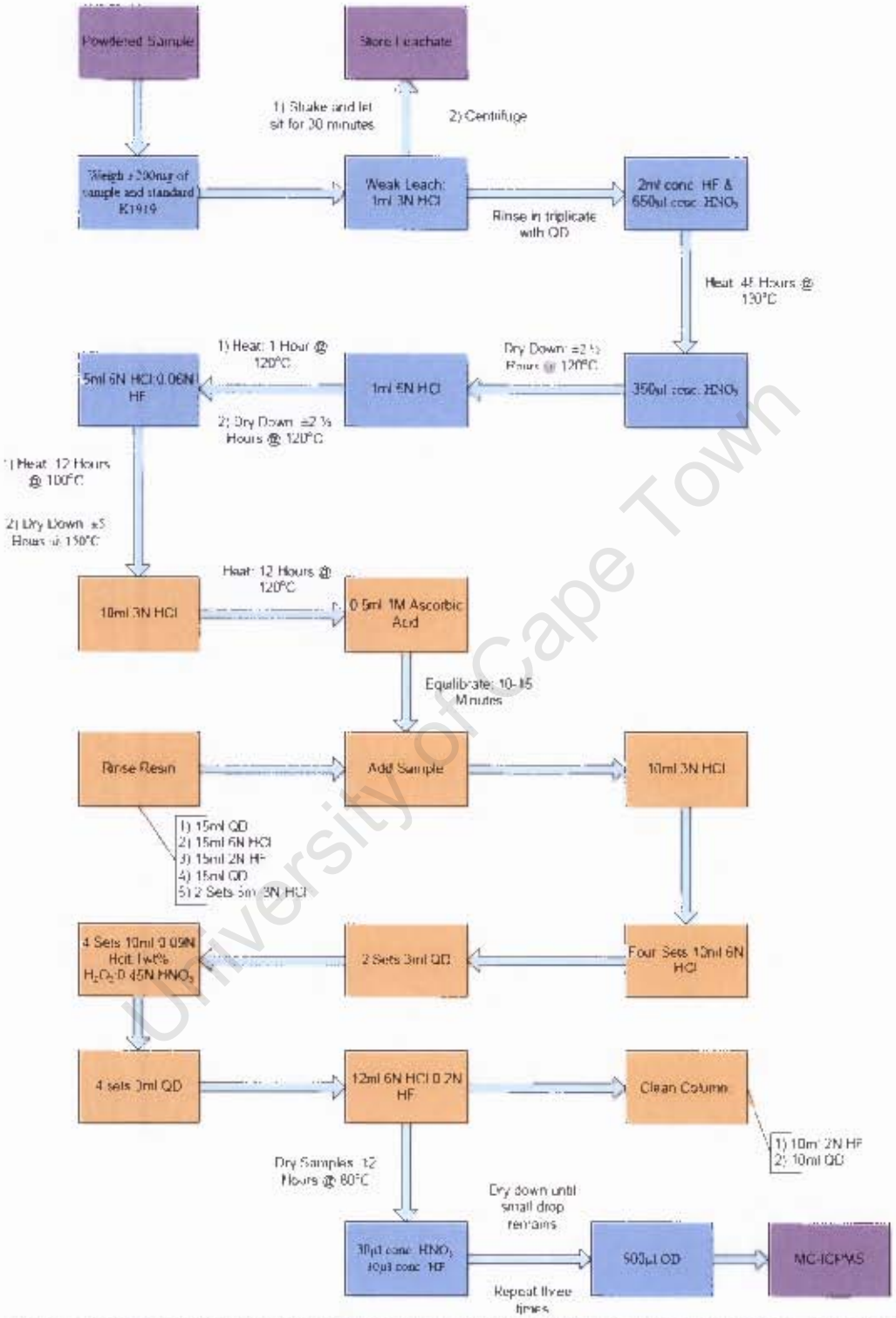

Fig B-1: Flowchart of the chemical procedure used to prepare samples for Hf-isotope analysis. Adapted by Cai (in prep.) from (Münker *et al.*, 2001).